國 立 交 通 大 學

應用化學系碩士班

碩 士 論 文

利用低振動頻率顯微拉曼光譜儀即時監控結晶態

1,1′-binaphthyl 在同質異像體間變化動力學與拉曼成像分析

In-situ Tracing of Transformation Dynamics and

Molecular Imaging of Crystalline 1,1′-Binaphthyl

by Low-Frequency Raman Microspectroscopy

研 究 生：張君輔

指導教授：重藤真介　博士

中 華 民 國 一〇二 年 七 月

利用低振動頻率顯微拉曼光譜儀即時監控結晶態 1,1′-binaphthyl 在同質異像體間變化動力學與拉曼成像分析

研 究 生：張君輔　　Student：Chun-Fu Chang

指導教授：重藤真介 博士　　Advisor：Dr. Shinsuke Shigeto

國 立 交 通 大 學

應用化學系碩士班

碩 士 論 文

A Thesis
Submitted to M. S. Program, Department of Applied Chemistry
College of Science
National Chiao Tung University
in Partial Fulfillment of the Requirements
for the Degree of
Master
in
M. S. Program, Department of Applied Chemistry

July 2013

Hsinchu, Taiwan, Republic of China

中華民國一〇二年七月

利用低振動頻率顯微拉曼光譜儀即時監控結晶態 1,1′-binaphthyl 在同質異像體間變化動力學與拉曼成像分析

學生: 張君輔　　指導教授: 重藤真介 博士

國立交通大學應用化學系碩士班

摘要

除了 X-光繞射分析以外，是否有其他研究晶體結構的方法？低頻率拉曼光譜提供豐富的晶體結構資訊以及分子位向。實驗室自行架設的低振動頻率拉曼光譜儀能觀測低至 9.8 cm^{-1} 的拉曼訊號。此外，本系統亦能在顯微鏡下進行空間解析量測並即時分析晶體結構。在此，作者研究不同晶形的 1,1′-binaphthyl 以展示這套新穎的分析方法。此聯芳化合物在結晶態時因為兩個萘環間有不同的二面角而呈現兩種不同的晶形：類順式和類反式（同質異像體）。當類順式被緩慢加熱時，會透過昇華和再結晶的機制逐漸轉變成類反式。本文中，將即時監控此轉變過程並使用顯微拉曼成像法分析晶形轉變後類順式、類反式晶體的分佈情形。

類順式和類反式在指紋區的拉曼光譜非常類似，唯一的區別指標是 510/532 cm^{-1} 波峰的強度比。然而，它們的光譜在低頻區截然不同。例如類順式最強的訊號在 100cm^{-1}；類反式最強的訊號在 26 cm^{-1}。是以此二低頻率特徵峰被用來區別類順式和類反式混合晶體。利用此二低頻率特徵峰建立的拉曼影像呈現了高度的選擇性與影像對比度。此外，低頻率拉曼影像更在外表看似完美的單晶中發現了分子的不規則排列。諸此結果讓我們意識到低頻率拉曼成像法，將會成為十分有用的晶體結構分析工具。

In-situ Tracing of Transformation Dynamics and Molecular Imaging of Crystalline 1,1′-Binaphthyl by Low-Frequency Raman Microspectroscopy

Student: Chun-Fu Chang Advisor: Dr. Shinsuke Shigeto

M. S. Program, Department of Applied Chemistry

National Chiao Tung University

Abstract (in English)

How can we understand crystal structure besides employing X-ray diffraction analysis? Low-frequency (LF) Raman spectra provide a wealth of precious information on crystal structure and orientation and can potentially be a complementary approach to the conventional X-ray diffraction method. However, observation of LF Raman spectra is very challenging due to severe interference of gigantic Rayleigh scattering. In this study, the author uses a laboratory-built LF Raman spectrometer that has the ability to observe Raman signals down to 9.8 cm^{-1}. Because this apparatus is combined with a confocal microscope, it has become feasible to perform space-resolved measurements of crystals under the microscope for *in-situ* crystal structure analysis. Here, the author demonstrates this novel approach by studying crystal polymorphs of 1,1′-binaphthyl. This biaryl compound occurs as two crystal polymorphs with different dihedral angles between the two naphthyl groups: namely, the cisoid (C) and transoid (T) forms. As the C form is heated up, it gradually transforms to the T form via sublimation and subsequent recrystallization. In this thesis, the author presents tracing of this transformation dynamics and LF Raman imaging that visualizes the spatial distribution of the C and T forms after the transformation takes place.

The only effective way to distinguish between the C and T forms by high-frequency Raman bands would be to calculate the intensity ratio for a pair of marker bands (510/532 cm^{-1}). However, the two forms show much more distinct spectral patterns in the LF region. For example, the C form shows the strongest band at 100 cm^{-1}, whereas the T form shows the most intense band at 26 cm^{-1}. Thus, these two LF bands were chosen as markers to selectively probe different crystal polymorphs that coexist in proximity. In sharp contrast with the intensity-ratio image, the LF Raman images at 100 and 26 cm^{-1} show markedly high contrast and clearly discriminate one crystal form from the other. Moreover, we observed inhomogeneous distribution patterns in the LF Raman images, suggesting different crystal

orientations within an apparent single crystal. Our results show that LF Raman spectroscopy and imaging should be a facile yet powerful addition to the toolbox for crystal structure analysis.

Acknowledgements

First, I want to thank Professor Shigeto for providing me a great environment and equipment to study this interesting topic. I also feel grateful for Professor Hamaguchi, who inspired me that “spectrum is a letter from molecule” and directed me how to read the letter. From Shimada san and Okajima san, I learned many knowledge on fundamental of spectroscopy, alignment of optics, data processing as well as programming. Without you, it is impossible to finish this project, I appreciate what you have taught me. Also, I feel thankful all Shigeto lab members, helping me work out the problems. Finally, I would like to give my sincerely appreciation to my parents who support me both economically and mentally.

Tables of Contents

List of Figures and Tables

Page

Chapter I.

General Introduction

I-1. Motivation of This Study

There are many beautiful crystals exist in Mother Nature. Some are perfect single crystals, and some are polycrystals. How do molecules align in those crystals? How do the molecular interactions change during phase transitions such as melting? Investigating these interesting fundamental physical properties is enormously helpful for both materials and biological sciences. Although X-ray diffraction analysis can precisely determine the crystal structure, long data acquisition time makes real-time monitoring of phase transitions impossible. In this study, the author aims at tracing dynamic changes in intermolecular interactions with a short acquisition time (<1 s) as well as visualizing molecular orientations within organic crystals at the molecular level.

I-2. Raman Measurements of Low-Frequency Motions

Intermolecular forces of molecules in the condensed phase are reflected in intermolecular or collective motions. The collective motions of molecular ensembles move very slowly and are therefore usually observed in the low-frequency region (< 200 cm^{-1}) of an optical spectrum. Measurements of Raman scattering in the low-frequency region have been utilized to discuss the optically active lattice vibration of crystals based on the important theory of the first-order lattice vibration Raman effect [1-3]. Likewise, the phonon modes of organic crystals, which are related to librational lattice vibrations, are observed below 150 cm^{-1} [4-6]. Recently, low-frequency Raman spectroscopy has been applied to estimate the diameter of single-wall carbon nanotube

(SWNT) from the size-dependent ring breathing modes (RBM) in the range of 100–500 cm^{-1} [7-9].

In the past decades, low-frequency Raman spectra were measured with a scanning Raman spectrometer, which is composed of two or three monochromators and a single-channel detector such as photomultiplier tube (PMT) [10]. This kind of setup takes a long time to slowly rotate the grating in order to acquire a Raman spectrum and it can record only one side of anti-Stokes or Stokes Raman signals. Nowadays, thanks to the improvement of laser technology and development of ultra-narrow band rejection filters as well as multi-channel detector, low-frequency Raman measurements can be realized with a short exposure time (< 0.1 s) and a wide spectral coverage [11]. Thus, it is now possible to monitor dynamic behaviors of vibrational motions associated with phase transitions in the condensed phase by low-frequency Raman spectroscopy [12].

The great advantage of the ability to measure both Stokes and anti-Stokes Raman spectra simultaneously is that the intensity ratio of the Stokes and anti-Stokes Raman bands of a given mode, I_{AS}/I_S, can be used to determine "molecular temperature" as follows [13]:

$$\frac{I(\text{anti-Stokes})}{I(\text{Stokes})} = \frac{(\tilde{\nu}_0 - \tilde{\nu}_m)^3}{(\tilde{\nu}_0 + \tilde{\nu}_m)^3} e^{-hc\tilde{\nu}_m/k_BT} \qquad \textbf{(I-1)}$$

where $\tilde{\nu}_0$ is the wavenumber of the laser line, $\tilde{\nu}_m$ is the vibrational frequency of a band of the sample, h is Planck's constant, c is the speed of light, k_B is the Boltzmann constant, and T is absolute temperature of the sample (or more specifically molecules). This equation stems from the fact that Stokes Raman scattering comes from the excitation of molecules in the vibrational ground state ($v = 0 \rightarrow 1$), while anti-Stokes Raman scattering comes from the vibrational excited

state (v = 1 → 0), as shown in Figure I-1. Therefore, I_{AS}/I_S is proportional to the population difference between vibrational excited and ground states by assuming Boltzmann distribution. It is worth noting that around room temperature (~300 K), the I_{AS}/I_S can be barely detected for Raman bands above 800 cm^{-1} due to the weak anti-Stokes Raman signals (Table I-1). However, the I_{AS}/I_S has a large enough value in the low-frequency region (< 200 cm^{-1}) for temperature estimation using Equation I-1, which makes Stokes/anti-Stokes ratio work as a "molecular thermometer".

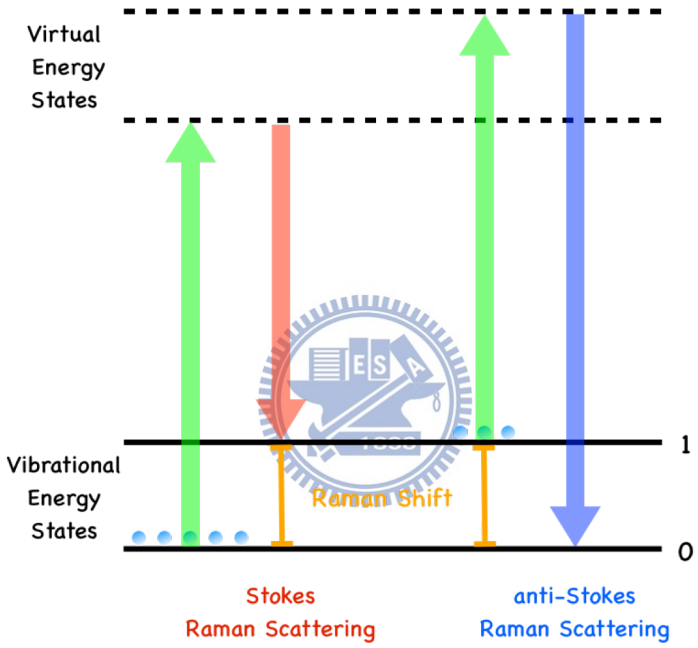

Figure I-1. Origin of Stokes and anti-Stokes Raman scattering.

Raman Shift (cm^{-1})	Temperature (K)							
	100	300	500	700	900	1100	1300	1500
200	0.056	0.383	0.562	0.663	0.726	0.769	0.801	0.825
400	0.003	0.147	0.316	0.439	0.528	0.593	0.642	0.681
800	0.000	0.022	0.100	0.193	0.278	0.351	0.413	0.464
1600	0.000	0.000	0.010	0.037	0.077	0.123	0.170	0.216
3200	0.000	0.000	0.000	0.001	0.006	0.015	0.029	0.046

Table I-1. Intensity ratios of anti-Stokes and Stokes Raman bands. [14]

I-3. Importance of Detecting of Molecular Orientation

Molecular orientation represents how constituent molecules align three-dimensionally. It is a very important physical property that affects the packing of molecules in crysyals, mechanical properties of polymers [15, 16], device performance of organic light-emitting diodes (OLEDs) [17], membrance bio-physics [18, 19], etc. X-ray diffraction has been commonly used to precisely determine the molecular alignment in a single crystal. However, X-ray diffraction is not a panacea for crystal orientation when the target crystal has domain structures or twinning as well as when high-quality singles crystals are unavailable. Some fluorescent dyes help to visualize molecular orientaitons in biological samples, but they are applicable only to certain functional groups [18]. Coherent anti-Stokes Raman scattering (CARS) [20] and polarized Raman measurements [21] have been employed for studying molecular orientation as well. Unfortunately, intramolecular vibrations are not informative enough toward molecular ensemble structures. Thus, there has been an increasing demand for an alternative method for detecting molecular orientation and the method we present in this thesis, low-frequency Raman spectroscopy, is one of the promising candidates.

I-4. Organization of This Thesis

The rest of this thesis is organized as follow. In Chapter II, the author introduces a laboratory-built low-frequency Raman microspectromester, including its working principles and performance. In Chapter III, the laboratory-built low-frequency Raman spectromester is applied

to *in-situ* study of the transformation of crystal polymorphs of 1,1′-binaphthyl. By discussing the low-frequency Raman bands together with high-frequency Raman bands, the information about crystal structures is obtained. In Chapter IV, the author demonstrates low-frequency Raman microspectroscopy as a novel approach to crystal structure analysis by using 1,1′-binaphthyl crystals. Constructing Raman images of low-frquency bands can selectively visualize the crystal polymorphs. Moreover, detection of molecular orientation distributions within the crystal by calculating intensity ratio of low-frequency Raman bands will be discussed as well.

References for Chapter I.

[1] M. Born and K. Huang, *Dynamical theory of crystal lattices*: Oxford : Clarendon Press, 1954.

[2] R. Loudon, "The Raman effect in crystals," *Advances in Physics,* vol. 50, pp. 813-864, 2001.

[3] S. P. S. Porto, P. A. Fleury, and T. C. Damen, "Raman Spectra of TiO_2, MgF_2, ZnF_2, FeF_2, and MnF_2," *Physical Review,* vol. 154, pp. 522-526, 1967.

[4] H. Takeuchi, S. Suzuku, A. J. Dianoux, and G. Allen, "Low frequency vibrations in crystalline biphenyl: Model Calculations and Raman and Neutron Spectra," *Chemical Physics,* vol. 55, pp. 153-162, 1981.

[5] K. Krebs, S. Sandroni, and G. Zerbi, "Low-Frequency Vibrations of Crystalline Biphenyl," *The Journal of Chemical Phycis*, vol. 40, pp. 3502-3506, 1964.

[6] M. Suzuki, T. Yokoyama and M. Ito, "Polarized Raman Spectra of Naphthalene and Anthracene Single Crystals," *Spectrochimica Acta Part A: Molecular Spectroscopy*, vol. 24, pp. 1091-1107, 1968.

[7] A. M. Rao, E. Richter, S. Bandow, B. Chase, P. C. Eklund, K. A. Williams, S. Fang, K. R. Subbaswamy, M. Menon, A. Thess, R. E. Smalley, G. Dresselhaus, M. S. Dresselhaus, " Diameter-Selective Raman Scattering from Vibrational Modes in Carbon Nanotubes," *Science*, vol. 275, pp. 187-191, 1997.

[8] Zhonghua Yu and L. E. Brus, "(*n*, *m*) Structural Assignments and Chirality Dpendence in Single-Wall Carbon Nanotube Raman Scattering," *Journal of Physical Chemistry B*, vol. 105, pp. 6831-6837, 2001.

[9] M. S. Dresselhaus, G. Dresselhaus, R. Saito, A. Jorio, "Raman Spectroscopy of Carbon Nanotubes," *Physics Reports*, vol. 409, pp. 47-99, 2005.

[10] J. Loader, *Basic laser Raman spectroscopy*. London: Sadtler Research Laboratories, 1970.

[11] H. Okajima and H. Hamaguchi, "Fast Low Frequency (Down to 10 cm^{-1}) Multichannel Raman Spectroscopy Using an Iodine Vapor Filter," *Applied Spectroscopy,* vol. 63, pp. 958-960, 2009.

[12] H. Okajima1 and H. O. Hamaguchi, "Unusually Long trans/gauche Conformational Equilibration Time during the Melting Process of BmimCl, a Prototype Ionic Liquid," *Chemistry Letters*, vol. 40, pp. 1308-1309, 2011.

[13] J. R. Ferraro, K. Nakamoto, and C. W. Brown, *Introductory Raman Spectroscopy*. New York: Oxford Academic Press, 2003.

[14] 濱口宏夫・平川暁子, ラマン分光法, 学会出版センター, 1988.

[15] W. Retting, "The Effect of Molecular Orientationon the Mechanical Properties of Rubber-Modified Polystyrene," *Pure & Applied Chemistry*, vol.50, pp. 1725-1762, 1978.

[16] S. A. Arvidson, K. C. Wong, R. E. Gorga and S. A. Khan, "Structure, Molecular Orientation, and Resultant Mechanical Properties in Core/Sheath Poly(lactic acid)/Polypropylene Composites," *Polymer*, vol. 53, pp. 719-800, 2012.

[17] D. Yokoyama, "Molecular Orientation in Small-Molecule Organic Light-Emitting Diodes," *Journal of Materials Chemistry*, vol. 21, pp. 19187-19202, 2011.

[18] K. Godula, M. L. Umbell, D. Rabuka, Z. Botyanszki, C. R. Bertozzi and R. Parthasarathy, "Control of the Molecular Orientation of Membrane-Anchored Biomimetic Glycopolymers," *Journal of the American Chemical Society*, vol. 131,pp. 10263-10268, 2009.

[19] K. Godula, D. Rabuka, K. T. Nam and C. R. Bertozzi, "Synthesis and Microcontact Printing of Dual End-Functionalized Mucin-like Glycopolymers for Microarray Applications," *Angewandte Chemie International Edition*, vol. 48, pp. 4973-4976, 2009.

[20] M. Zimmerley, R. Younger, T. Valenton, D. C. Oertel, J. L. Ward and E. O. Potma, "Molecular Orientation in Dry and Hydrated Cellulose Fibers: A Coherent Anti-Stokes Raman Scattering Microscopy Study," *Journal of Physical Chemistry B*, vol. 114, pp. 10200-10208, 2010.,

[21] L. M. Bellan and H. G. Craighead, "Molecular Orientation in Individual Electrospun Nanofibers Measured via Polarized Raman Spectroscopy," *Polymer*, vol. 49, pp. 3125-3129, 2008.

Chapter II.

Laboratory-Built

Fast Low-Frequency Raman Spectrometer

II-1. General Introduction

To observe low-frequency Raman signals with the conventional Raman spectrometer is not an easy task because the excitation laser output is often very broad and low-frequency Raman signals are buried under immense Rayleigh scattering. In addition, commercial notch filters usually have a broad band-rejection width, which eliminates not only Rayleigh scattering but low-frequency Raman signals. A fast multichannel low-frequency Raman spectrometer using an iodine (I_2) vapor filter was first developed by Okajima and Hamaguchi at Tokyo [1] and reconstructed by us at National Chiao Tung University [2]. The principle of this apparatus is to use a single-mode laser which has a very narrow bandwidth of output wavelength ($\leq$0.001 cm^{-1}) coupled with an iodine vapor filter [3] as an ultra-narrow notch filter. Thus, it does not block the low-frequency Raman signals. Iodine vapor has a numerous number of absorption bands due to electronic transitions [4] and their bandwidths are as narrow as 0.03 cm^{-1}. If one of these narrow and intense absorption bands of iodine can efficiently absorb light happens to absorb light exactly at the Raman excitation wavelength work, then the absorption band can function as a high-performance notch filter that removes elastic Rayleigh scattering with minimum blocking of inelastic Raman scattered light (see Figure II-1). Figure II-2 shows the two absorption lines of iodine vapor that are suitable for 514.5 and 532 nm excitation lasers.

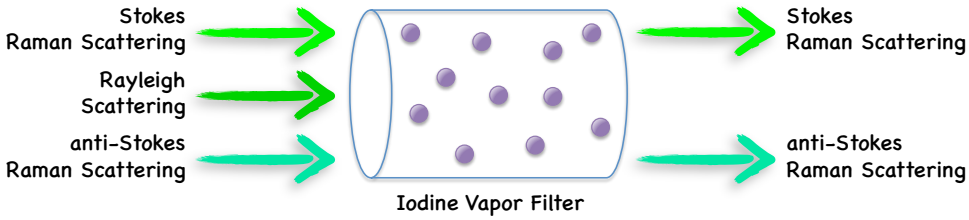

Figure II-1. Gaseous iodine molecules can efficiently absorb unwanted Rayleigh scattering and only the wavelength-shifted Raman signals pass through it.

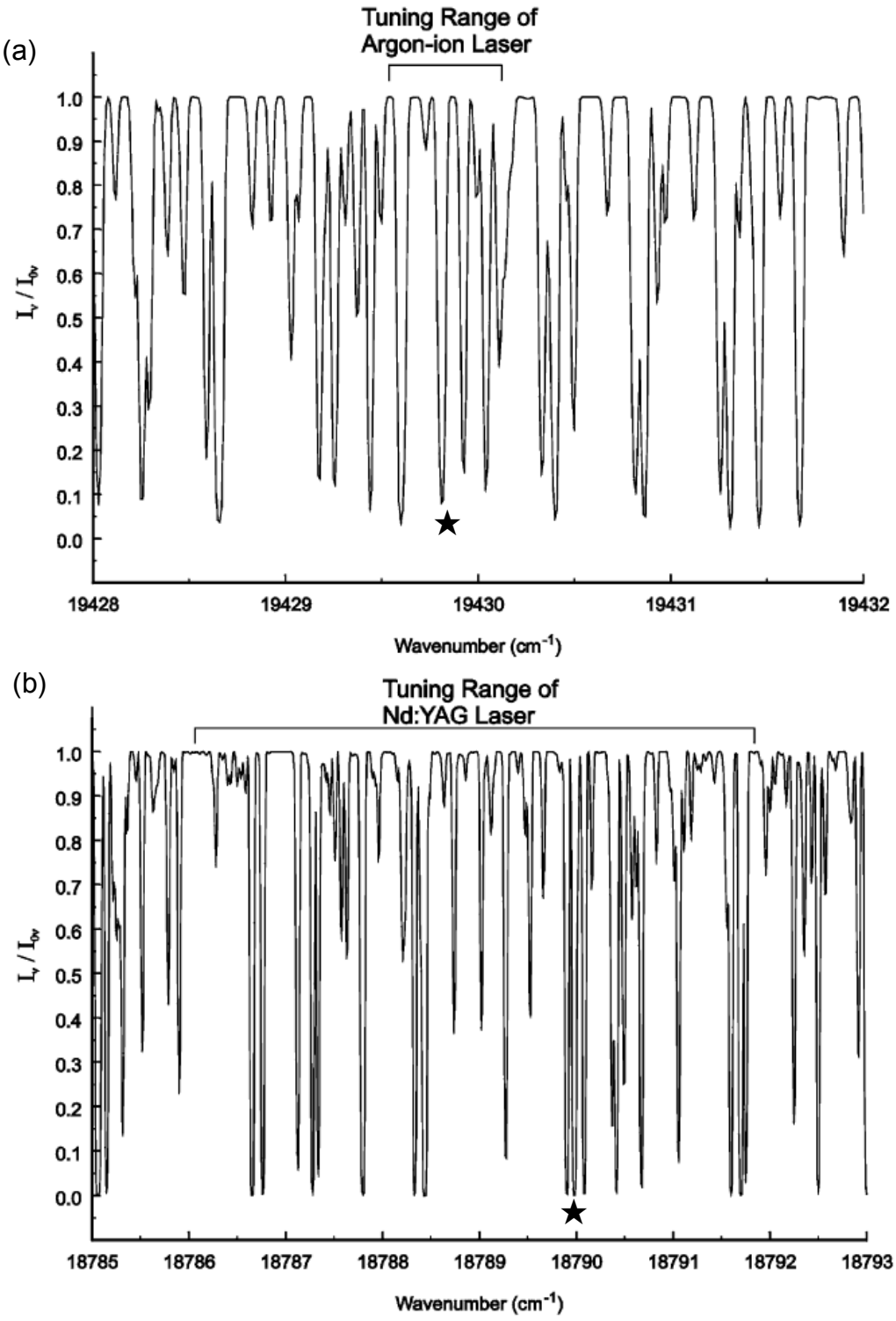

Figure II-2. Calculated absorption lines of I_2 in the visible frequency region accessible by (a) Ar^+-ion (514.5 nm), (b) Nd:YAG (532.0 nm) lasers [5]. The 19429.82 cm^{-1} and 1889.90 cm^{-1} absorption lines (marked by stars) are used for laser line elimination of the single-mode Ar^+-ion laser and Nd:YAG laser, respectively.

Recently, OptiGrate launched a new line of optical notch filters based on Bragg's diffraction law, named BragGrate™ notch filters (BNFs) [4]. By precisely calculating the angle between the incident light and filter surface, BNFs is capable of reflecting a certain wavelength of light with a bandwidth as narrow as 10 cm^{-1}. We used either a home-built iodine vapor filter or BNFs with single-mode lasers and achieved observation of Raman signals down to 9.8 cm^{-1}.

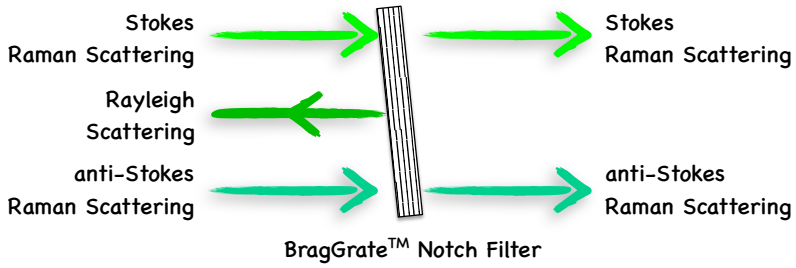

Figure II-3. The BragGrate™ notch filter can reflect a given wavelength of light (Rayleigh scattering) and other wavelengths (Raman scattering) pass through it.

The iodine vapor filter and BNFs have both pros and cons. For example, the iodine vapor filter can more efficiently eliminate Rayleigh scattering (OD≥6) and has a larger aperture (diameter = 5 cm) than BNFs. The larger aperture has a practical advantage because it is easier for alignment and suitable for use in both conventional 90° scattering setup and confocal Raman microscope system. Despite these advantages, the Raman spectra acquired with the iodine vapor filter are suffered from the artifacts due to the rotational and vibrational absorption of iodine molecules. Correction of the artifacts is required every time after experiments. In contrast with the iodine vapor filter, the BNFs are free from the annoying artifacts and have higher transmittance for Raman signals. However, the optical density of one BNF is three orders of magnitude smaller (OD≈3), so at least two BNFs is required to reach the same Rayleigh

scattering elimination efficiency as the iodine vapor filter. Moreover, the elimination efficiency of BNF is very sensitive to the incident angle. Therefore, the alignment of the BNFs is critical and at present only compatible with the confocal Raman system. Figure II-4 shows typical transmittance spectra of the iodine vapor filter and BNFs. The absorption band of the iodine vapor filter used to eliminate Rayleigh scattering cannot be observed in this spectrum because the bandwidth (0.03 cm^{-1}) is too narrow to be distinguished compared with the spectral resolution (2.7 cm^{-1}).

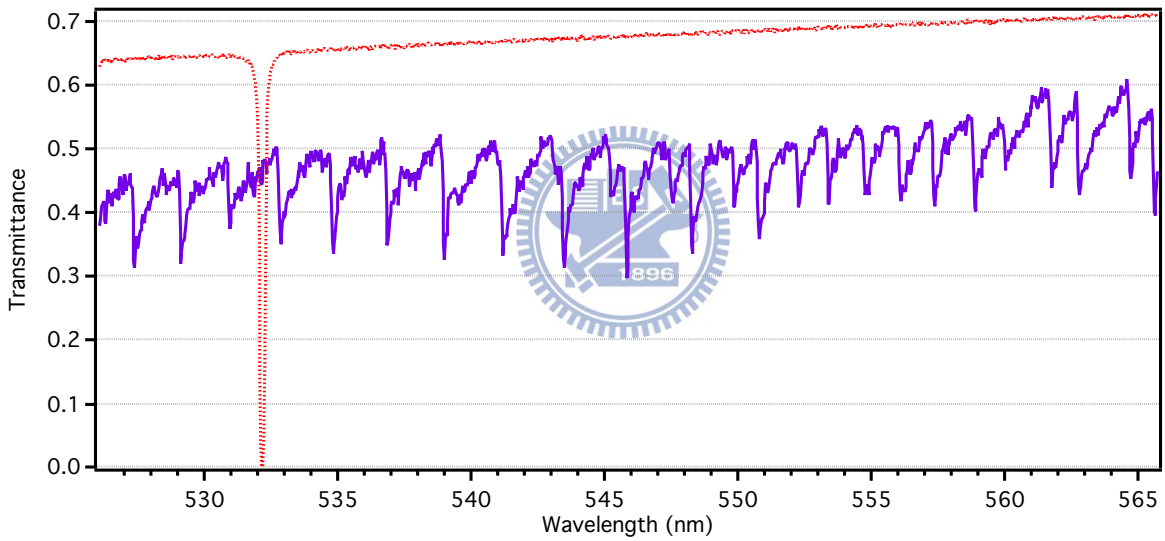

Figure II-4. Transmittance spectra of the iodine vapor filter operated at 60 °C (solid line) and combination of two BragGrate^{TM} notch filters (dotted line).

In this study, we used two fast low-frequency Raman spectrometers equipped with different lasers, that is, a single-mode Ar^{+}-ion gas laser (514.5 nm) and a single-mode Nd-YVO_4 solid-state laser (532 nm), and details of the two spectrometers are described below.

II-2. Fast Low-Frequency Raman Spectrometer Using a Single-Mode Ar^+-ion Laser (514.5 nm)

II-2-1. Apparatus

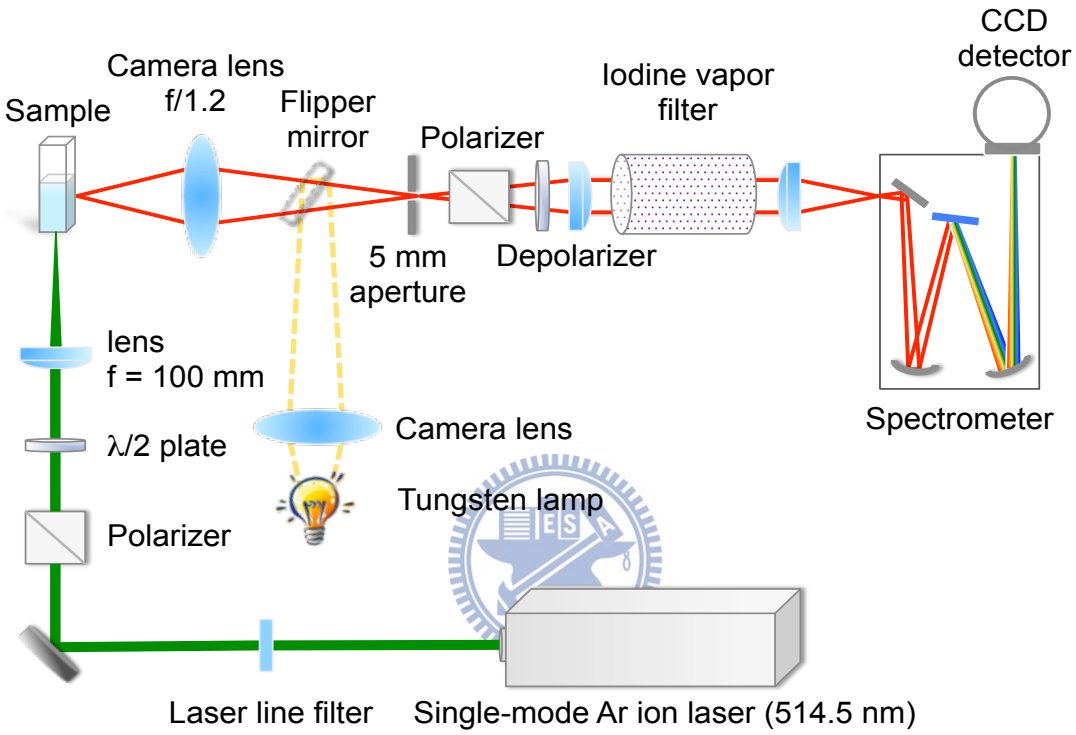

Figure II-5. Schematic diagram of the low-frequency Raman spectrometer with 514.5 nm excitation.

A schematic diagram of the 514.5 nm apparatus is shown in Figure II-5. An argon ion laser (BeamLok 2060, Spectra Physics) with a 514.5 nm output wavelength was used as the excitation source and focused on the sample cell. The scattered light was collected at 90° by a camera lens (f = 50 mm, *f*/1.2, Nikon), then focused on a 5 mm aperture to block strong reflected light from the sample cell. The collimated light passed through the iodine vapor filter operating at 95 °C, which filtered out almost all Rayleigh scattering. The transmitted light was further

focused onto the entrance slit (50 μm) of a spectrometer (f = 500 mm, *f*/6.5, SP-2558, Princeton Instruments) and dispersed by a 1200 g/mm grating, which covers a wide spectral range (>1300 cm^{-1}) with a high spectral resolution of 2.7 cm^{-1}. The dispersed light was finally detected by a back-illuminated, liquid-N_2 cooled CCD detector (Spec 10:100 B, Princeton Instruments) with 100×1340 pixels operating at −120 °C.

White light from a tungsten lamp was monitored before and after each measurement to correct the rotational-vibrational absorption of the iodine vapor. In order to direct the white light into the filter with good position reproducibility, a motorized flipper mirror and an aperture needed to be placed in front of the iodine vapor filter.

II-2-2. Low-Frequency Raman Measurement of L-Cystine

In this section, we demonstrate the ability of the apparatus to clearly detect the Raman bands at 9.8 cm^{-1} in both Stokes and anti-Stokes region. L-Cystine was chosen to be a standard sample due to its many low-frequency Raman bands. The Raman spectrum of micro-crystalline powder L-cystine is shown in Figure II-6. L-Cystine was purchased from Wako Pure Chemical Industries (99% pure) and used without further purification. As can be seen from the inset of Figure II-5(c), the lowest Raman band of L-cystine at 9.8 cm^{-1} is clearly observed. Moreover, the most intense Raman band of L-cystine located at 498 cm^{-1} has nearly the same area intensity as that of the remaining Rayleigh scattering band at 0 cm^{-1}, which can help us to check the Rayleigh elimination efficiency of the iodine vapor filter.

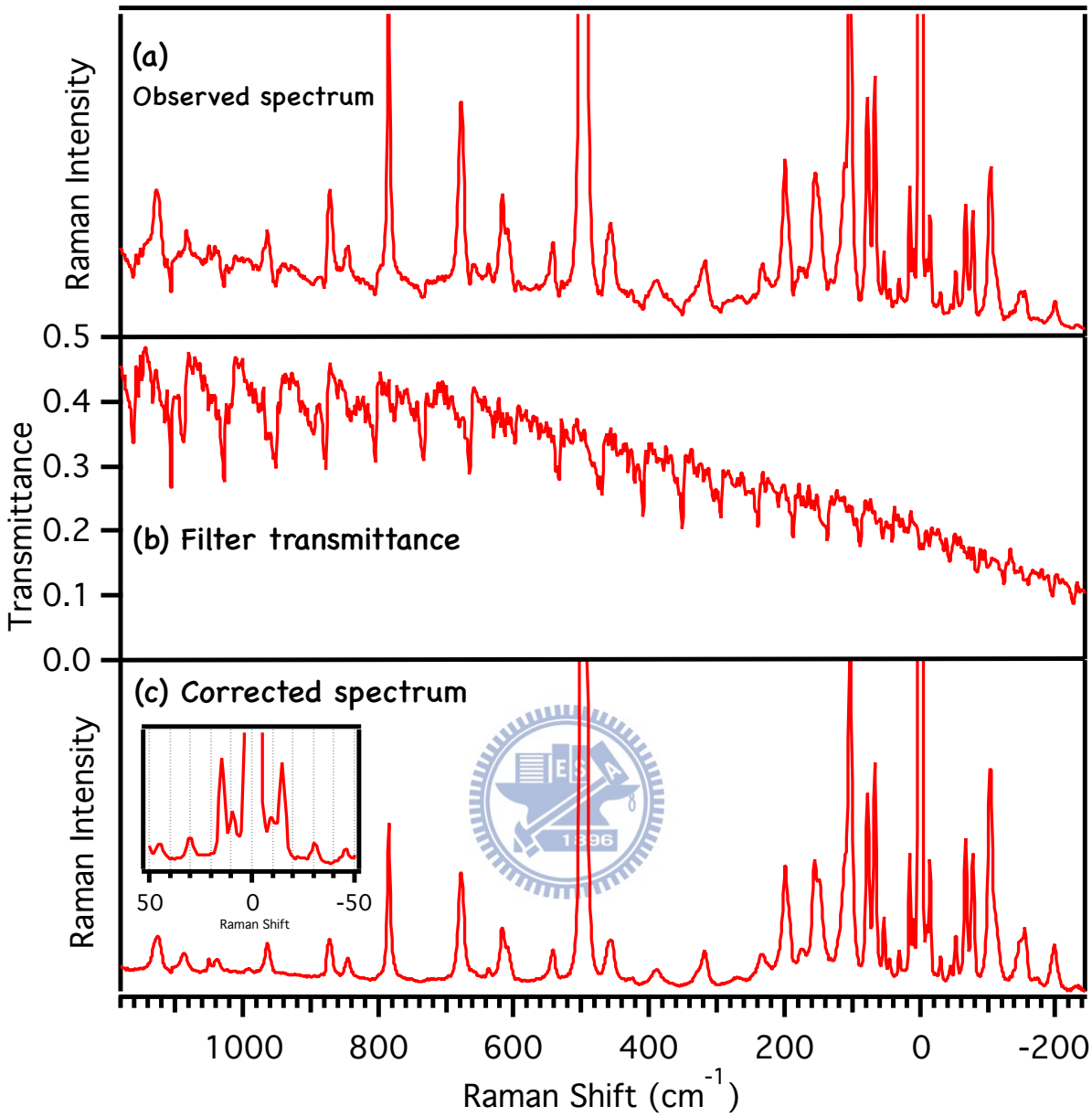

Figure II-6. Raman spectra of L-cystine.

(a) Observed Raman spectrum of L-cystine.

(b) Transmittance spectrum of the iodine vapor filter.

(c) Intensity corrected Raman spectrum of L-cystine (= a/b).

The measurement was done with 2.7 cm^{-1} spectral resolution, 1 s exposure time, and 68 mW laser power.

II-3. Fast Low-Frequency Raman Spectrometer Using a Single-Mode Solid-State Laser (532 nm)

Nowadays, diode-pumped solid-state (DPSS) lasers have been widely used in Raman measurements to replace gas lasers because they have higher output power, better stability and smaller size. Here, we used a DPSS laser with 532 nm output wavelength. The iodine vapor filter can eliminate a laser line at 532 nm more efficiently than the argon ion laser line (514.5 nm). This high elimination efficiency at 532 nm allows us to decrease the operation temperature of the iodine vapor filter and increase the transmittance of the Raman signals. In addition, the operating frequency of the DPSS laser is monitored by a wavelength meter, and fixed exactly to the absorption band of the iodine vapor filter. Together, the system with the DPSS laser (532 nm) has better stability and higher efficiency than that with the argon ion laser (514.5 nm).

In this system, besides the conventional 90° scattering setup discussed in the last section, an optical microscope and a 2-axis motorized stage were introduced to construct a confocal low-frequency Raman microspectrometer, which enables us to investigate the sample under the microscope and acquire its Raman images. For the confocal Raman microscope system, both iodine vapor filter and BragGrate^{TM} notch filters can be utilized.

II-3-1. Apparatus

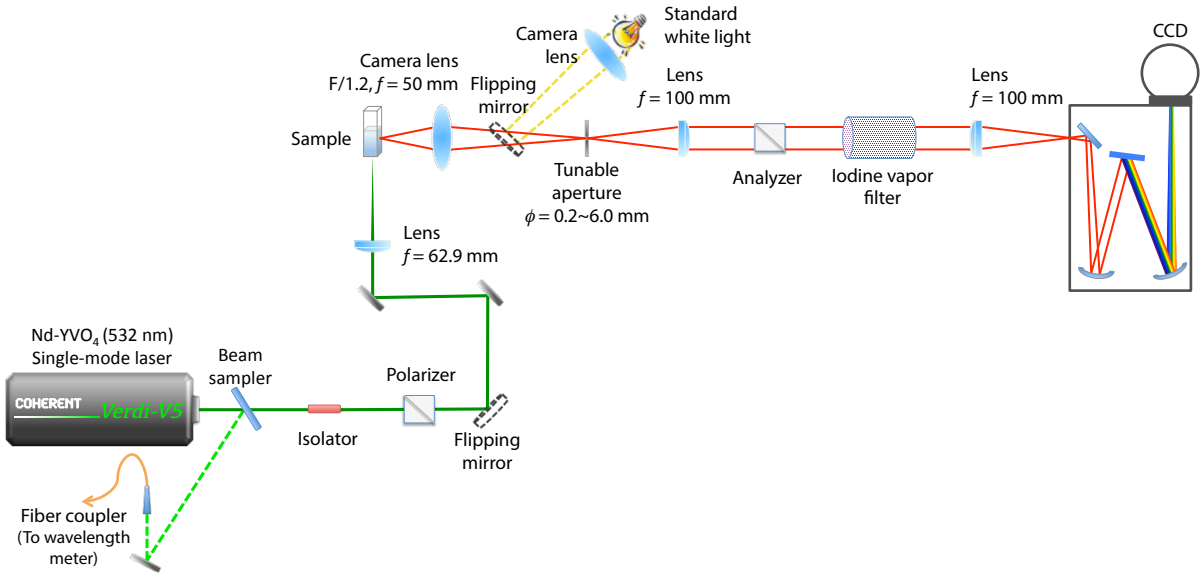

Figure II-7. Schematic diagram of the low-frequency Raman spectrometer (532 nm excitation) with 90° scattering setup.

Low-Frequency Raman Spectrometer with 90° Scattering Setup (532 nm)

A schematic diagram of the 532-nm apparatus is shown in Figure II-7. A frequency-doubled Nd:YVO_4 laser (532 nm) based on a ring cavity (Verdi-V5, Coherent) was used as the excitation light source. A small portion (<5%) of the output was reflected to a high-resolution wavelength meter (WS-7, HighFinesse). The frequency of the laser line was monitored by the wavelength meter with 60-MHz accuracy and maintained at 18789.902 cm^{-1}, which coincides with the frequency of an absorption line of iodine vapor (Figure II-2 (b)). This apparatus is similar to the low-frequency Raman spectrometer with the argon ion laser introduced in section II-2. An advantage of the low-frequency Raman spectrometer described here is that the iodine vapor has better Rayleigh elimination efficiency at 532 nm than at 514.5 nm. As a result, the operation temperature of the iodine vapor filter can be decreased to 67 °C,

and the transmittance of the Raman signals increases accordingly. The scattered light from the sample was collected by a camera lens (f = 50 mm, *f*/1.2, Nikon). The collimated light was passed through the iodine vapor filter, which filtered out almost all Rayleigh scattering. The transmitted light was dispersed by the spectrometer (f = 500 mm, *f*/6.5, SP-2558, Princeton Instruments) and detected by a back-illuminated, liquid-N_2 cooled CCD detector (Spec 10:400 B, Princeton Instruments) with 400×1340 pixels operating at −110 °C.

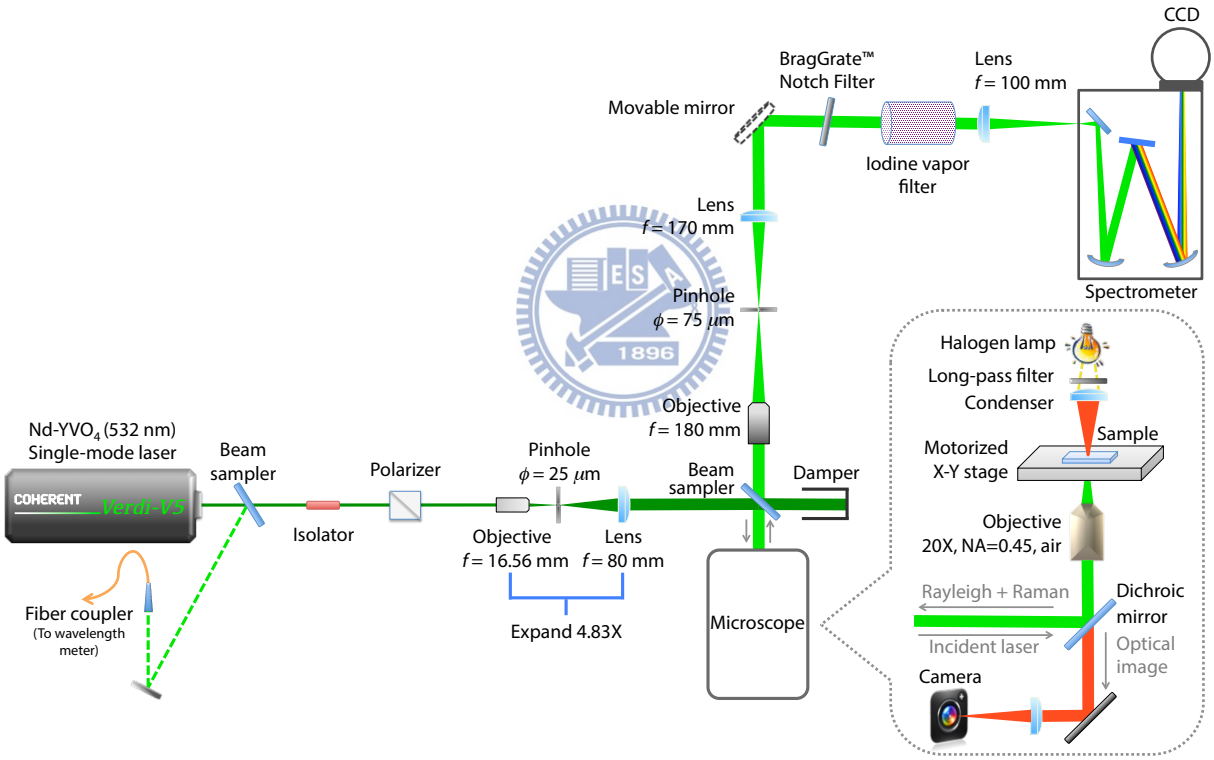

Figure II-8. Schematic diagram of the low-frequency confocal Raman spectrometer

Confocal Low-Frequency Raman Microspectrometer (532 nm)

The system is schematically shown in Figure II-8. The same laser as in the 90° scattering setup was used. In order to make full use of the numeric aperture of the objective lens, the

diameter of the laser beam was magnified from 2.25 mm to 10.87 mm by a pair of lenses. The expanded laser beam was directed to an inverted optical microscope (ix71, Olympus) and focused onto the sample by a long working distance objective (20X, NA=0.45). The sample was placed on a 2-axis motorized stage (Sigma Koki) with a minimum of 0.1 μm step of movement. The back-scattered light was collected by the same objective, and then focused by a second objective (f=180 mm) onto a pinhole (diameter = 75 μm). With this confocal configuration, the axial resolution at the sample point was increased. The well-collimated light was passed though the iodine vapor filter or BragGrate^{TM} notch filters to reject almost all Rayleigh scattering. The transmitted light was dispersed and detected by the same spectrometer and CCD detector as in the 90° scattering setup.

II-3-2. Comparison of the Filter Transmittance and Examination of Low-Frequency Measurement Capability Using L-Cystine

In the confocal Raman spectrometer system, both the iodine vapor filter and BragGrate^{TM} notch filters (BNFs) can be utilized as Rayleigh rejection filters. Compared to the iodine vapor filter, the advantage of using BNFs is not only that they can be free from the artifacts but also that the higher transmittance allows more Raman signals to pass through. The transmittance spectra of different filter sets are shown in Figure II-9. Which kind of filter set should be used during the measurement depends on the exposure time. Generally speaking, if the exposure time is short (<1 s), two BNFs can reach the best S/N ratio because of the high transmittance (>60 %). If a long exposure time (>1 min) is needed, the combination of one BNF and iodine vapor filter

can reach the best Rayleigh elimination efficiency.

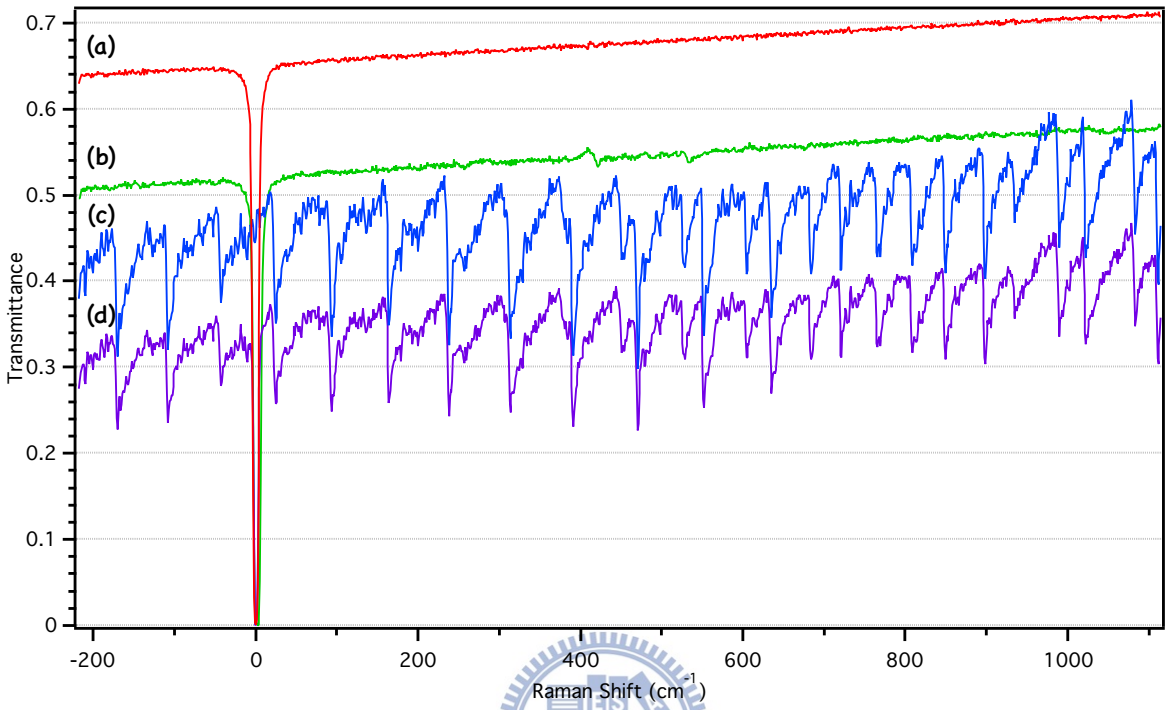

Figure II-9. Transmittance spectra of (a) two BNFs, (b) three BNFs, (c) iodine vapor filter (at 60 °C), and (d) one BNF + iodine vapor filter (at 60 °C).

As described in section II-2-2, L-cystine was employed as a standard sample to check the low-frequency measurement capability of the system. Figure II-10 shows the observed Raman spectra. In both spectra taken with either iodine vapor filter or BNFs, the ±9.8 cm^{-1} Raman band can be seen, indicating a similar low-frequency measurement capability of the BNFs to the iodine vapor filter. It is noteworthy that the observed spectrum taken with the iodine vapor filter was interfered with artifacts on the background. The band intensities are also incorrect due to the absorption of the iodine molecules. In contrast, the observed spectrum taken with three BNFs does not have these problems, so we can directly look at the spectrum without any background correction.

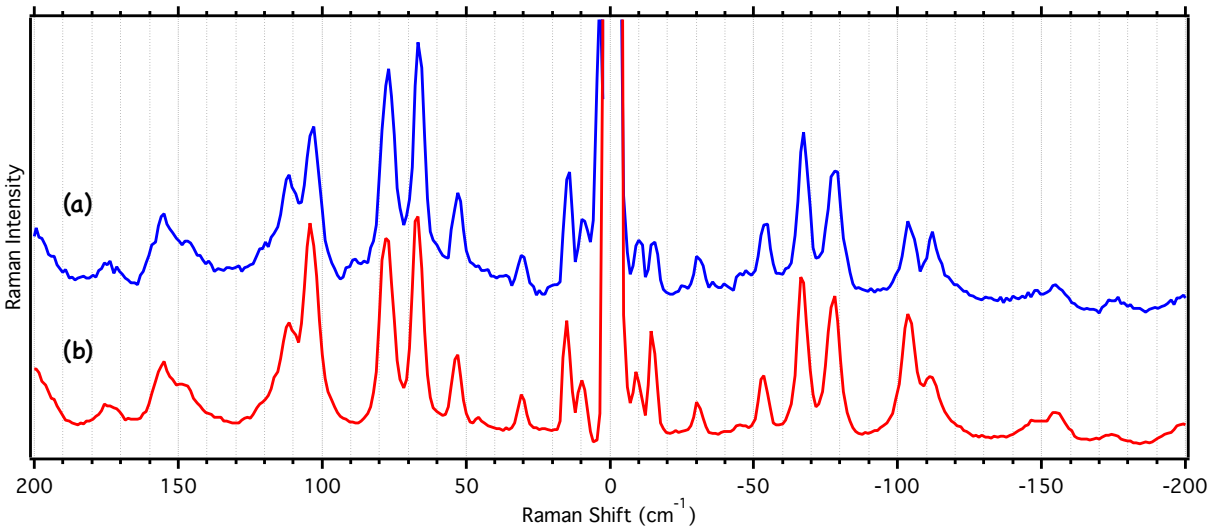

Figure II-10. Observed Raman spectra of L-cystine taken with (a) three BNFs and (b) a combination of one BNF and the iodine vapor filter. The measurement was done with 2.7 cm^{-1} spectral resolution, 10 s exposure, time and 1 mW laser power.

II-3-3. Evaluation of the Spatial Resolution of the Confocal Raman Microspectrometer

The spatial resolution of the confocal system is governed by an objective lens and the confocal pinhole. The lateral (XY) resolution was determined by scanning the focused laser beam horizontally with a step of 0.2 μm across a spherical polystyrene bead with 1 μm diameter. The Raman band intensity of polystyrene at 1003 cm^{-1} was used to estimate the lateral resolution. Figure II-11 (a) displays the band intensity of polystyrene at 1003 cm^{-1} versus the stage-scanned distance. The beam profile was assumed to be a Gaussian function and its width obtained by fitting was 0.925 μm. The lateral resolution is defined as the full-width at half-maximum (FWHM) of the Gaussian width, which is equal to $2\sqrt{\ln 2}\times$Gaussian width. Therefore, the calculated lateral resolution was 1.5 ± 0.1 μm.

Likewise, the axial resolution was evaluated by scanning the focused laser beam vertically with a step of 5 μm across interfaces between air and glass and between glass and tetrachloroethylene. The Raman band intensity of tetrachloroethylene at 236 cm^{-1} was employed for evaluation of the axial resolution. The Raman intensity change at the two interfaces can be fitted by a Heaviside step function $H(x)$ convoluted with a Gaussian function $G(x)$ (Equation II-1) [7].

$$f(x,N,c,B) = N\int_{-\infty}^{\infty} H(a')G(a'-a)da' = \frac{N}{2}\left[1+erf\left(\frac{x-a}{\sqrt{2}B}\right)\right]+c \qquad (\mathbf{II-1})$$

where N is a normalization constant, a is the onset of the step function, B is the width of the Gaussian function, c represents a constant offset, and erf denotes the error function. The fitting result is shown in Figure II-11 (b). The obtained Gaussian width was 19.2 μm. The axial resolution is defined as the FWHM of the Gaussian width. Consequently, the calculated axial resolution was 32 ± 1.3 μm.

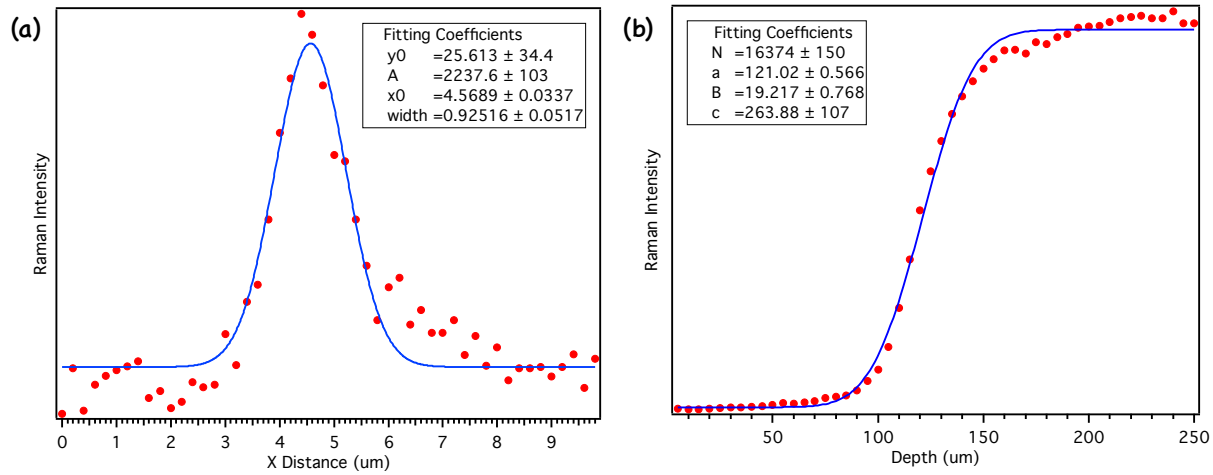

Figure II-11. Evaluation of lateral (a) and axial (b) resolution of the low-frequency confocal Raman microspectrometer. Red dots represent observed Raman intensities and blue curves represent fitted lines.

II-3-4. Development of the Low-frequency Raman Mapping Program

Since the low-frequency confocal Raman microspectrometer system is equipped with a 2-axis motorized stage and an optical microscope, it is possible to control the movement of the stage by a computer and acquire spectra synchronously (Figure II-12).

Our low-frequency Raman mapping program was developed on LabVIEW 2012 (National Instruments). This program sends commands to the stage controller (SHOT-702, Sigma Koki) then moves the motorized stage with a minimum of 0.1 μm step. The stage was programmed to move in a zigzag way, as depicted in Figure II-13 (b). After moving each step, the stage stops for a while to wait for CCD exposure. At this moment, the program sends a transistor-transistor-logic (TTL) signal to the CCD controller (ST-133, Princeton Instruments) and triggers CCD exposure. Acquisition of Raman spectra is done with Winspec/32 software provided by Princeton Instruments. Consequently, it is necessary to run the LabVIEW program and Winspec/32 software simultaneously when doing Raman mapping.

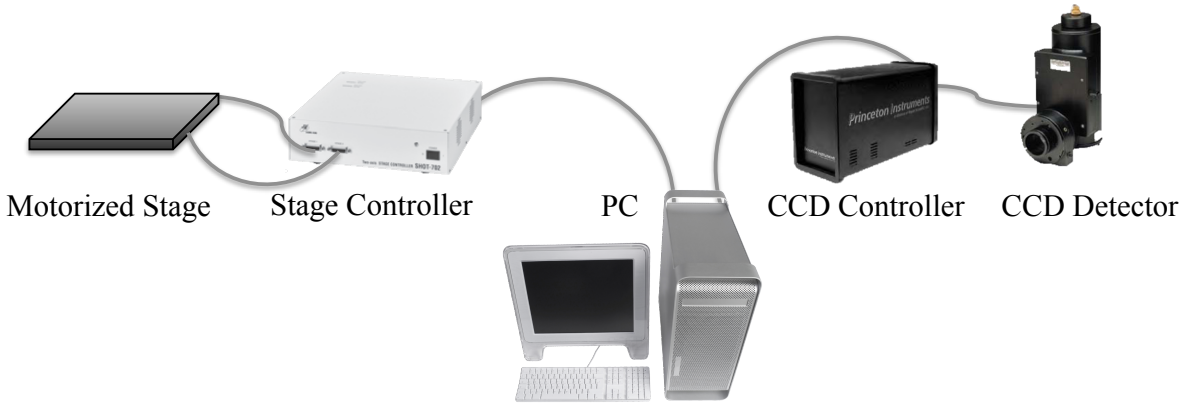

Figure II-12. Schematic layout of the Raman imaging system.

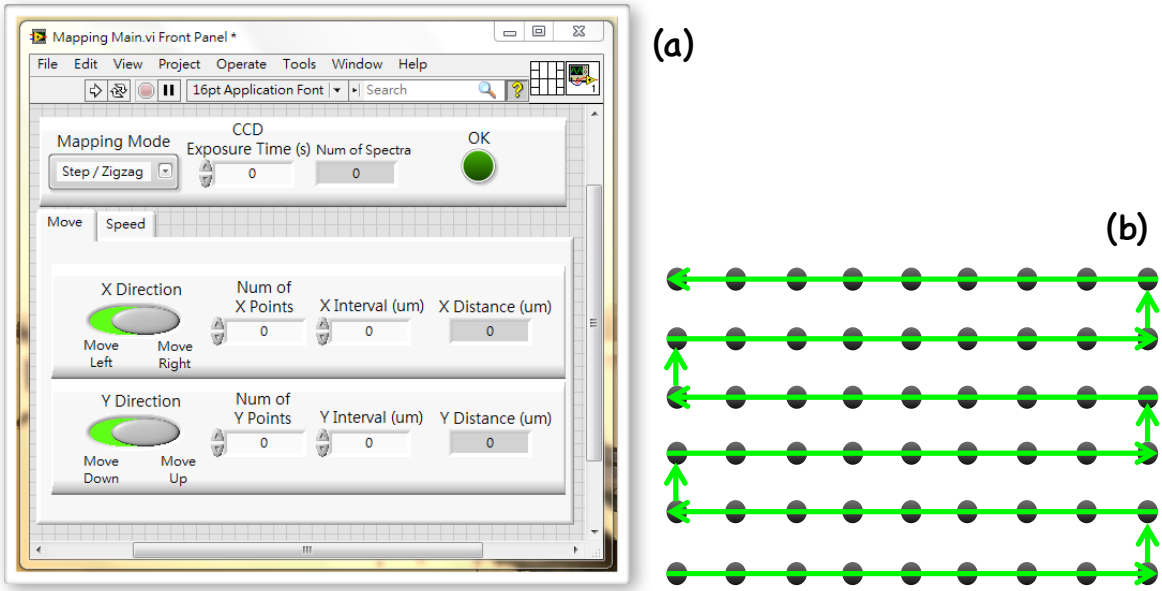

Figure II-13. (a) Developed user interface of the mapping program in LabVIEW 2012. (b) Stage movement during mapping.

References for Chapter II.

[1] H. Okajima and H. Hamaguchi, "Fast Low Frequency (Down to 10 cm^{-1}) Multichannel Raman Spectroscopy Using an Iodine Vapor Filter," *Applied Spectroscopy,* vol. 63, pp. 958-960, 2009.

[2] Szu-Cheng Wang, "Construction of a Fast Low-Frequency Raman Spectrometer and Its Application to Real-Time Tracing of Melting Process of Crystalline 1,1'-binaphthyl," *National Chiao Tung University*, Master Thesis, 2011.

[3] G. E. Devlin, J. L. Davis, L. Chase, and S. Geschwind, "Absorption of Unshifted Scattered Light by a Molecular I_2 Filter in Brillouin and Raman Scattering," *Applied Physics Letters,* vol. 19, pp. 138-141, 1971.

[4] W. L. Peticolas, "Inelastic Light Scattering and the Raman Effect," *Annual Review of Physical Chemistry,* vol. 23, pp. 93-116, 1972.

[5] Gregory S. Elliott and Thomas J. Beutner, "Molecular Filter Based Planar Doppler Velocimetry," *Process in Aerospace Science*, vol. 35, pp. 799-845, 1999.

[6] Alexei L. Glebov, Oleksiy Mokhun, Alexandra Rapaport, Sébastien Vergnole, Vadim Smirnov, Leonid B. Glebov, "Volume Bragg Gratings as Ultra-Narrow and Multiband Optical Filters," *Proceedings of SPIE*, vol. 8428, pp. 84280C-1-84280C-11, 2012.

[7] V. V. Pully, and C. Otto, "The Intensity of 1602 cm^{-1} Band in Human Cells is Related to Mitochondrial Activity," *Journal of Raman Spectroscopy*, vol. 40, pp. 473-475, 2009.

Chapter III.

In-situ Tracing of the Transformation Dynamics between Crystal Polymorphs of 1,1′-Binaphthyls

III-1. Introduction to 1,1′-binaphthyls

1,1′-Binaphthyl is composed of two naphthyl groups linked via a C-C single bond at 1,1′-positions, which represents a special class of biaryl molecules. The molecule is well known for its applications as chiral recognition receptors and chiral catalysts such as 2,2′-bis(diphenylphosphino)-1,1′-binaphthyl (BINAP) [1-3]. The rotational barrier along the C-C single bond is 23.5 kcal/mol ($\Delta G^{\neq}$) [4], which is much larger than the rotational barrier of biphenyl around the phenyl-phenyl bond in the gas phase (~1.4 kcal/mol) [5]. The large rotational barrier is attributed mainly to the repulsion of the hydrogen atoms at the 8 and 8′ positions. Besides, 1,1′-binaphthyl no longer possesses a plane of symmetry that biphenyl has in its perpendicular conformation, resulting in axial chirality of the molecule. This fact allows the isolation of the optically active 1,1′-binaphthyl enantiomers.

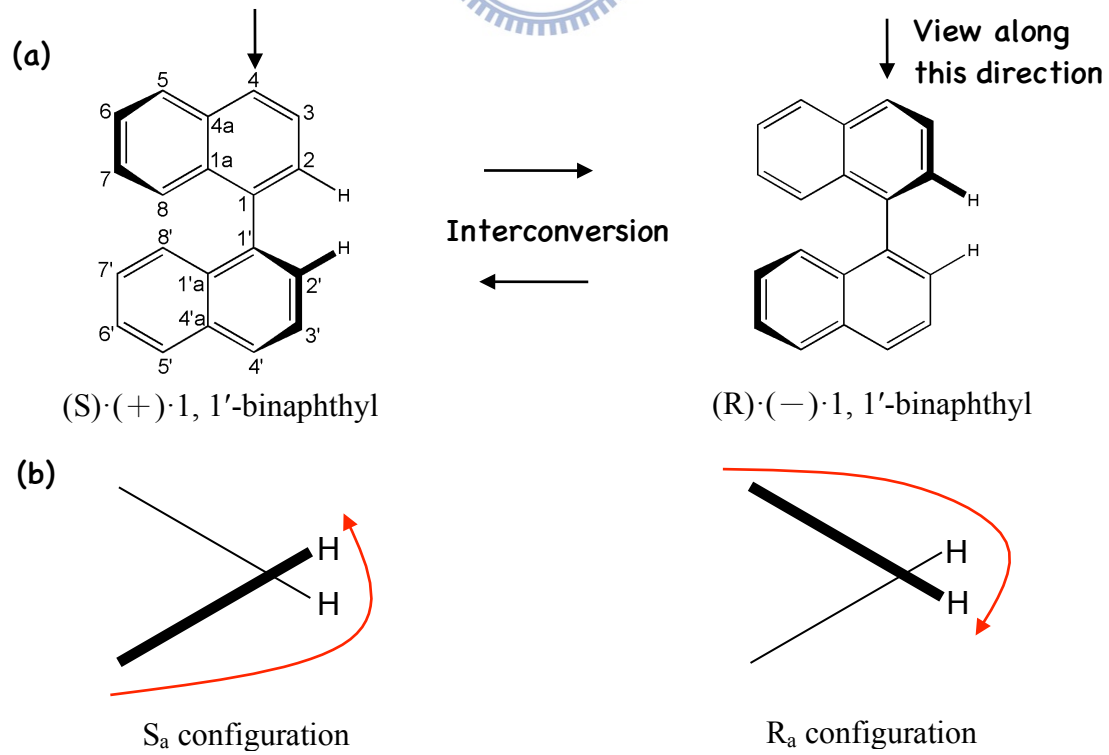

Figure III-1. Axial chirality of 1,1′-binaphthyl.

The asymmetry of 1,1′-binaphthyl is molecular in nature, and enantiomeric interconversion is made possible simply by rotation about the interannular bond instead of by any bond-breaking process (Figure III-1 (a)). The racemization half-life of the enantiomers was found to be 14.5 min at 50 °C. Chiral 1,1′-binaphthyl was discovered by Pincock et al. in 1971 [6]. He found that racemic 1,1′-binaphthyl undergoes spontaneous resolution to generate the optically active R or S enantiomer when this compound crystallizes from the melt. The chiral 1,1′-binaphthyl molecule contains a chiral axis instead of a chiral center. The enantiomers of axially chiral compounds are usually given the stereochemical labels R_a and S_a as shown in Figure III-1 (b).

In the crystalline state, 1,1′-binaphthyl is known to occur as two polymorphs [7]: the cisoid configuration or lower melting point (148 °C) form and the transoid configuration or higher melting point (161 °C) form. Brown et al. [8] were the first to recognize the fundamental difference between the two forms. They found that the molecules of the lower melting point form take a cisoid configuration. X-ray diffraction [9] confirmed the dihedral angle θ to be 68.6° (Figure III-2). Badar et al. [7] suggested, on the basis of their infrared spectroscopic results, that the high melting point form adopts a transoid configuration, which was later confirmed by X-ray analysis [10] to have a dihedral angle of 103.1°. The cisoid form, whose structure was determined by Kerr and Robertson [9], consists of racemic monoclinic crystals (space group *C*2/c). A unit cell of this achiral crystal is comprised of two R enantiomers and two S enantiomers, i.e., Z = 4. On the other hand, Kress et al. [10] reported the crystal structure of the

transoid form as an optically active compound which belongs to the tetragonal system of space group $P4_12_12_1$ with either R or S enantiomer in a unit cell (Z = 4).

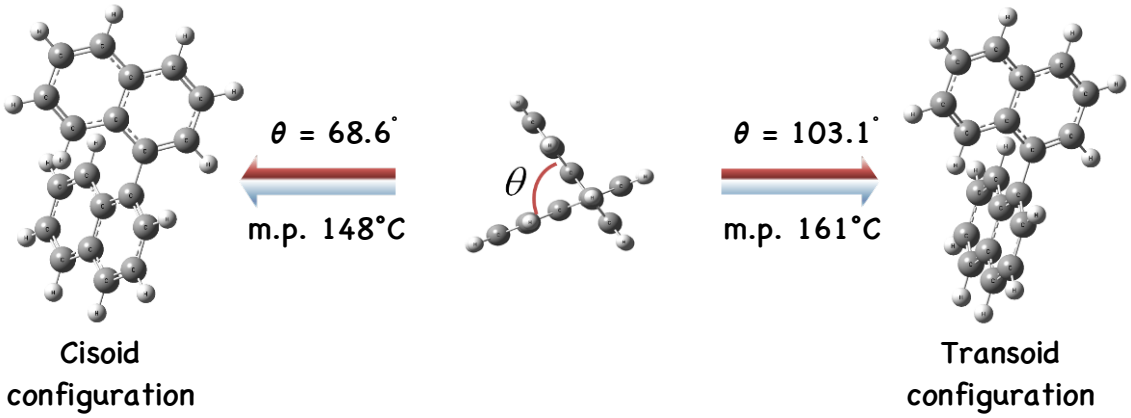

Figure III-2. Schematic diagram of the two crystal forms of 1,1′-binaphthyl.

Extensive studies on the structural change of the ground and excited states of 1,1′-binaphthyl in the solution phase have been done by absorption spectroscopy [11, 12], fluorescence spectroscopy [13, 14], and Raman spectroscopy [14-16]. Also there are some theoretical studies, in which the dihedral angle adopted by the 1,1′-binaphthyl molecule in its most stable conformation was estimated [17-23].

The first report on the two crystal forms of 1,1′-binaphthyl in the viewpoint of Raman spectroscopy was provided by Lacey et al. [15]. However, the Raman spectra of the cisoid and transoid form in the low-frequency region (<150 cm^{-1}) have not been reported yet. In this study, we are interested to see how different are the spectral patterns in the low-frequency region of the different crystal structures of 1,1′-binaphthyl. Then we can use these differences to monitor the transformation dynamics between the cisoid and transoid forms. Moreover, the low-frequency Raman imaging technique can be applied to differentiate the two crystal forms on a molecular

basis and to reveal spatial distributions of molecular orientations inside the crystal, both of which can hardly be realized with any other existing methods.

III-2. Preparation of the Cisoid and Transoid Form

1,1′-Binaphthyl powder with 98% purity, which is dominated by the cisoid form, was purchased from Tokyo Chemistry Industry Co., LTD. Unknown impurities may cause strong fluorescence in the Raman spectrum measured with 514.5 and 532 nm excitations. In order to get rid of possible fluorescent impurities, column chromatography was used to purify the commercially obtained 1,1′-binaphthyl (Figure III-3).

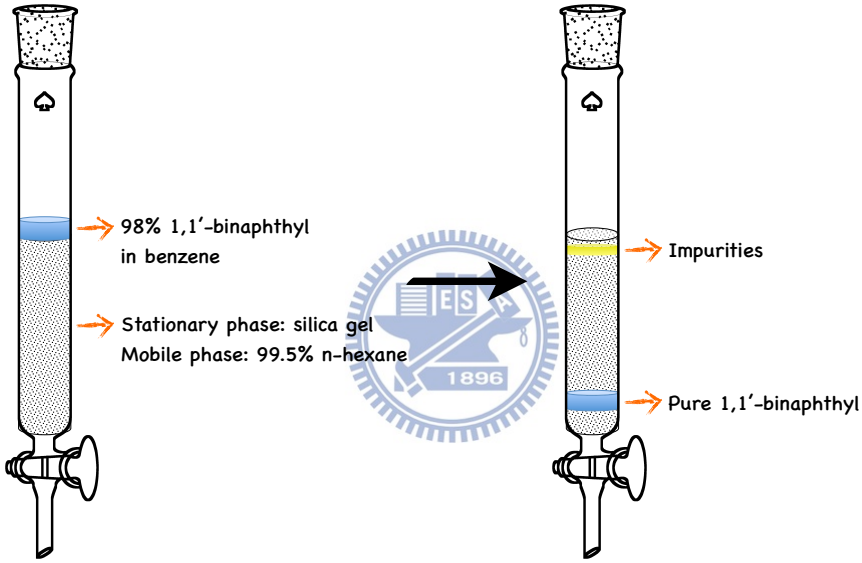

Figure III-3. Column chromatography purification of 1,1′-binaphthyl.

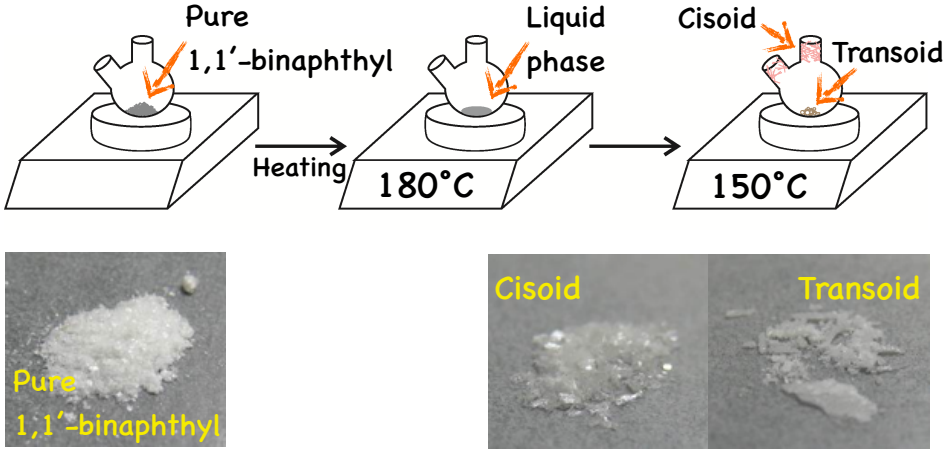

Figure III-4. Preparation of the cisoid and transoid forms.

Preparation of the cisoid and transoid crystal was followed the similar procedure reported previously [6, 24, 25, 26], figure III-4 visually describe how we prepared them. A small amount of the pure 1,1'-binaphthyl (0.35 g) was placed in a 10 ml round-bottom flask and heated up to 180 °C in an oil bath. The melt was kept in the temperature for 15 minutes to completely racemize the sample, then we cooled down the melt to 150 °C and allowed it to crystallize. After 4 hours, the sample was cooled down to room temperature. The transparent, flake-shaped cisoid crystals was found at the top of the reactor, as the result of evaporation and recrystallization of 1,1'-binaphthyl. This process is consistent with the previous literature, which claimed the transformation of these polymorphs follows vapor-solid transformation [10]. On the other hand, the white transoid solids were observed to stay at the bottom of the reactor.

To examine the purity of the cisoid and transoid crystals so obtained, differential scanning calorimetry (DSC) was applied to measure the melting point of the two crystal forms. Figure III-5 shows the DSC curves of the cisoid crystal obtained with different heating rates. The 146 °C band was observed, which represents the melting point of the cisoid form. In addition, the 160 °C band was also observed, which indicates the melting point of the transoid form. With a faster heating rate (45 °C/min), the cisoid form predominates. However, with a slower heating rate (5 °C/min), the DSC curve is dominated by the transoid form. This result implies that to observe the transformation between the cisoid and transoid forms, a slower heating rate should be used. The DSC curves of the transoid form measured with different heating rates are shown in Figure III-6. This time, the transoid form dominates in all the cases. Thus we would be unable to observe the transformation from the transoid crystal.

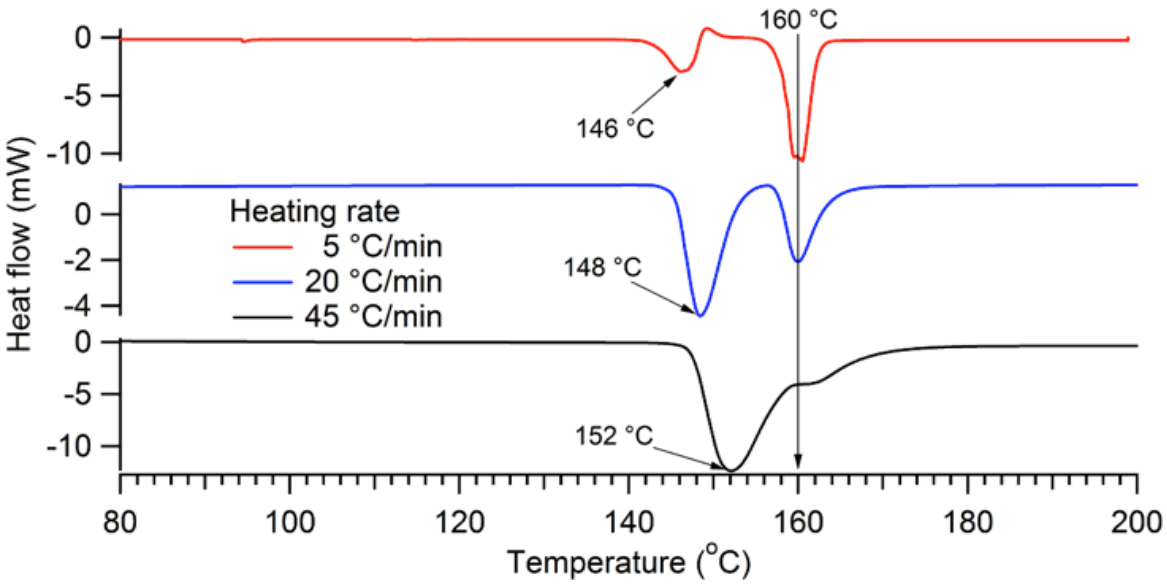

Figure III-5. Differential scanning calorimetry (DSC) measurements of cisoid form crystal with different heating rates [26].

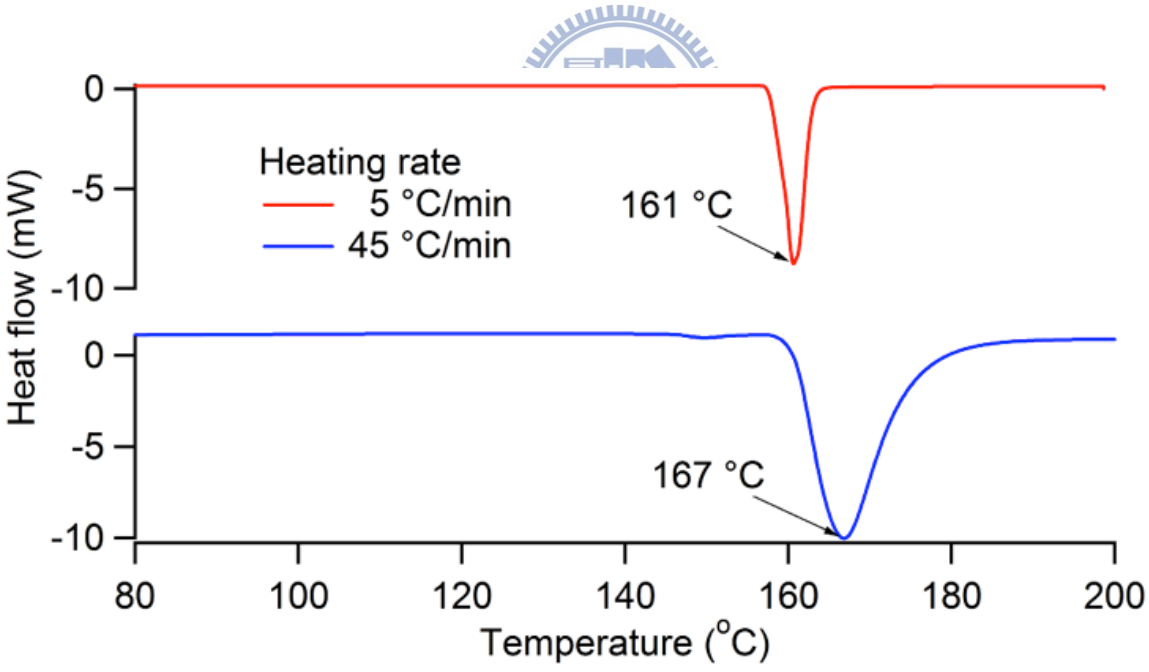

Figure III-6. Differential scanning calorimetry (DSC) measurements of transoid form crystal with different heating rates [26].

III-3. Raman Spectra of the Two Polymorphs of 1,1′-Binaphthyl

The Raman spectra of the two purified crystal powder samples measured at room temperature with 514.5 nm laser excitation and 1 second exposure time are shown in Figures III-7 and III-8. The most notable difference in the high-frequency region (200 – 1100 cm^{-1}) between the two spectra is concerned with different intensity ratios of pairs of Raman bands centered at 460, 520, 1025, and 1588 cm^{-1} [15]. The difference in the intensity ratio of a pair of the bands can be explained in terms of the weakly coupled model of the two naphthyl groups [27]. Due to the coupling, each of the bands splits into a doublet in 1,1′-binaphthyl by ~21 cm^{-1}, and the intensity ratios can reflect how these two naphthyl groups interact with each other with different dihedral angles (68.6° and 103.1°). Among those pairs of bands, the 510/532 cm^{-1} pair shows the strongest intensity; thus they are selected to be the pair of marker bands to distinguish the cisoid and transoid forms in the high-frequency region. Compared with the high-frequency region, the low-frequency region (<200 cm^{-1}) shows significantly strong signal intensities. The reason for this is that the low-frequency motions usually originate from collected motions or lattice vibrations, which give large polarizability changes that result in strong Raman signals.

Figure III-9 shows the low-frequency (−200 to +200 cm^{-1}) Raman spectra of the two polymorphs of crystalline 1,1′-binaphthyl. Decent low-frequency Raman spectra in both Stokes and anti-Stokes regions have been obtained simultaneously within 1 s. This is the first observation, to our knowledge, of the low-frequency Raman spectra of the crystal polymorphs of 1,1′-binaphthyl. In the transoid form, the 26 cm^{-1} band gives the strongest intensity in the whole spectrum. On the other hand, the cisoid form shows the most intense bands at 100 and 110 cm^{-1},

which may arise from a symmetry splitting of one band into a doublet at 100 and 110 cm^{-1}. Detailed band assignments are yet to be done, and high resolution polarized Raman measurements are required in the future.

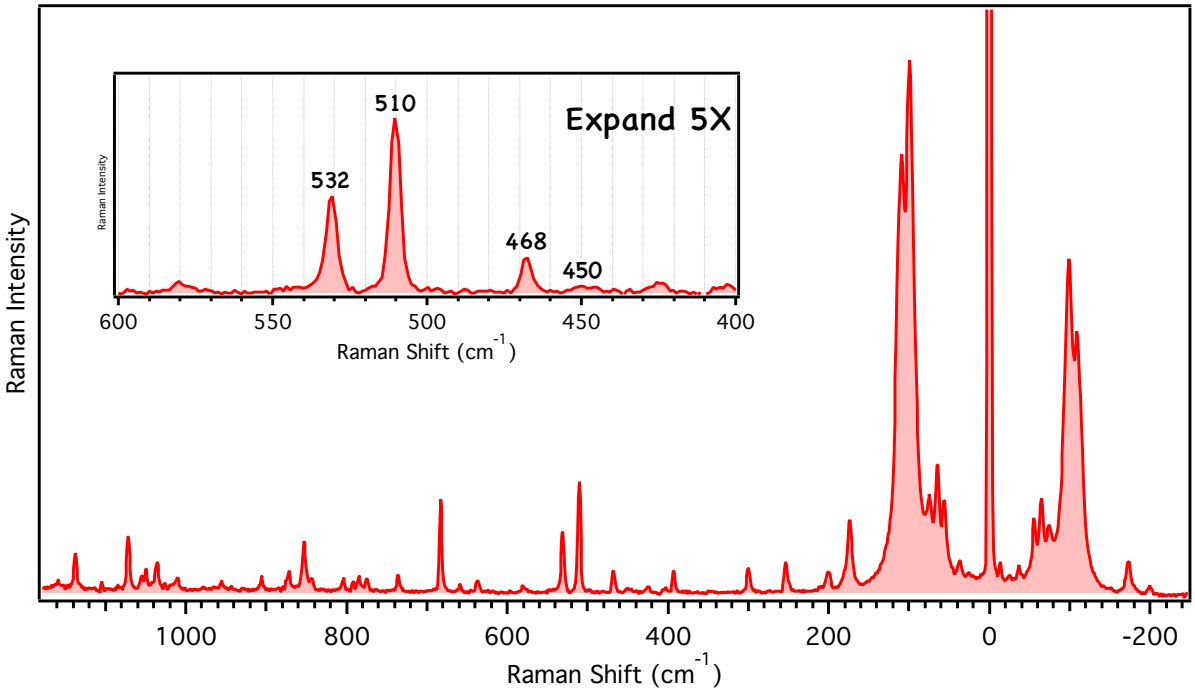

Figure III-7. Raman spectrum of the cisoid powder at room temperature.

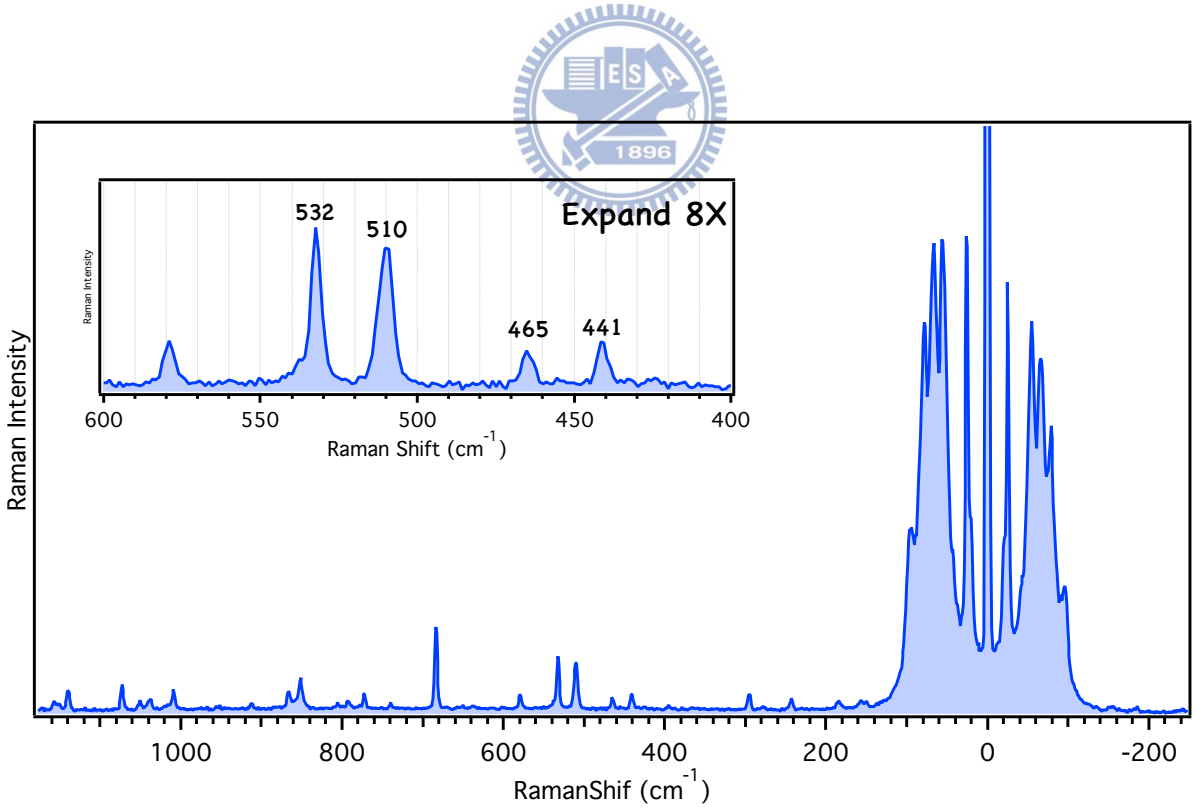

Figure III-8. Raman spectrum of the transoid powder at room temperature.

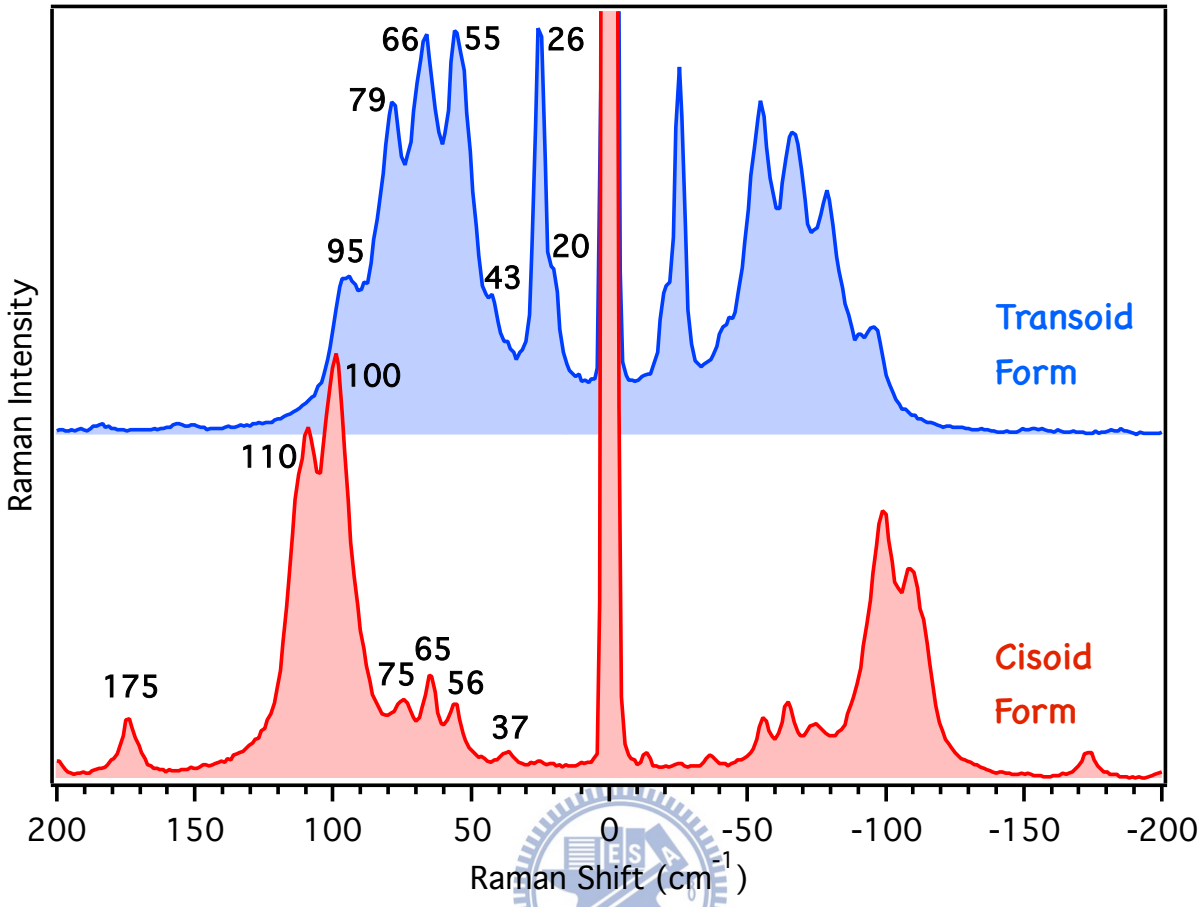

Figure III-9. Low-frequency Raman spectra of the two crystalline 1,1′-binaphthyl.

III-4. *In-situ* Tracing the Transformation between Polymorphs

Heating Apparatus

As demonstrated by the DSC measurements of the cisoid crystal (Figure III-5), we now know that when the cisoid form is heated, it transforms to the transoid form. In order to measure the Raman spectra during the transformation, we designed a heating cell.

Figure III-10 draws the design of the laboratory-built heating cell for the 90° scattering setup Raman spectrometer. It is a closed system and can be raised its temperature by heating coils inside the cell. The sample sealed in a capillary is inserted from the side port, and a thermocouple is placed beside the capillary to monitor the surrounding temperature. The laser beam is introduced from the bottom window and focused on the sample. The scattered Raman signals can be collected from the large optical window.

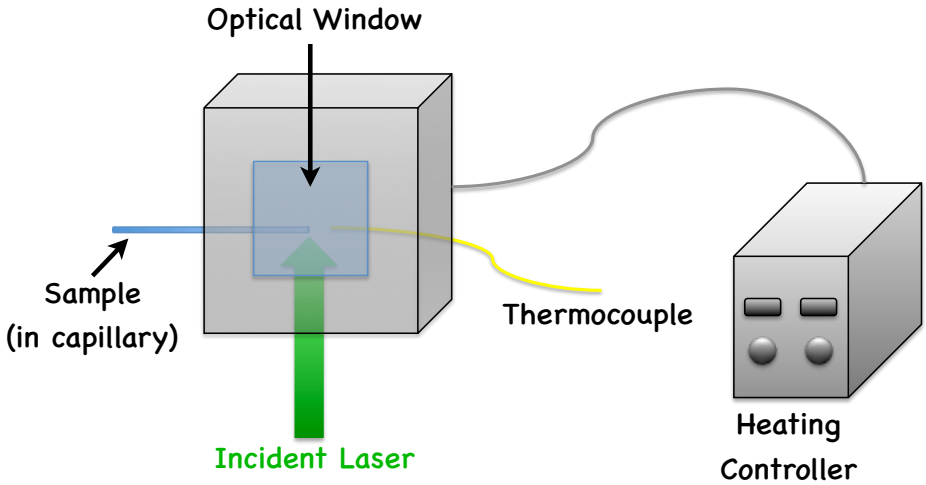

Figure III-10. Laboratory-built heating cell.

Raman Spectral Change Observed When the Cisoid Powder Was Heated

Figure III-11 shows the low-frequency (−200 to +200 cm^{-1}) Raman spectra of slowly heated cisoid powder at different temperatures. The measurement was started from room temperature, and the sample was heated up with a rate of 3 °C/min. When the temperature reached to the desired value, we waited another 1 minute to ensure that thermal equilibrium was reached and then acquired the Raman spectrum. As the temperature increases, all Raman bands shift to lower frequencies. At 126 °C, the Raman band located at 26 cm^{-1}, which is a low-frequency marker band for the transoid form starts to appear. In other words, the transformation from the cisoid to transoid form takes place at this temperature. After 138 °C, the cisoid was totally transformed into the transoid form. The transoid form melts at 156 °C, which is in agreement with the literature [7].

Compared to the low-frequency region, the spectral pattern in the higher frequency region (Figure III-12) does not change significantly. The only difference is the intensity ratios of three pairs of Raman bands: 450/468 cm^{-1}, 510/532 cm^{-1} and 1010/1035 cm^{-1}. From these results, we can conclude that the low-frequency Raman bands are more sensitive to the structural change, exhibiting much more notable differences than the high-frequency Raman bands do.

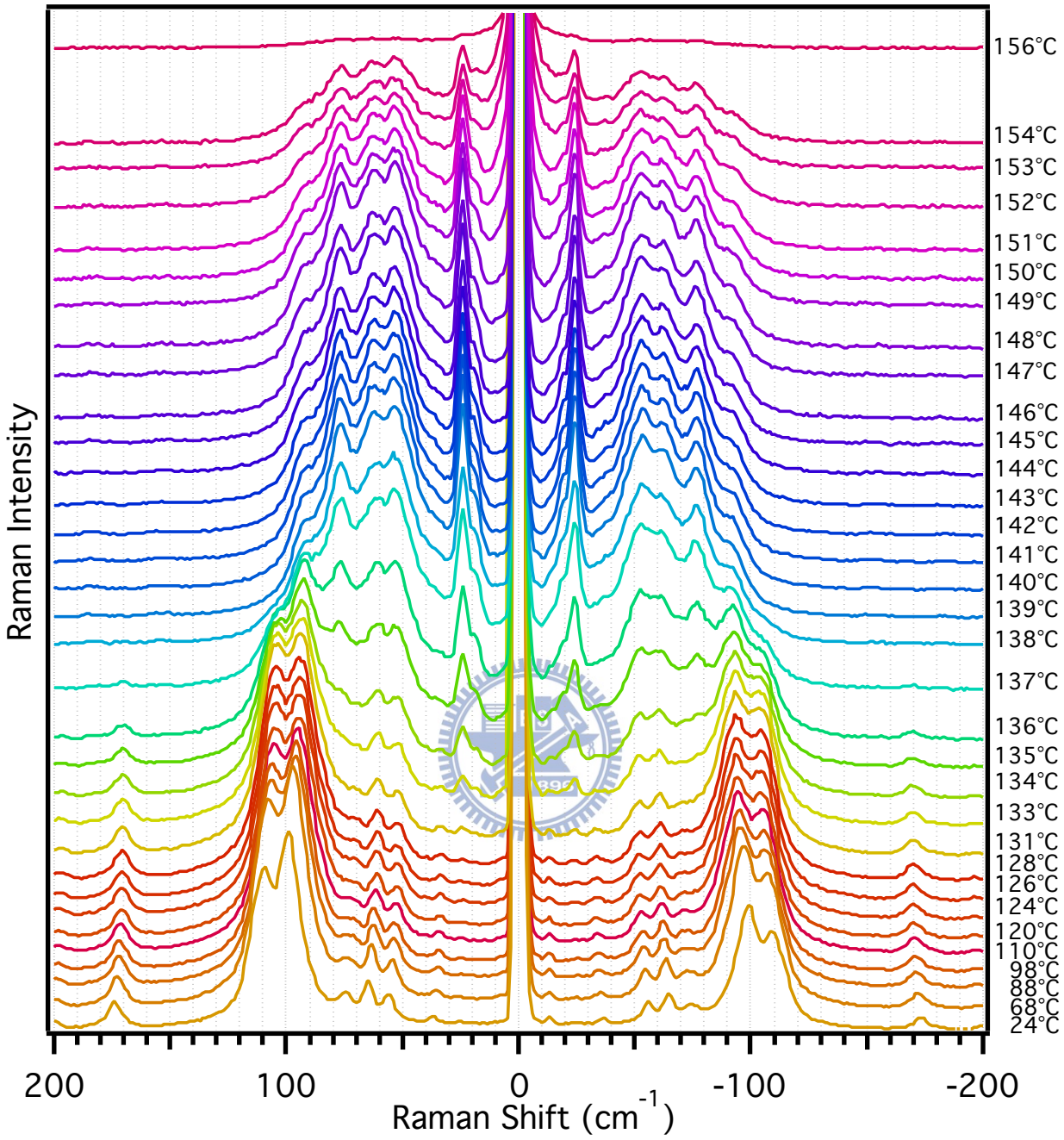

Figure III-11. Low-frequency Raman spectra at different temperatures recorded by heating the cisoid powder. Laser power, 55 mW (514.5 nm excitation); exposure time, 1 s; spectral resolution, 2.7 cm^{-1}; and heating rate, 3 °C/min. The temperatures shown on the right are those indicated by the thermocouple.

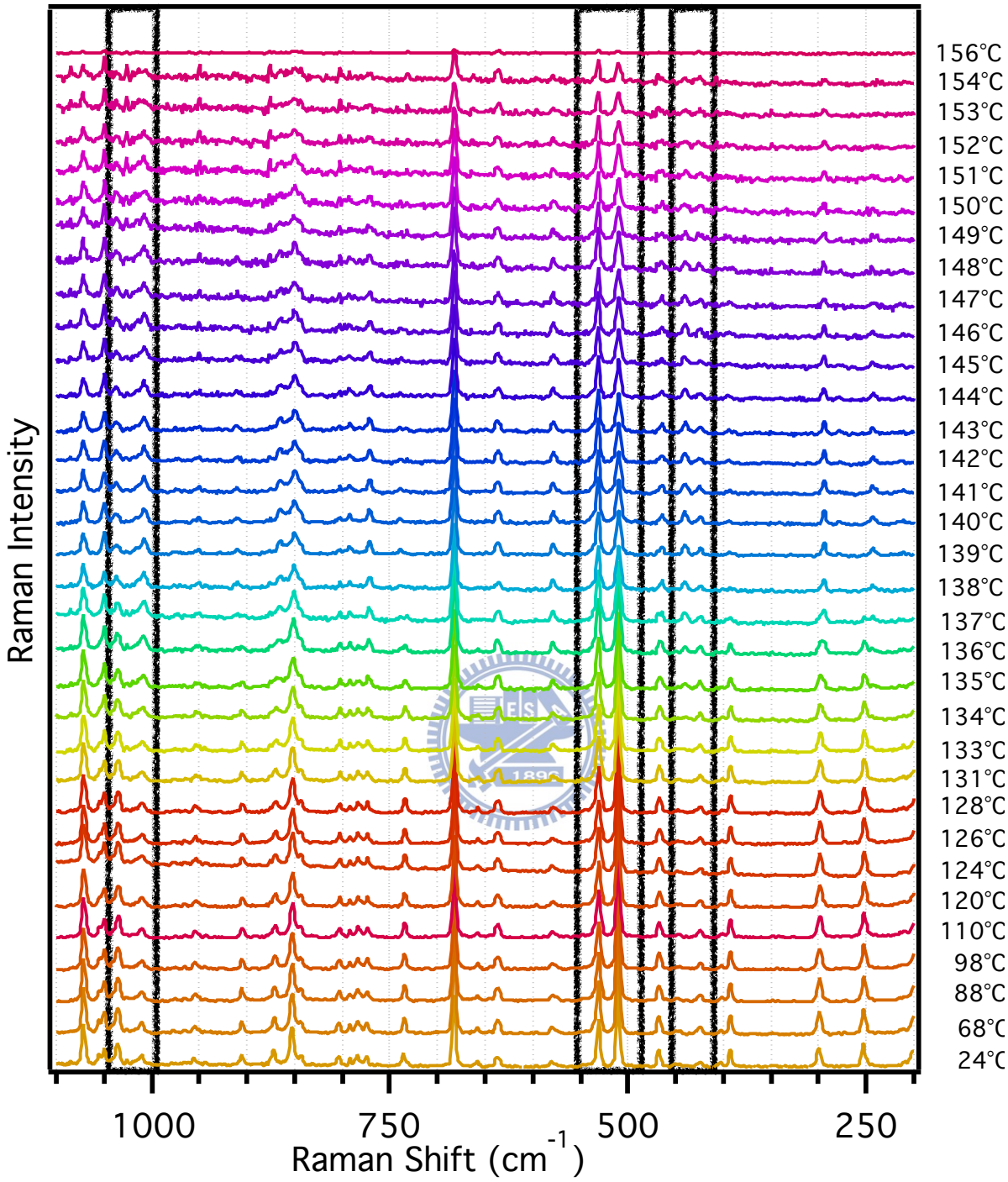

Figure III-12. Raman spectra in the fingerprint region at different temperatures recorded by heating the cisoid powder. Laser power, 55 mW (514.5 nm excitation); exposure time, 1 s; spectral resolution, 2.7 cm^{-1}; and heating rate, 3 °C/min. The temperatures shown on the right are those indicated by the thermocouple.

Raman Spectral Change Observed When the Transoid Powder Is Heated

To examine the reversibility of the transformation between the cisoid and transoid forms, similar heating measurements were performed on the transoid powder. However, we did not observe any transformation of the transoid form. The low-frequency Raman spectra at different temperatures displayed in Figure III-13 show no spectral pattern change. The low-frequency Raman bands just keep showing a decrease in intensity and a slight shift to lower frequency upon heating. After 154 °C, almost all low-frequency Raman bands disappear, indicating the transoid form melts. Also the Raman spectra in the higher frequency region (Figure III-14) do not show any significant change, including the three pairs of Raman bands.

This result suggests that the transformation is irreversible. It only happens with slower heating of the cisoid form. Our result also indicates that the transoid form is a more thermally stable structure. This interpretation is consistent with the X-ray diffraction analysis of the cisoid and transoid single crystals [24]. Figure III-15 depicts the crystal structure inside a unit cell of the cisoid and transoid crystals. In both cases, the intermolecular interactions are mainly from van der Waals force, acting between the H atoms and π electrons of the aromatic ring. In the transoid form, the molecules stack parallel to each other via the CH- π interactions, while the CH- π interactions in the cisoid form are expected to be small within each layer. Thus, the intermolecular interactions within a unit cell of the transoid form are stronger than those in the cisoid form.

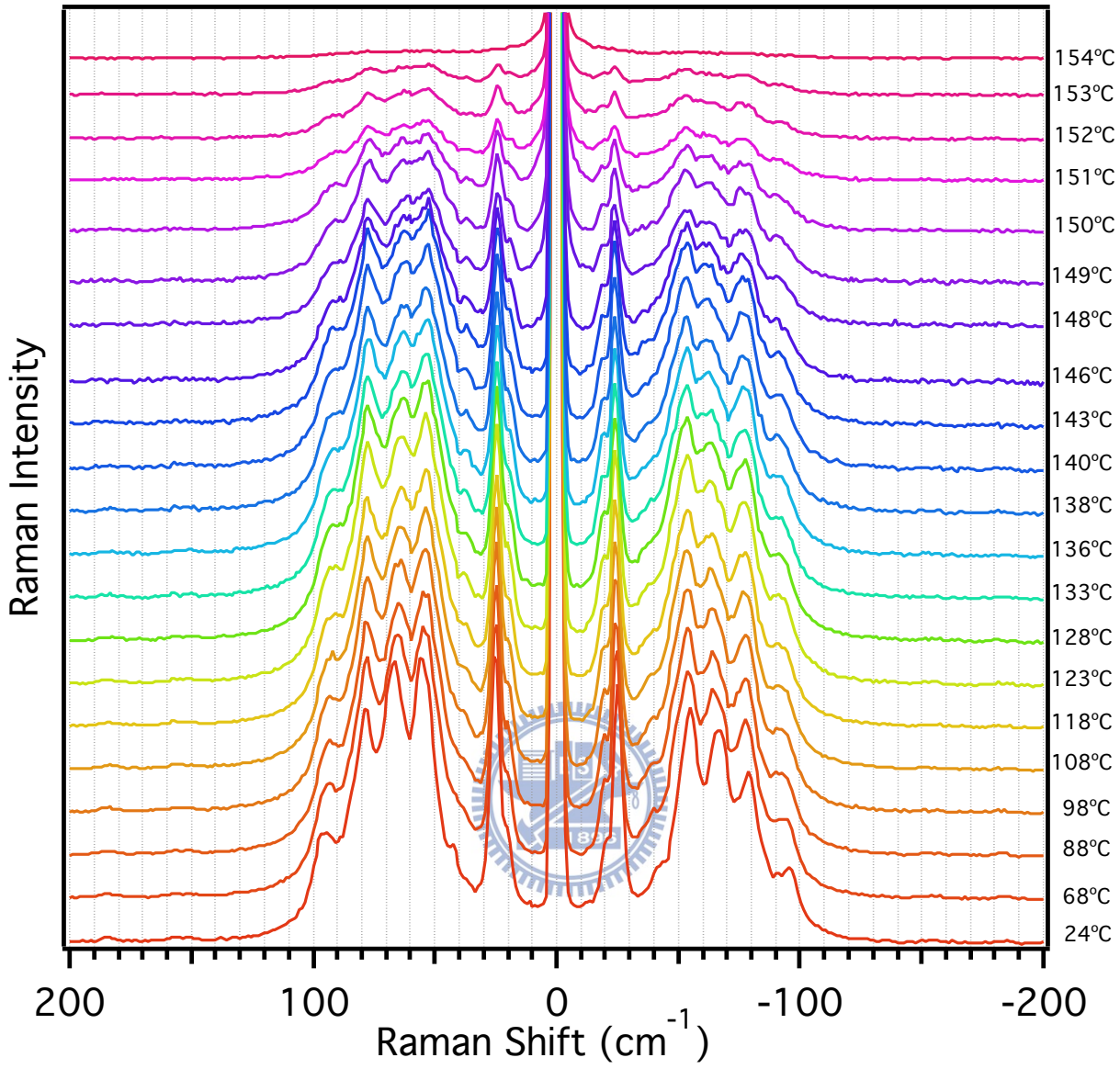

Figure III-13. Low-frequency Raman spectra at different temperatures recorded by heating the transoid powder. Laser power, 55 mW (514.5 nm excitation); exposure time, 1 s; spectral resolution, 2.7 cm^{-1}; and heating rate, 3 °C/min. The temperatures shown on the right are those indicated by the thermocouple.

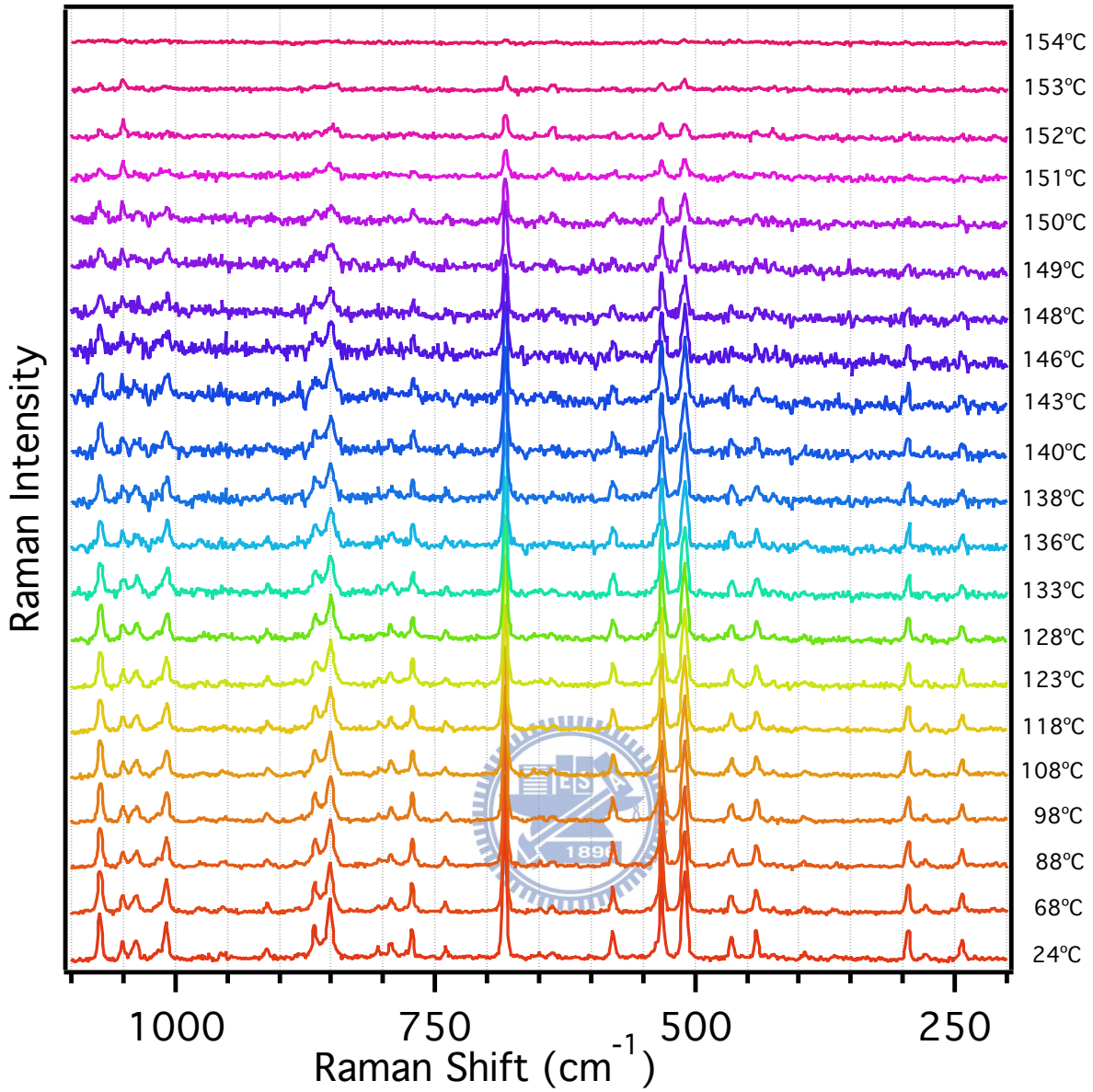

Figure III-14. Raman spectra of the fingerprint region at different temperatures recorded by heating the transoid powder. Laser power, 55 mW (514.5 nm excitation); exposure time, 1 s; spectral resolution, 2.7 cm^{-1}; and heating rate, 3 °C/min. The temperatures shown on the right are those indicated by the thermocouple.

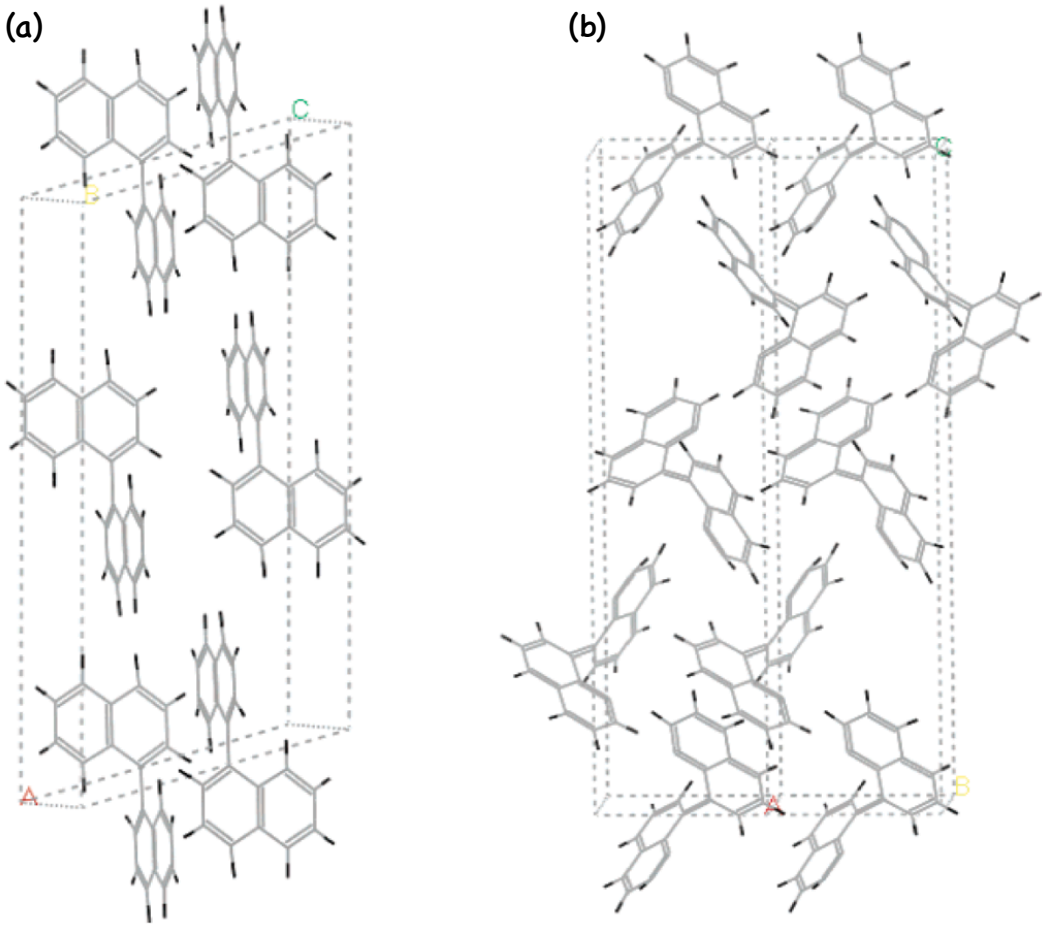

Figure III-15. The crystal structure of (a) the cisoid form and (b) the transoid form. [24]

Raman Spectra of Melted 1,1′-Binaphthyl

We kept recording the Raman spectra after the melting point of the transoid form (158 °C) was reached. The observed Raman spectra after melting are shown in Figure III-16 (a). To get rid of the broad Rayleigh wing, the following reduce equation (Equation III-1) was employed [28].

$$I_{red}[\tilde{v}] = \left(1 + e^{-\frac{hc\tilde{v}}{k_B T}}\right)^{-1} \times (\tilde{v}_0 - \tilde{v})^{-3} \times I_{obs}[\tilde{v}] \qquad \textbf{(III-1)}$$

where c is the speed of light, h is Planck's constant, k_B is the Boltzmann constant, T is the sample temperature, $\tilde{v}_0$ is the absolute wavenumber of the incident laser, $\tilde{v}$ is the Raman shift, and $I_{obs}[\tilde{v}]$ is the observed Raman intensity.

The reduced Raman spectra at different temperatures (Figure III-16 (b)) clearly show that the 20 and 26 cm^{-1} bands of the transoid form disappear upon melting. The absence of these bands in the liquid state suggests that they are most likely assigned to lattice vibrations. In contrast, a broad feature from 40 to 140 cm^{-1} still remains even at 173 °C, which is much higher than the melting point. Based on this observation, the three low-frequency Raman bands at 55, 66, and 79 cm^{-1} may be due to intramolecular vibrations. With the present data alone, it is hard to tell whether the other two shoulders located at 43 and 95 cm^{-1} are lattice vibrations or intramolecular vibrations. Accurate calculations of Raman spectra of molecular crystals, which are highly challenging at the present stage of theoretical development, will help clarify the band assignments.

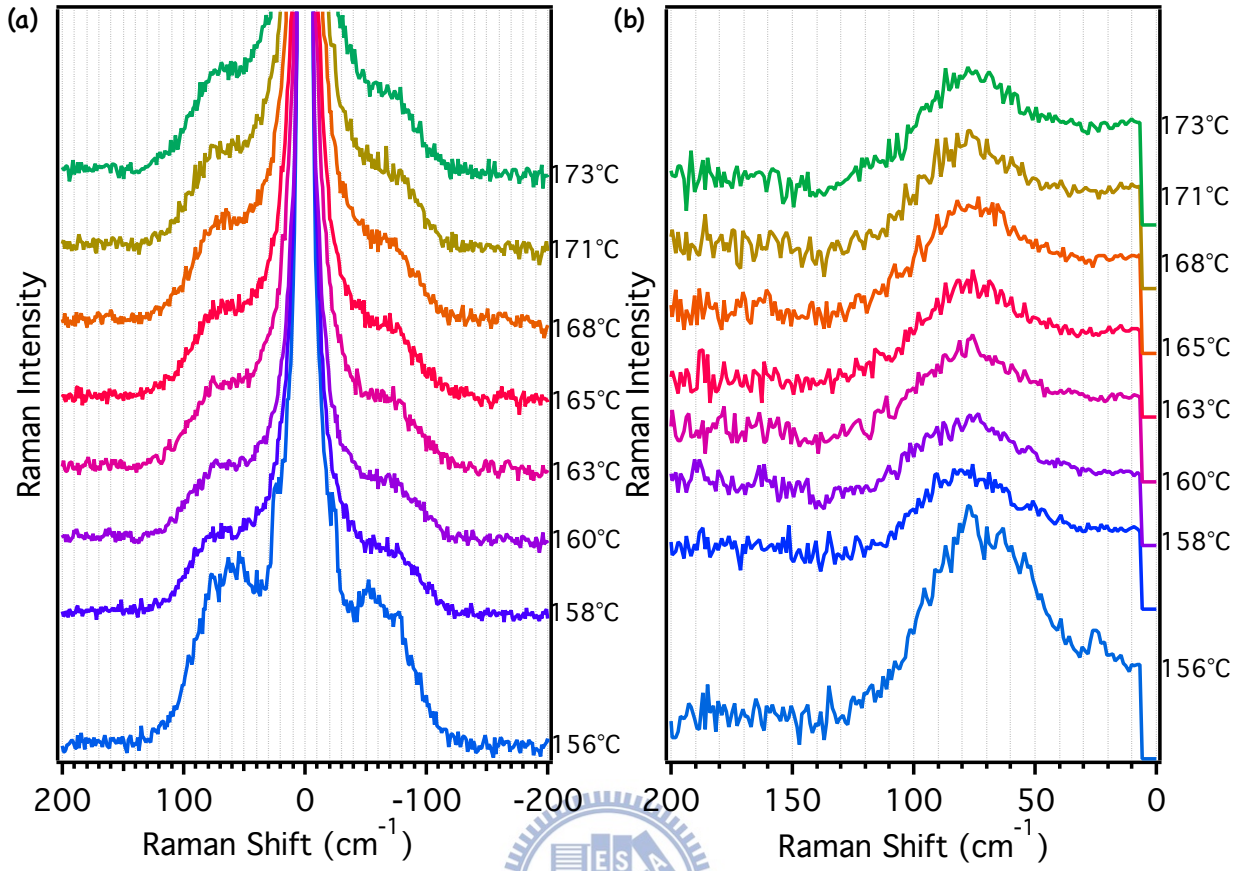

Figure III-16. (a) Observed low-frequency Raman spectra of melted 1,1′-binaphthyl and (b) the corresponding reduced Raman spectra at different temperatures.

Laser power, 55 mW (514.5 nm excitation); exposure time, 1 s; spectral resolution, 2.7 cm^{-1}; and heating rate, 3 °C/min. The temperatures shown on the right are those indicated by the thermocouple.

III-5. Fitting Analysis

We have evidently observed spectral pattern changes associated with the transformation from the cisoid form into the transoid form. To extract quantitative information on peak shift and intensity change, band fitting analysis was applied. In this section, we mainly focus on the spectral change at different temperatures (24–154 °C) in the low-frequency spectra (Figure III-11), and compare with the changes in 510/532 cm^{-1} intensity ratios in the fingerprint region. All Raman spectra were normalized with the strongest intramolecular vibrational band located at 683 cm^{-1} before fitting.

Band Fitting in Low-Frequency Raman Spectra (−200 to +200 cm^{-1})

Raman bands can generally be fitted well by assuming Lorentzian band shape. Here too, Lorentz function was used for fitting each low-frequency band including the shoulder-like peaks in the transoid form. Because the Raman bands at Stokes and anti-Stokes sides must be symmetric with respect to 0 cm^{-1}, the fitting function should have the form

$$\frac{A_i}{(\tilde{\nu} - \tilde{\nu}_i)^2 + {\Delta_i}^2} + \frac{A_i}{(\tilde{\nu} + \tilde{\nu}_i)^2 + {\Delta_i}^2} \qquad \textbf{(III-2)}$$

where $\tilde{\nu}$ is the Raman shift, $\tilde{\nu}_i$ is the peak position, A_i is the band intensity, and Δ_i is the bandwidth. This function has two peak positions at $+\tilde{\nu}_i$ (Stokes side) and $-\tilde{\nu}_i$ (anti-Stokes side). If $\tilde{\nu}_i$ is zero, Equation III-2 reduces to one single Lorentz function located at 0 cm^{-1}, representing Rayleigh scattering.

The intensities of the Stokes and anti-Stokes bands are not the same due to two important factors. First, the anti-Stokes/Stokes intensity ratio is related to the Boltzmann distribution of the vibrational energy levels. Considering that the Stoke and anti-Stokes intensity difference results from the thermal effect, it can be compensated by multiplying the symmetrized Lorentz function (Equation III-1) with the Bose-Einstein factor ($n(\tilde{\nu})$) [29]:

$$n(\tilde{\nu}) = \left(1 + \exp\left[-\frac{ch\tilde{\nu}}{k_B T}\right]\right)^{-1} \quad \textbf{(III-3)}$$

Note that this factor requires only one parameter to be included in the fitting, that is, temperature (T). In the fitting, the temperature parameter is assumed to be common for all the low-frequency Raman bands.

One more factor that affects the anti-Stokes/Stokes intensity ratio is called the "frequency factor", which is due to variation of Raman transition rate of different frequencies. The frequency factor is written as

$$(\tilde{\upsilon}_0 - \tilde{\upsilon})^3 \quad \textbf{(III-4)}$$

where $\tilde{\nu}_0$ is the absolute wavenumber of the incident laser.

The resulting overall fitting function is the product of Equations III-2, III-3 and III-4 as follows:

$$f(\tilde{\upsilon}) = y_0 + \left\{\sum\left[\frac{A_i}{(\tilde{\upsilon} - \tilde{\upsilon}_i)^2 + \Delta_i^2} + \frac{A_i}{(\tilde{\upsilon} + \tilde{\upsilon}_i)^2 + \Delta_i^2}\right]\right\} \times \left(1 + e^{-\frac{hc\tilde{\upsilon}}{k_B T}}\right)^{-1} \times (\tilde{\upsilon}_0 - \tilde{\upsilon})^3 \quad \textbf{(III-5)}$$

Table III-1 summarizes the fitting parameters. This fitting function can fit nine low-frequency bands of the cisoid and transoid form in both Stokes and anti-Stokes sides. Twenty-nine independent parameters are determined simultaneously for each fitting.

Table III-1.	
Baseline	y_0
Peak position	$\tilde{\nu}_i$ $(i = 1–9)$
Bandwidth	Δ_i $(i = 1–9)$
Intensity	A_i $(i = 1–9)$
Temperature	T

Figure III-17 shows the fitted results of the heating measurement on the cisoid form. All Raman spectra are well reproduced by the assumed fitting function (Equation III-5). Based on these high-quality fitting results, the temperature at the sample point can be estimated. Moreover, changes in the peak position change as well as in intensity can also been determined by the fitting. These results will be discussed independently in the next section.

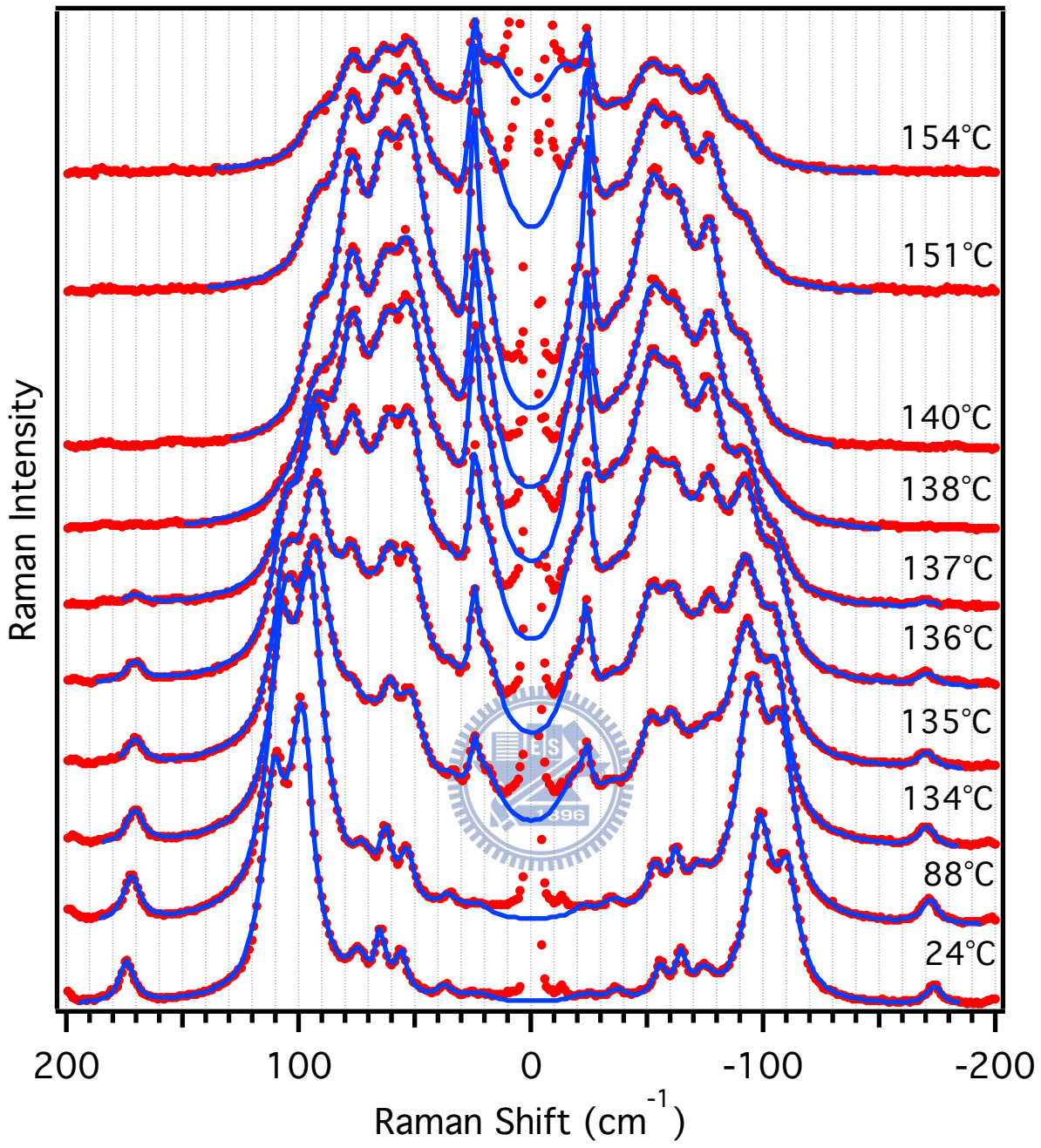

Figure III-17. Experimental data in the low-frequency region (red dots) and their fitted results (blue lines). The temperatures shown on the right are those indicated by the thermocouple.

Band Fitting of a Pair of Raman Bands at 510/532 cm^{-1}

As mentioned in Chapter III-3, the intensity ratios of three pairs of Raman bands at 450/468 cm^{-1}, 510/532 cm^{-1} and 1010/1035 cm^{-1} are found to differ between the cisoid and transoid forms. Among these three pairs, the 510/532 cm^{-1} pair has the strongest intensities, so we analyze this pair. The determined intensity ratios are compared with the intensity change of the low-frequency bands at different temperatures.

Trial fitting shows that neither Gaussian function nor Lorentz function can perfectly fit the pair of Raman bands. Therefore, the Voigt function, whose line shape is in between Gaussian and Lorentzian profiles, was used to fit the pair of Raman bands. Equation III-6 describes the fitting function.

$$f(\tilde{v}) = y_0 + \sum I_i \times Voigt[(\tilde{v} - \tilde{v}_i) \times \Delta_i, B_i] \quad \textbf{(III-6)}$$

where y_0 determines the baseline, I_i is the band intensity, $\tilde{v}$ is the Raman shift, $\tilde{v}_i$ is the peak position, and Δ_i is the bandwidth. B_i is used to adjust the band shape.

Some representative fitting results are shown in Figure III-18, from which the intensity ratios can be easily calculated.

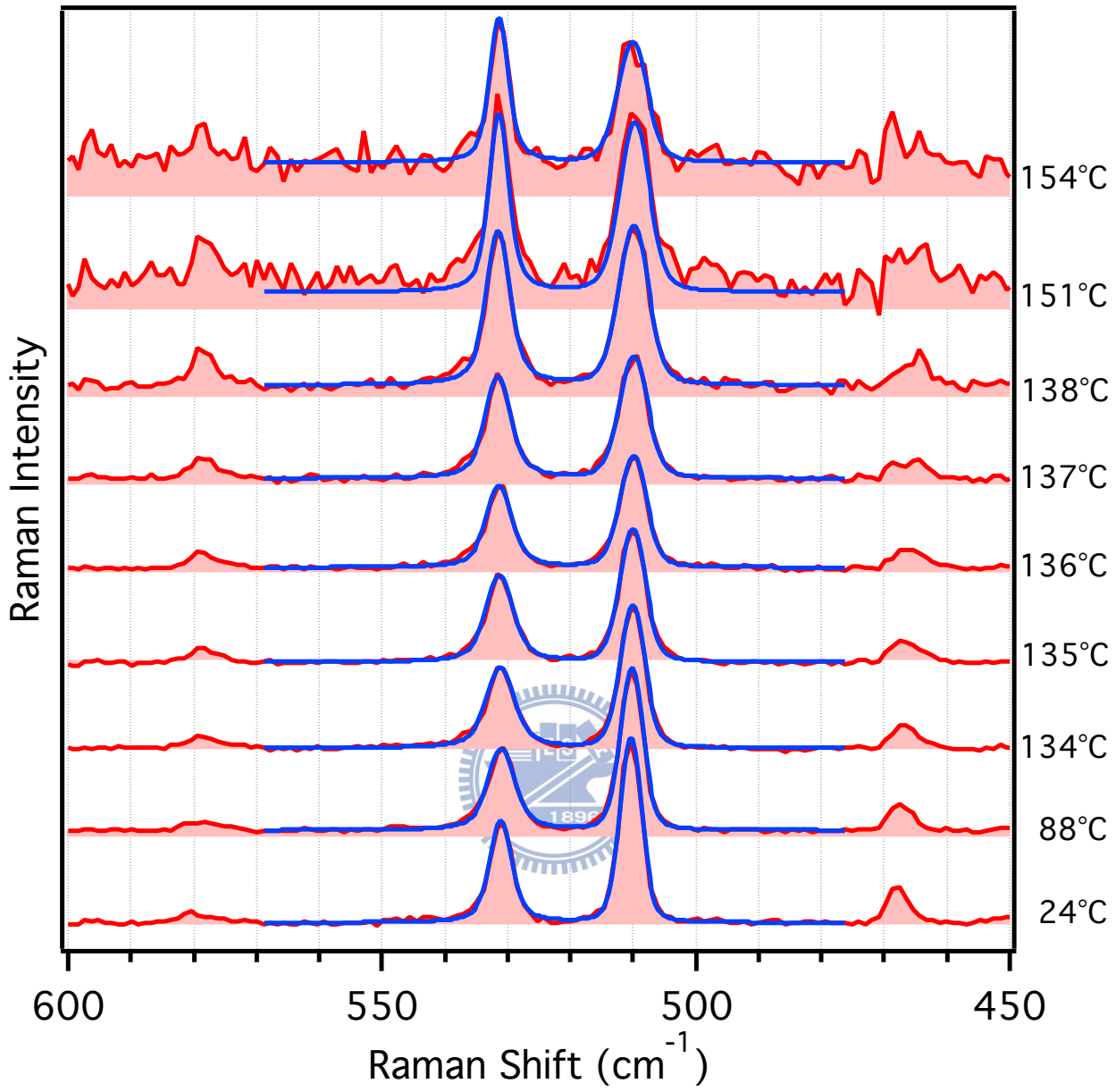

Figure III-18. Experimental data in the fingerprint region (red hatched curves) and their fitted results (blue curves). The temperatures shown on the right are those indicated by the thermocouple.

III-6. Discussion:

Changes in Low-frequency Raman Bands Change During Transformation

Peak Position Shift Caused by Temperature Elevation

Figure III-19 displays the changes in peak positions of the low-frequency bands obtained from band fitting. Because the measurement started from the cisoid form and the cisoid form transformed into the transoid form at high temperatures, the temperature ranges in Figures III-19 (a) and (b) are different from each other. All the bands shift to lower frequency linearly when increasing temperature. It is noteworthy that the cisoid associated bands have more prominent peak shifts (larger slopes) than those of the transoid associated bands. It is known that the peak shift is related to thermal expansion of the crystal structure. Consequently, the smaller peak shift of the Raman bands found for the transoid form may imply stronger intermolecular interaction than the cisoid form. This result also supports the argument that the transoid form has a more stable crystal structure.

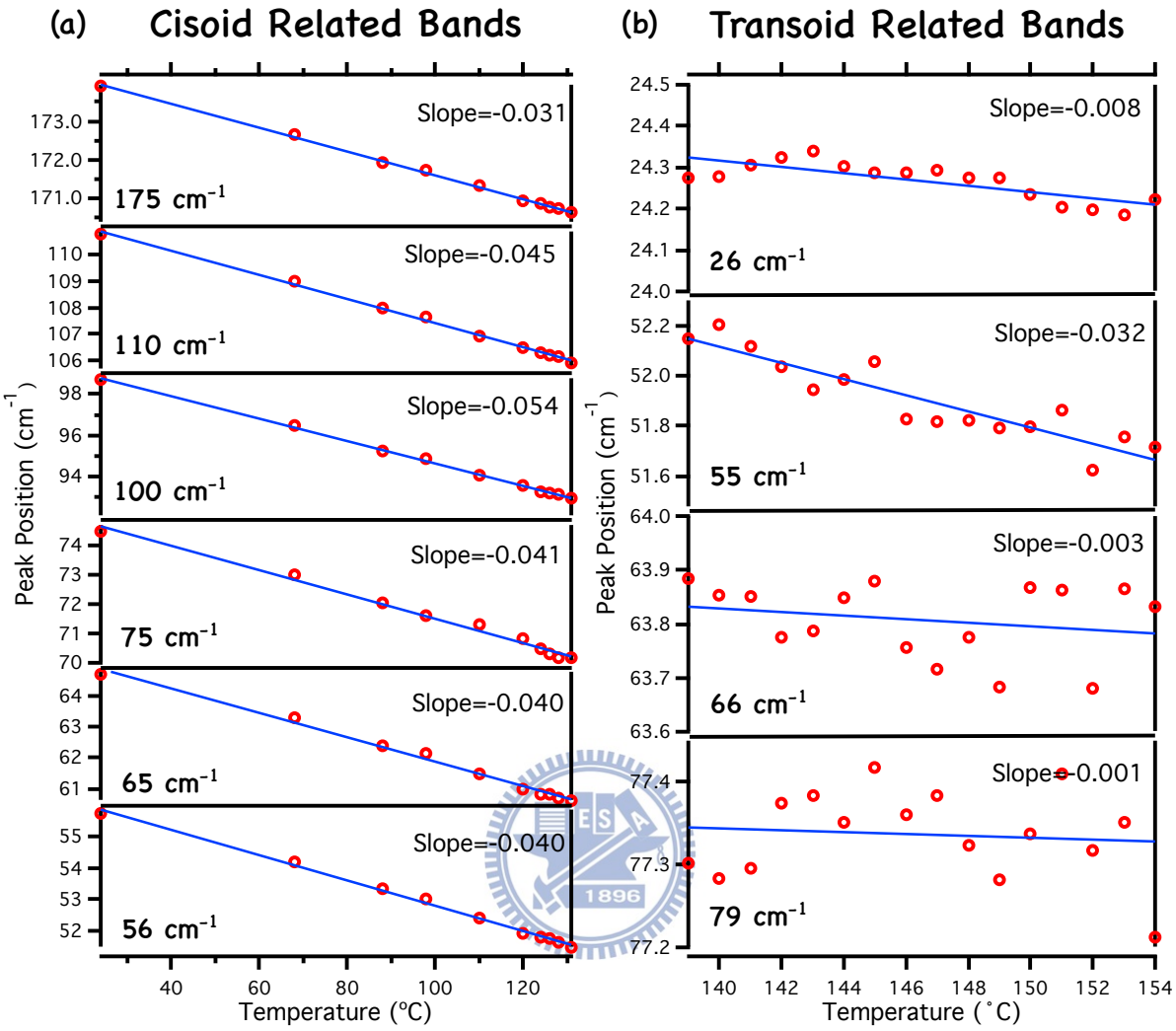

Figure III-19. Peak position shift with respect to temperature of (a) the cisoid related bands and (b) the transoid related bands. Opened circles are the peak positions at different temperatures and solid lines are line fitting of the peak positions. The temperature on the horizontal axis refers to that indicated by the thermocouple.

Band Intensity Change During the Transformation

The cisoid and the transoid forms have some distinct Raman bands in the low-frequency region, such as 175, 110, and 100 cm^{-1} for the cisoid form and 26 cm^{-1} for the transoid form. By tracing the change of these band intensities, we can understand the transformation progress. Figure III-20 exhibits the band intensity change during the transformation until melting takes place. At 128 °C, the 26 cm^{-1} band of the transoid form appears, indicating the onset of transformation. At temperatures higher than 128 °C, the intensities of the transoid Raman bands keep increasing, whereas the cisoid Raman bands keep decreasing. At temperatures higher than 138 °C, all the cisoid form related bands disappears, indicating that the cisoid form has been transformed into the transoid form completely. It is worth noting that the most intense cisoid Raman band at 100 cm^{-1} becomes as a shoulder band of the transoid form at 95 cm^{-1}, so it still possesses some intensity even after the transformation.

The change of the 510/532 cm^{-1} intensity ratio is also compared with the intensity change of the low-frequency bands in Figure III-20. At room temperature, the cisoid form has a larger 510/532 cm^{-1} intensity ratio (~2) than the transoid form (~1). Upon the transformation, due to the appearance of the transoid form, the 510/532 cm^{-1} intensity ratio decreases. It is noteworthy that the intensities of an intramolecular vibration band at 300 cm^{-1} maintained almost unity for all temperatures, indicating normalization of the spectra by the 683 cm^{-1} band worked well.

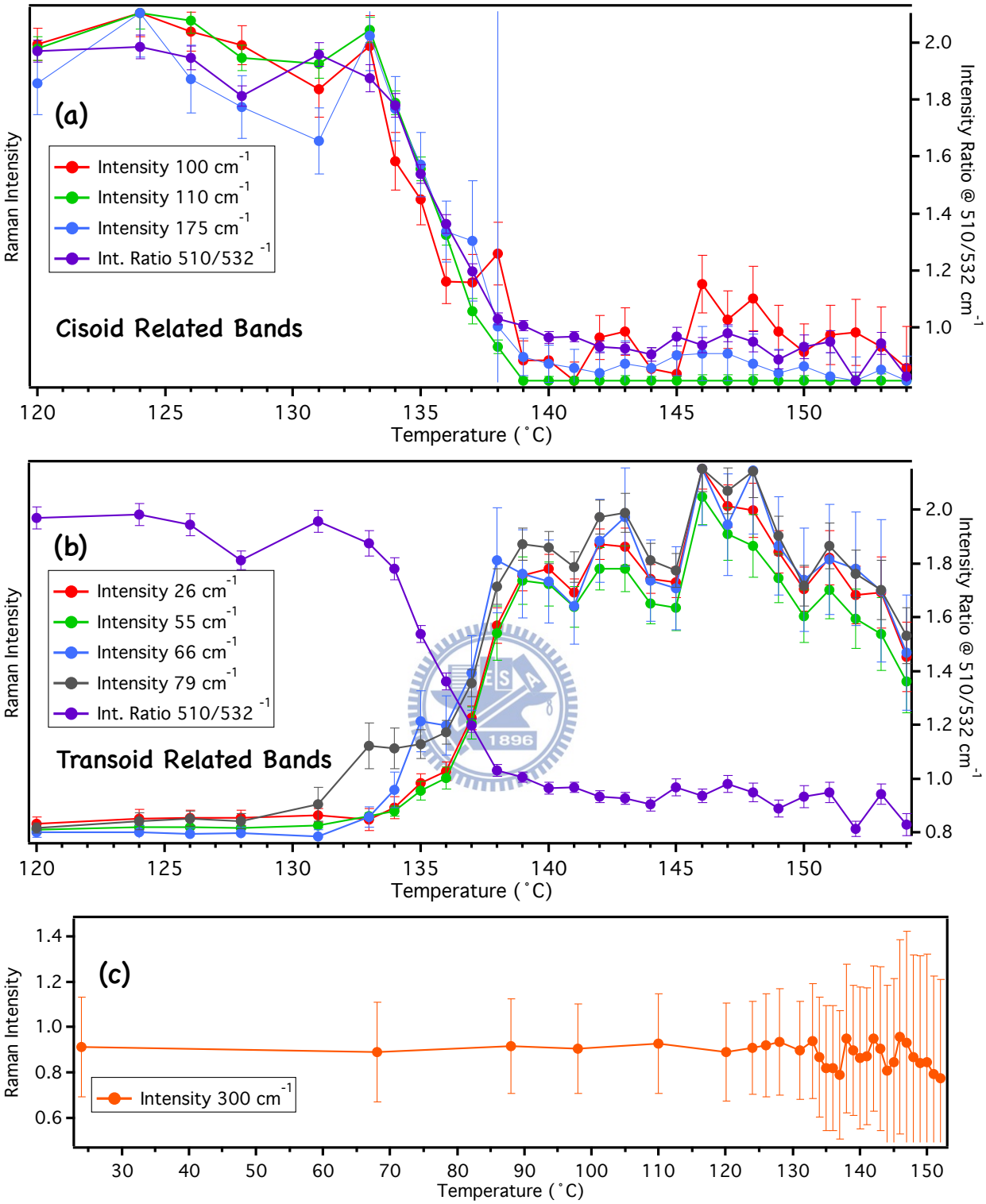

Figure III-20. Low-frequency band intensity changes upon heating of (a) the cisoid related bands, (b) the transoid related bands. Also shown is the change of the 510/532 cm^{-1} intensity ratio (purple lines) upon heating and (c) intramolecular vibration band at 300 cm^{-1}.

III-7. Discussion:

Which Low-Frequency Band Is Attributed to the Torsional Motion?

Low-frequency Raman spectroscopy is sensitive to some intramolecular vibrations, which have large amplitude, such as the C–C torsional motion of the crystalline biphenyl [30]. Since 1,1′-binaphthyl is a similar biaryl compound, we expect to observe the C–C torsional motion in crystalline 1,1′-binaphthyl as well. In Wang's Master thesis, he regarded the 26 cm^{-1} as the most likely candidate for the torsional motion on the basis of DFT calculation results [26]. However, according to the melted 1,1′-binaphthyl spectra (Figure III-21 (a)), the 26 cm^{-1} band is assigned to a lattice vibration rather than to the torsional motion. In contrast, a broad band ranging from 40 to 140 cm^{-1} with the peak located at 75 cm^{-1} remains even after melting. Thus, we attribute the three bands at 56, 65, and 75 cm^{-1} for the cisoid form (Figure III-21 (b)) and 55, 66, and 79 cm^{-1} for the transoid form to the torsional motion. The transoid form, which has a larger dihedral angle (103.1°) than the cisoid form (68.6°), would have a smaller barrier for the torsional motion due to smaller repulsion force between the two H atoms at 8 and 8′ positions. The smaller barrier for the torsional motion may result in a larger change of polarizability, so the transoid form shows stronger Raman intensity of the torsional motion than the cisoid form.

The Raman spectrum of 1,1′-binaphthyl in carbon tetrachloride was also measured to confirm the intramolecular vibrations in the low-frequency region and is shown in Figure III-21 (d). Solvent bands have been subtracted and subsequently, the difference spectrum was reduced

by using Equation III-1. The spectrum displays a similar pattern to the melted 1,1′-binaphthyl spectrum. Both of them show a broad band centered at 75 cm^{-1}. This result further supports that the composite band around 75 cm^{-1} arises from the torsional motion along the C-C single bond.

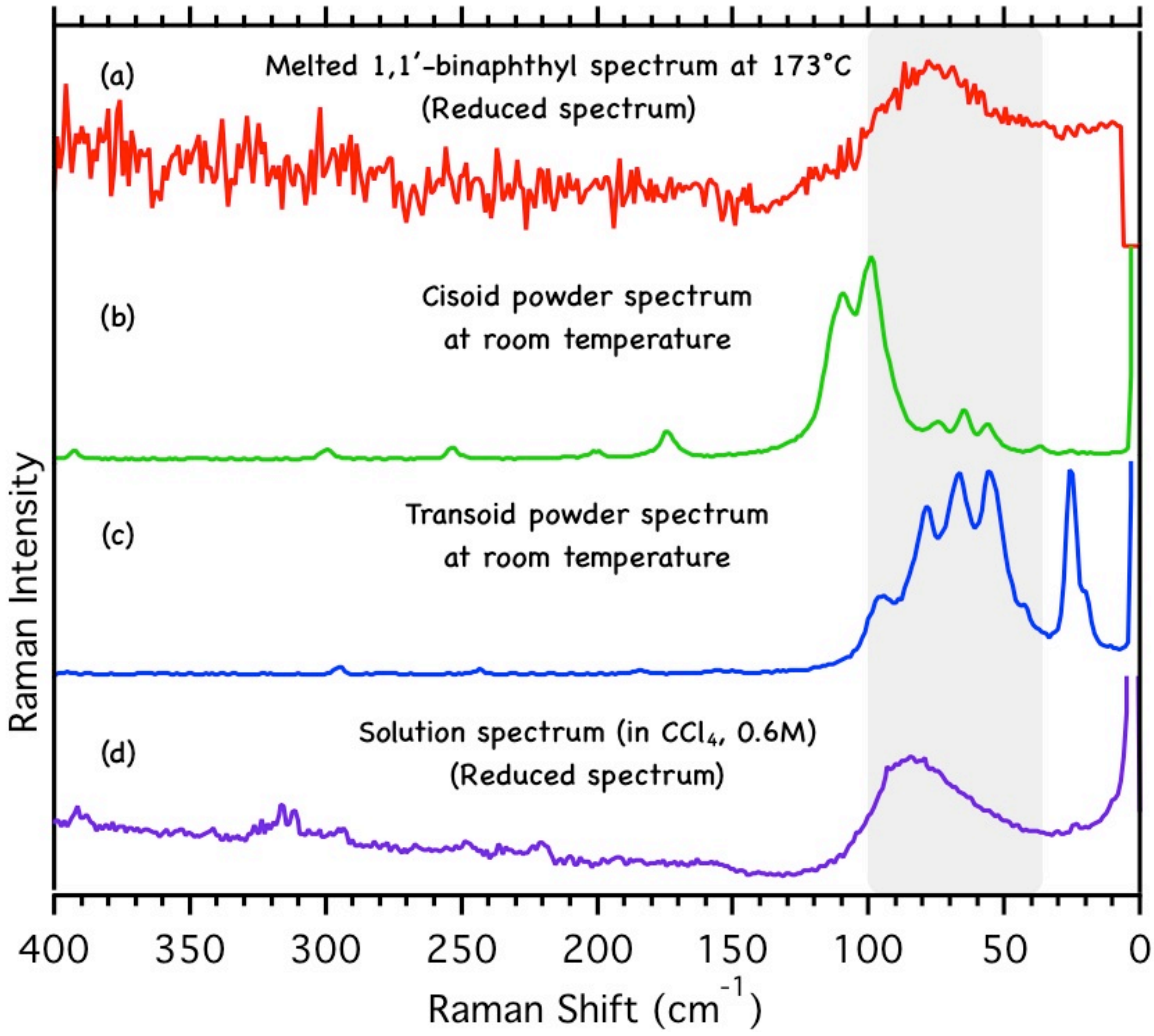

Figure III-21. (a) Reduced spectrum of the melted 1,1′-binaphthyl. (b) Raman spectrum of the cisoid form. (c) Raman spectrum of the transoid form. (d) Raman spectrum of 1,1′-binaphthyl dissolved in CCl_4 (0.6 M) at room temperature.

The solution spectrum was measured with 532 nm excitation and 50 mW power. The exposure time was 3 min. The spectral resolution was 2.7 cm^{-1}.

III-8. Summary

In this chapter, we have demonstrated that low-frequency Raman spectroscopy can effectively discriminate molecules that have the same chemical formula but different crystal structures. The cisoid form and the transoid form of 1,1′-binaphthyl show distinct low-frequency spectral patterns. This is the first observation of the low-frequency (<150 cm^{-1}) Raman spectra of 1,1′-binaphthyl. The 100 and 110 cm^{-1} bands can be used as the marker bands for the cisoid form, while the 20 and 26 cm^{-1} bands for the transoid form.

In the slow heating experiments, we found that the cisoid form gradually transforms into the transoid form from 128 °C. At temperatures higher than 138 °C, it totally transforms into the transoid form. On the other hand, the transoid form cannot transform back into the cisoid form while heating. By analyzing the temperature dependent change of peak position, the transoid form shows less peak shift than the cisoid form, indicating that the transoid form undergoes less thermal expansion of the crystal structure. These results imply that the transoid form has a more stable structure than the cisoid form.

In the Raman spectra of melted 1,1′-binaphthyl and of 1,1′-binaphthyl in solution, almost all low-frequency Raman bands are absent. Only a broad band centered at 75 cm^{-1} remains because it possibly comes from an intramolecular vibration. Thus, we conclude that the 56, 65, and 75 cm^{-1} bands of the cisoid form, and the 55, 66, and 79 cm^{-1} bands of the transoid form are associated with this broad band, which is most probably assigned to the torsional motion.

References for Chapter III.

[1]. R. Noyori and H. Takaya, "BINAP: an efficient chiral element for asymmetric catalysis," *Accounts of Chemical Research,* vol. 23, pp. 345-350, 1990.

[2]. D. J. Cram, R. C. Helgeson, K. Koga, E. P. Kyba, K. Madan, L. R. Sousa, M. G. Siegel, P. Moreau, and G. W. Gokel, "Host-guest complexation. 9. Macrocyclic polyethers and sulfides shaped by one rigid dinaphthyl unit and attached arms. Synthesis and survey of complexing abilities," *The Journal of Organic Chemistry,* vol. 43, pp. 2758-2772, 1978.

[3]. A. Miyashita, A. Yasuda, H. Takaya, K. Toriumi, T. Ito, T. Souchi, and R. Noyori, "Synthesis of 2,2'-bis(diphenylphosphino)-1,1'-binaphthyl (BINAP), an atropisomeric chiral bis(triaryl)phosphine, and its use in the rhodium(I)-catalyzed asymmetric hydrogenation of .alpha.-(acylamino)acrylic acids," *Journal of the American Chemical Society,* vol. 102, pp. 7932-7934, 1980.

[4]. A. S. Cooke and M. M. Harris, "Ground-state strain and other factors influencing optical stability in the 1,1'-binaphthyl series," *Journal of the Chemical Society (Resumed),* pp. 2365-2373, 1963.

[5]. A. Almenningen, O. Bastiansen, L. Fernholt, B. N. Cyvin, S. J. Cyvin, and S. Samdal, "Structure and barrier of internal rotation of biphenyl derivatives in the gaseous state : Part 1. The molecular structure and normal coordinate analysis of normal biphenyl and pedeuterated biphenyl," *Journal of Molecular Structure,* vol. 128, pp. 59-76, 1985.

[6]. Richard E. Pincock, Robert R. Perkins, Alan S. Ma, and K. R. Wilson, "Probability Distribution of Enantiomorphous Forms in Spontaneous Generation of Optically Active Substances," *Science,* vol. 174, pp. 1018-1020, 1971.

[7]. Y. Badar, C. C. K. Ling, A. S. Cooke, and M. M. Harris, "Two Crystalline Modifcations of 1,1'-Binaphthyl," *Journal of the Chemical Society,* pp. 1543-1544, 1965.

[8]. W. A. C. Brown, J. Trottera, and J. M. Robertson, "X-Ray Study of Crystals isolated during the Synthesis of 1,12-o-Phenyleneperylene," *Proceedings of the Chemical Society,* pp. 115-116, 1961.

[9]. K. A. Kerr and J. M. Robertson, "Crystal and Molecular Structure of 1,1'-Binaphthyl," *Journal of the Chemical Society B,* pp. 1146-1149, 1969.

[10]. R. B. Kress, E. N. Duesler, M. C. Etter, I. C. Paul, and D. Y. Curtin, "Solid-state Resolution of Binaphthyl: Crystal and Molecular Structures of the Chiral (A)[1] Form and Racemic (B)[1] Form and the Study of the Rearrangement of Single Crystals. Requirements for Development of Hemihedral Faces for Enantiomer Identification," *Journal of the American Chemical Society,* vol. 102, pp. 7709-7714, 1980.

[11]. C. V. Shank, E. P. Ippen, O. Teschke, and K. B. Eisenthal, "Picosecond dynamics of conformational changes in 1,1'-binaphthyl," *The Journal of Chemical Physics,* vol. 67, pp. 5547-5551, 1977.

[12]. R. A. Friedel, M. Orchin, and L. Reggel, "Steric Hindrance and Short Wave Length Bands in the Ultraviolet Spectra of Some Naphthalene and Diphenyl Derivatives," *Journal of the American Chemical Society,* vol. 70, pp. 199-204, 1948.

[13]. R. M. Hochstrasser, "The Effect of Intramolecular Twisting on The Emission Spectra of Hindered Aromatic Molecules: Part I. 1,1'-Binaphthyl," *Canadian Journal of Chemistry,* vol. 39, pp. 459-470, 1961.

[14]. M. J. Riley, A. R. Lacey, M. G. Sceats, and R. G. Gilbert, "Low-temperature vibronic spectra of 1,1'-binaphthyl," *Journal of Chemical Physics,* vol. 72, pp. 83-91, 1982.

[15]. A. R. Lacey and F. J. Craven, "A preliminary study of the conformation of 1,1'-binaphthyl in solution by Raman spectroscopy," *Chemical Physics Letters,* vol. 126, pp. 589-592, 1986.

[16]. S. Fujiyoshi, S. Takeuchi, and T. Tahara, "Time-Resolved Impulsive Stimulated Raman Studies of 1,1'-Binaphthyl in the Excited State: Low-Frequency Vibrations and Conformational Relaxation," *The Journal of Physical Chemistry A,* vol. 108, pp. 5938-5943, 2004.

[17]. V. Liégeois, "A Vibrational Raman Optical Activity Study of 1,1'-Binaphthyl Derivatives," *ChemPhysChem,* vol. 10, pp. 2017-2025, 2009.

[18]. F. Zhang, G. B. Bacskay, and S. H. Kable, "Quantum Chemical Determination of the Equilibrium Geometries and Harmonic Vibrational Frequencies of 1,1‘-, 1,2‘- and 2,2'-Binaphthyl in Their Ground and Excited (1La) Electronic States," *The Journal of Physical Chemistry A,* vol. 108, pp. 172-184, 2003.

[19]. K. Gustav, J. Sühnel, and U. P. Wild, "Theoretical study on geometry and spectroscopic properties of 1,1'-binaphthyl in the electronic ground and first excited singlet states," *Chemical Physics,* vol. 31, pp. 59-65, 1978.

[20]. R. W. Bigelow and R. W. Anderson, "A CNDO/S study on the electronic structure of

1,1'-binaphthyl," *Chemical Physics Letters,* vol. 58, pp. 114-118, 1978.

[21]. M. F. M. Post, J. K. Eweg, J. Langelaar, J. D. W. van Voorst, and G. Ter Maten, "SCF Cl calculations and assignment of the S1 --> Sn absorption spectra of 1,1'-binaphthyl in different molecular conformations," *Chemical Physics,* vol. 14, pp. 165-176, 1976.

[22]. R. E. Carter and T. Liljefors, "A theoretical study of configurational inversion of 1,1'-binaphthyl by molecular mechanics," *Tetrahedron,* vol. 32, pp. 2915-2922, 1976.

[23]. A. Gamba, E. Rusconi, and M. Simonetta, "A conformational study of phenyl- and naphthyl-naphthalenes," *Tetrahedron,* vol. 26, pp. 871-877, 1970.

[24]. C. I. Sainz-Díaz, A. P. Martín-Islán, and J. H. E. Cartwright, "Chiral Symmetry Breaking and Polymorphism in 1,1'-Binaphthyl Melt Crystallization," *The Journal of Physical Chemistry B,* vol. 109, pp. 18758-18764, 2005.

[25]. D. K. Kondepudi, J. Laudadio, and K. Asakura, "Chiral Symmetry Breaking in Stirred Crystallization of 1,1'-Binaphthyl Melt," *Journal of the American Chemical Society,* vol. 121, pp. 1448-1451, 1999.

[26]. Szu-Cheng Wang, "Construction of a Fast Low-Frequency Raman Spectrometer and Its Application to Real-Time Tracing of Melting Process of Crystalline 1,1'-binaphthyl," *National Chiao Tung University*, Master Thesis, 2011.

[27]. Harry T. Jonkman and Douwe A. Wiersma, "Spectroscopic study of conformational dynamics of 1,1′binaphthyl in a jet," *Journal of Chemical Physics*, vol. 81, pp. 1573-1582, 1984.

[28]. K. Iwata, H. Okajima, S. Saha, and H. Hamaguchi, "Local Structure Formation in Alkyl-imidazolium-Based Ionic Liquids as Revealed by Linear and Nonlinear Raman Spectroscopy," *Accounts of Chemical Research*, vol. 40, pp. 1174-1181, 2007.

[29]. R. Shuker and R. W. Gammon, "Raman-Scattering Selection-Rule Breaking and the Density of States in Amorphous Materials," *Physical Review Letters,* vol. 25, pp. 222-225, 1970.

[30]. H. Takeuchi, S. Suzuku, A. J. Dianoux, and G. Allen, "Low frequency vibrations in crystalline biphenyl: Model calculations and Raman and neutron spectra," *Chemical Physics,* vol. 55, pp. 153-162, 1981.

Chapter IV.

Low-Frequency Raman Imaging of 1,1′-Binaphthyl Crystals

IV-1. Purpose of This Study

In Chapter III, we studied the transformation dynamics of polycrystalline powder 1,1′-binaphthyl samples macroscopically. Here, we are interested in investigating 1,1′-binaphthyl crystals microscopically, that is, under an optical microscope. The confocal microspectroscopy described in section II-3 is applied to the cisoid and transoid crystals of 1,1′-binaphthyl in this study.

Confocal Raman microspectroscopy has been widely used in bioscience. Our group has been applying this technique to perform *in-vivo* Raman imaging of living cells and investigate the distributions of proteins, lipids and polysaccharide inside the cell [1, 2]. Also, there are some studies on crystal growth based on high-frequency Raman signals [3-5]. However, high-frequency Raman signals are relatively weak compared with low-frequency signals. Since the laboratory-built confocal Raman system can easily observe Raman signals down to 9.8 cm^{-1}, we make full use of the information derived from low-frequency Raman spectra to investiate crystal structures and molecular orientations.

IV-2. Sample Preparation

The ciosid form single crystal was recrystallized by the gas diffusion method (Figure IV-1 (a)). Pure 1,1′-binaphthyl powder in a small vial was dissolved in ethyl acetate, then it was put in a larger vial containing n-pentane. Because n-pentane has a lower boiling point than ethyl acetate, it would diffuse into the small vial and slowly decrease the solubility of 1,1′-binaphthyl in ethyl acetate, eventually resulting in recrystallization of 1,1′-binaphthyl. The cisoid form single crystals can be found in the bottom of the small vial after one day. A typical cisoid single crystal obtained with this protocol is shown in Figure IV-1 (b). Note that the cisoid crystal belongs to monoclinic (*C*2/c) space group [6].

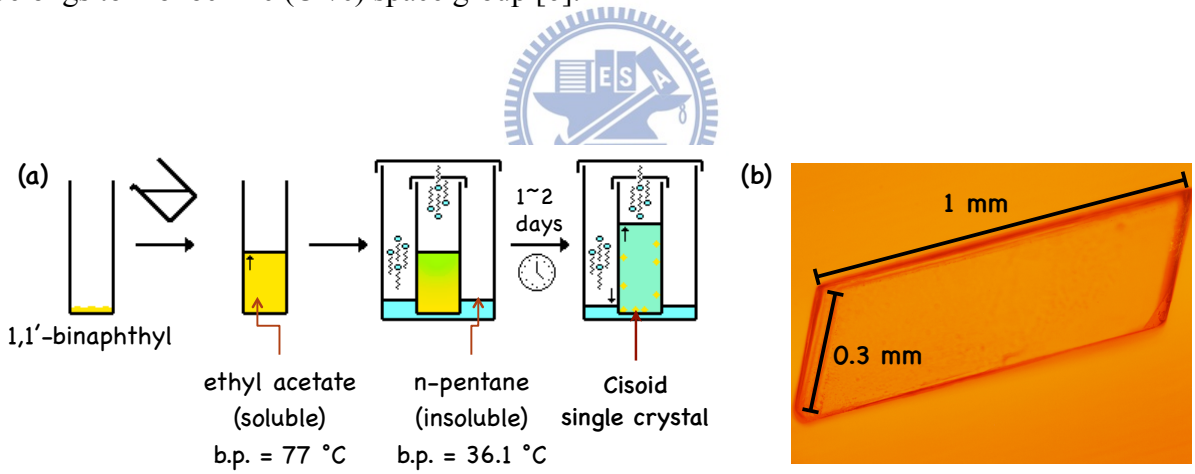

Figure IV-1. (a) Preparation of the cisoid form single crystal. [Picture from Wikipedia].

(b) Bright-field optical image of a typical cisoid form single crystal obtained with the gas diffusion method.

Then the cisoid form single crystal was transfered from the vial to a slide glass by a sharp needle made from a glass capillary. The glass needle is an insulator which is easily coverd by

static electricity on the surface. Therefore, we can use the interaction between static electricity on the sharp needle and van der Waals force of the cisoid molecules to transfer the tiny sample without damaging. The cisoid form single crystal was sandwiched by slide glass, sealed by high temperature tape and kept at 130 °C on a hot plate for three days. After cooling down to room temperature, the transoid crystals were observed under the optical microscope. Some transoid crystals were isolated from the cisoid mother crystal, but some were attached to the ciosid mother crystal. This observation supports that the transformation mechanism is sublimation of the cisoid form followed by recrystalization to the transoid form [6, 7]. To demonstrate the power of low-frequency Raman microspectroscopy, we focus especially on the sample in which a transoid crystal is found in the vicinity of a cisoid crystal (Figure IV-2).

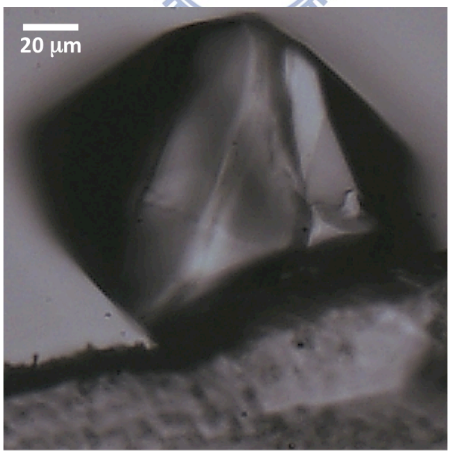

Figure IV-2. Bright-field optical image of a composite of the cisoid and transoid microcrystals.

IV-3. Low-Frequency Raman Imaging of the Cisoid Form Crystal

The prepared cisoid form single crystal (Figure IV-3 (a)) was analyzed by multi-mode Raman images constructed from the low-frequency Raman bands to check the molecular alignment inside the crystal. Space-resolved Raman spectra were recorded by moving with a 3 μm step the sample mounted on the motarized stage. Each Raman spectrum was taken with 0.2 second exposure under the conditions of 532 nm excitation, 5 mW laser power and 2.7 cm^{-1} spectral resolution. Ultimately, an area of 600 × 300 μm^2 was scanned to cover the whole cisoid form single crystal with 1.5 μm lateral resolution and 32 μm axial resolution.

The obtained Raman spectra were analyzed by the band fitting as mentioned in Chapter III-5. Equation III-5 was still used as the fitting function to fit the seven low-frequency Raman bands (Figure IV-3 (b)). During fitting, each peak position and bandwidth were fixed, so the band amplitude of each band was the only adjustable parameter. Then the low-frequency Raman images were constructed from the band intensities of each vibrational mode and displayed in Figure IV-4.

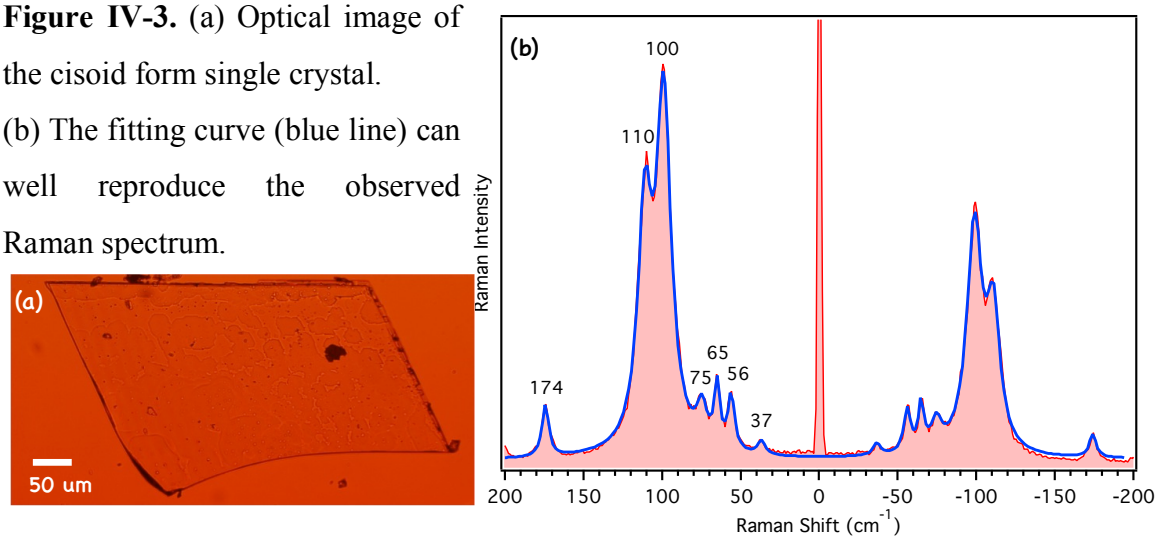

Figure IV-3. (a) Optical image of the cisoid form single crystal. (b) The fitting curve (blue line) can well reproduce the observed Raman spectrum.

As can be seen from Figure IV-4, the intensities of the Raman bands at 110, 100, 75, 56 and 37 cm^{-1} are homogeneously distributed in the cisoid form single crystal. The stronger band intensites on the lower left corner of the crystal most likely indicates that the crystal is thicker there. Apart from these bands, we found that the 174 and 65 cm^{-1} band only apears on the edge of the crystal. This finding impies that the molecular orientation on the crystal edge may differ from that of the inner part of the crystal.

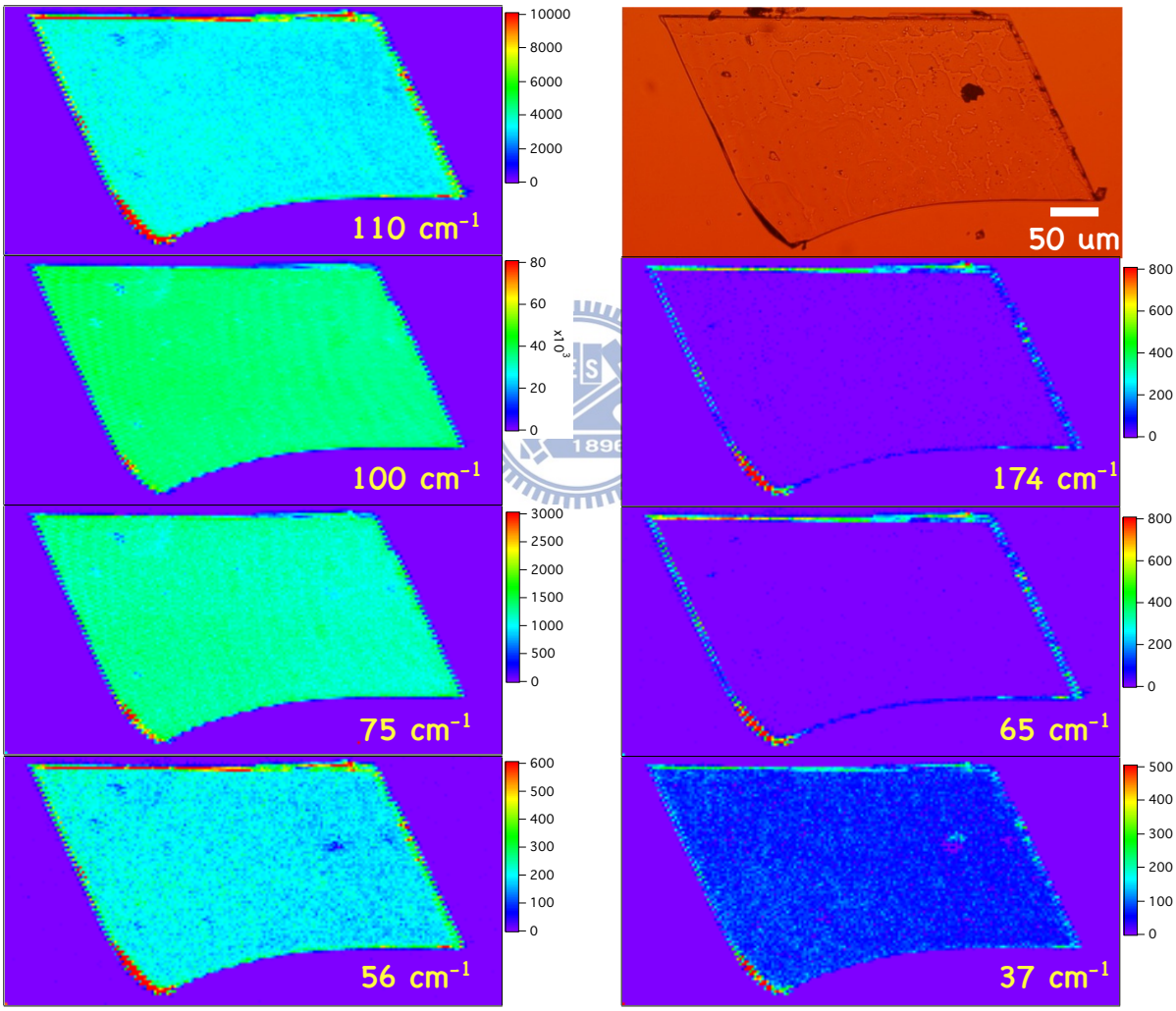

Figure IV-4. Low-frequency Raman imaging of the cisoid form single crystal and the optical image (orange picture).

IV-3-1. Structure of the Cisoid Form Crystal

According to the low-frequency Raman images shown in Figure IV-4, the 174 and 65 cm^{-1} bands appear only on the edge of the crystal. To examine the spectral difference in detail, we average the spectra around the center (inner) and the left corner (edge) of the crystal (Figure IV-5). Surprisingly, we found that the averaged Raman spectrum of the crystal edge is very similar to the spectrum of the cisoid powder sample, which is considered to consist of microcrystals with random orientations. Similarity of the edge spectrum to the powder spectrum suggests that the edge of the cisoid form single crystal is polycrystalline. This result may challenge the naive assumption that a crystal like what is shown in Figure IV-4 is spatially uniform everywhere. Although we call the measured crystal a "single cisoid form crystal", there is some heterogeneity of crystal structure that possibly results in the different low-frequency spectral patterns (Figure IV-5). The inner spectrum is considerably different from the edge spectrum. In addition to the intensities of the weak 174 and 65 cm^{-1} bands, the intensity ratio of 100/110 cm^{-1} is also different between the inner and edge regions of the cisoid crystal. Therefore, the intensity ratio of 100/110 cm^{-1} can be used to investigate the homogeneity of the cisoid molecular alignment.

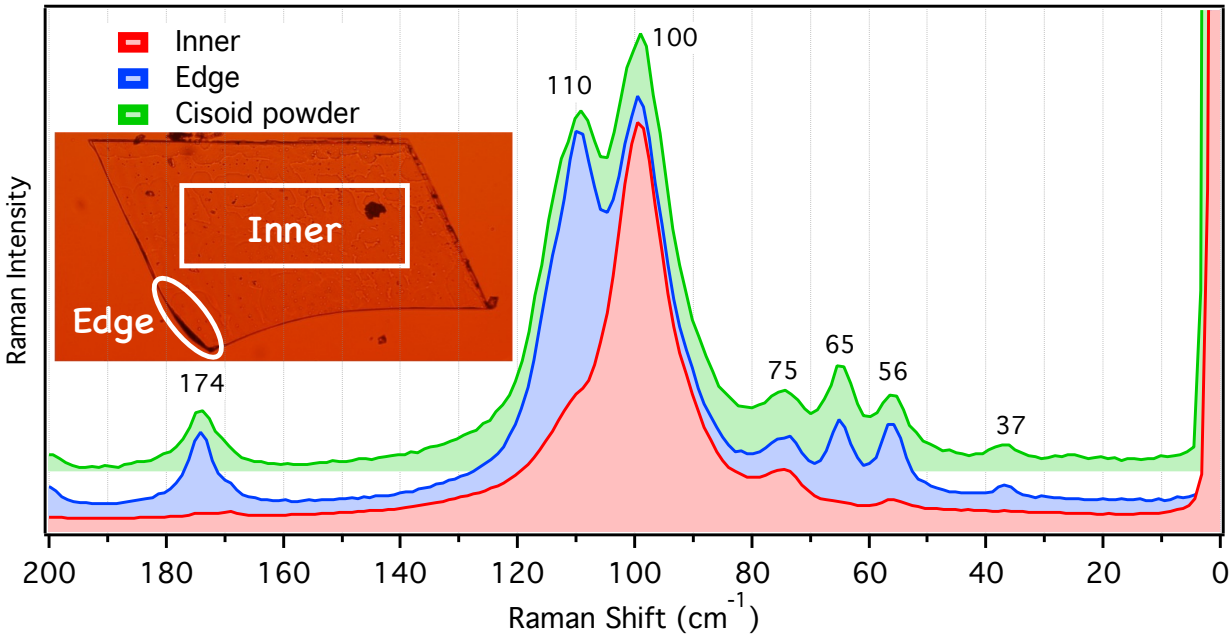

Figure IV-5. Averaged low-frequency Raman spectra of the cisoid crystal around the center (red curve) and the left corner (blue curve) compared with the cisoid powder spectrum (green curve).

Figure IV-6 shows the Raman images constructed from the intensity ratio of 100/110 cm^{-1} bands. The ratio is homogeneously distributed inside the crystal but decreases on the edge. Based on this result, a schematic illustration of crystal orientations in the cisoid form crystal (Figure IV-7) can be drawn. The width of the polycrystalline edge was estimated to about 9 μm (corresponding to ~3 pixels in the image). Finally, we conclude that the intensity ratios of the low-frequency Raman bands are useful to examine crystal orientation. Thus it is applicable to check the quality of crystal growth.

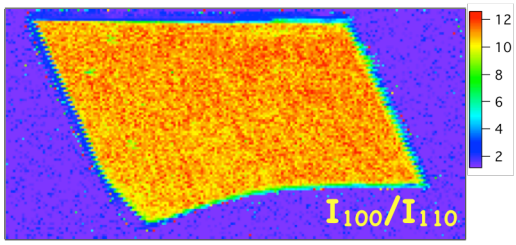

Figure IV-6. Raman imaging with the intensity ratio of the 100/110 cm^{-1} bands.

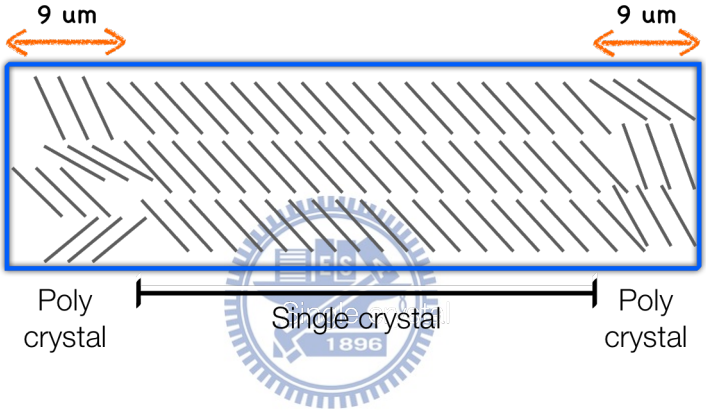

Figure IV-7. Proposed heterogeneous crystal structure of the cisoid form crystal.

IV-4. Low-Frequency Raman Imaging of the Transoid Form Crystal Adjacent to Cisoid Form Crystal

Next we investigated transoid and cisoid microcrystals that are in close proximity (Figure IV-8 (a)) by low-frequency Raman imaging. In the present study, we demonstrate the ability of low-frequency Raman bands to easily distinguish microcrystals with different crystal structures. Space-resolved Raman spectra were recorded by moving with a 1 μm step the sample mounted on the motarized stage. Each Raman spectrum was taken with 0.2 second exposure under the conditions of 532 nm excitation, 5 mW laser power and 2.7 cm^{-1} spectral resolution. Finally, an area of 160 × 160 μm^2 was scanned to cover the whole transoid crystal and part of the cisoid crystal.

Five marker bands (20 and 26 cm^{-1} for the transoid form and 100, 110, and 174 cm^{-1} for the ciosid form) are selected for band fitting. The fitting function is assumed to be a superposition of five Lorentz functions, like equation IV-1.

$$f(x) = y_0 + \sum_{i=1}^{5} \frac{A_i}{(x - x_i)^2 + B_i} \qquad (\mathrm{IV}-1)$$

where y_0 determines the baseline, A_i is the band amplitude, x_i is the peak position and B_i is square of the bandwidth. During fitting, each peak position and bandwidth were fixed and the band amplitude was the only adjustable parameter. Representative fitting results of the Raman spectra measured at three locations indicated in Figure IV-8 (a) are displayed in Figure IV-8 (b).

In addition, the intensity ratio of the pair of high-frequency Raman bands 510/532 cm^{-1} was also calculated to distinguish the cisoid and transoid forms on a molecular basis. The fitting

procedure is the same as described in Chapter III-5. Representative fitting results are shown in Figure IV-8 (c).

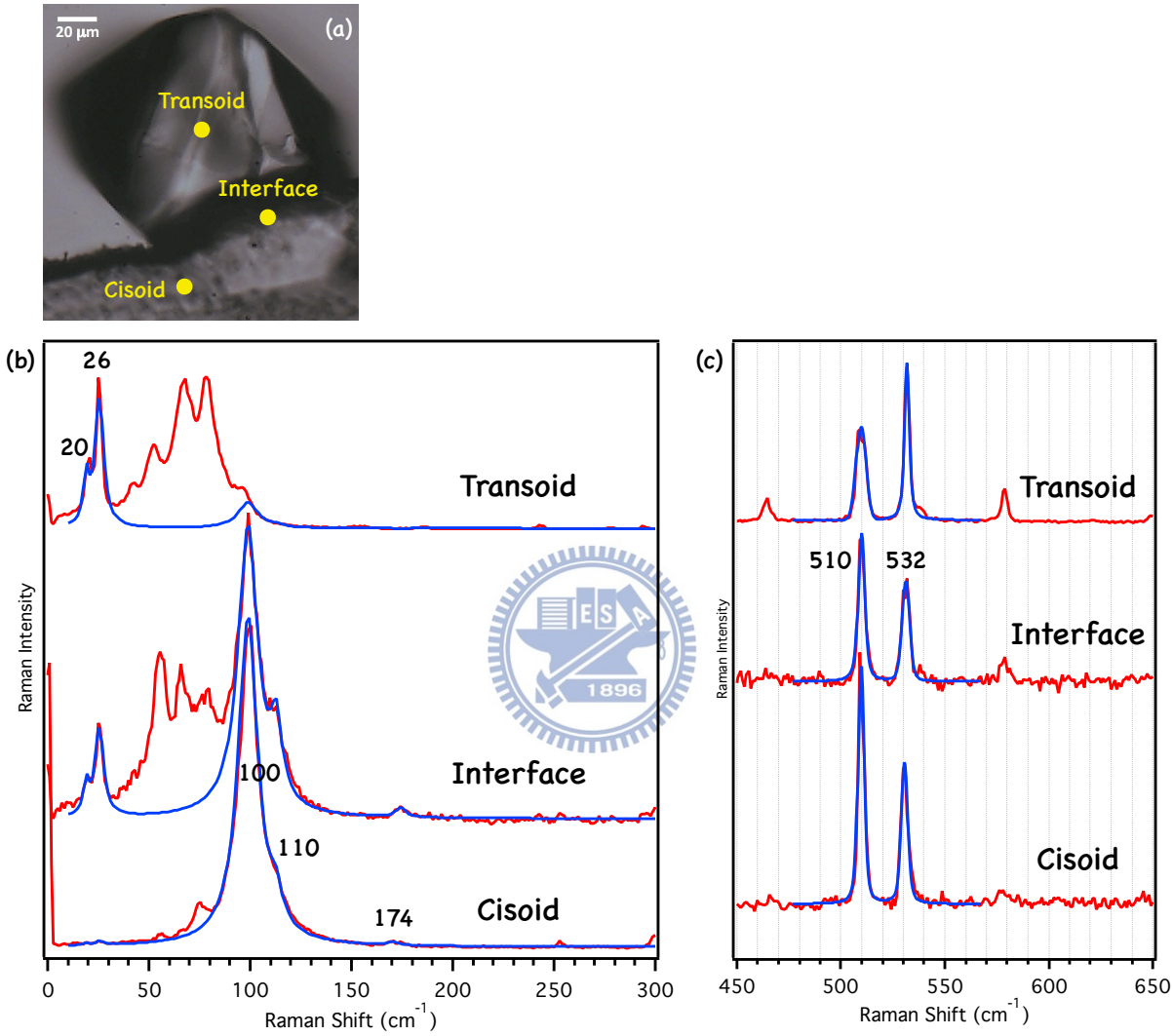

Figure IV-8. (a) Optical image of cisoid/transoid crystal mixture.
(b)(c) Representative Raman spectra selected from the points labeled in panel (a) (red curves) and the fitting curves (blue curves).

Raman images have been constructed from the band amplitudes at 20, 26, 100, 110, and 174 cm^{-1} and intensity ratios of 510/532 cm^{-1} (Figure IV-9 (b)–(g)). The images of the low-frequency bands (Figures IV-9(b)–(f)) can selectively see either the cisoid or transoid crystal depending on which crystal marker band is used, and provide the information on the heterogeneity of the crystals. Although the Raman image of the 510/532 cm^{-1} intensity ratio (Figure IV-9(g)) is capable of distinguishing between the cisoid and transoid forms, it does not contain the information on detailed crystal orientations. Moreover, due to the weaker intensity of these bands, the image is easily interfered with the noise from background. Unlike the cisoid crystal discussed in section IV-3, the Raman images of the cisoid bands at 100, 110, and 174 cm^{-1} (Figures IV-9 (d)–(f)) look quite heterogeneous presumably due to sublimation involved in the sample preparation. It should be noted that crystal morphology also affects the Raman images constructed from intensities; if the focal volume probes a large part of the crystal, the observed Raman intensity would be greater. Figure IV-10 compares the band intensity of 26 and 530 cm^{-1} along the axis of the transoid crystal. The 26 cm^{-1} low-frequency band show markedly high contrast to the background compare with the high-frequency band.

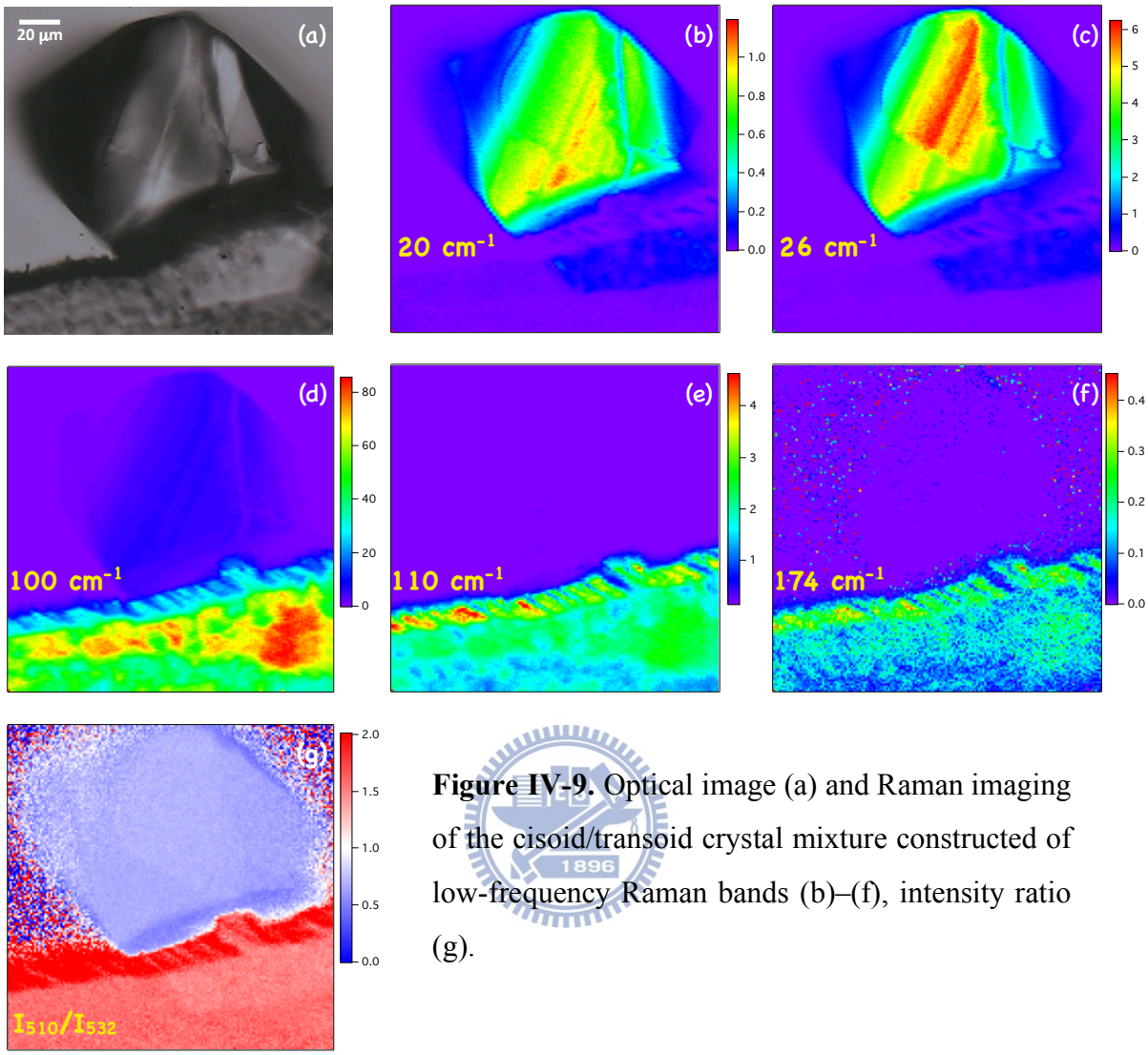

Figure IV-9. Optical image (a) and Raman imaging of the cisoid/transoid crystal mixture constructed of low-frequency Raman bands (b)–(f), intensity ratio (g).

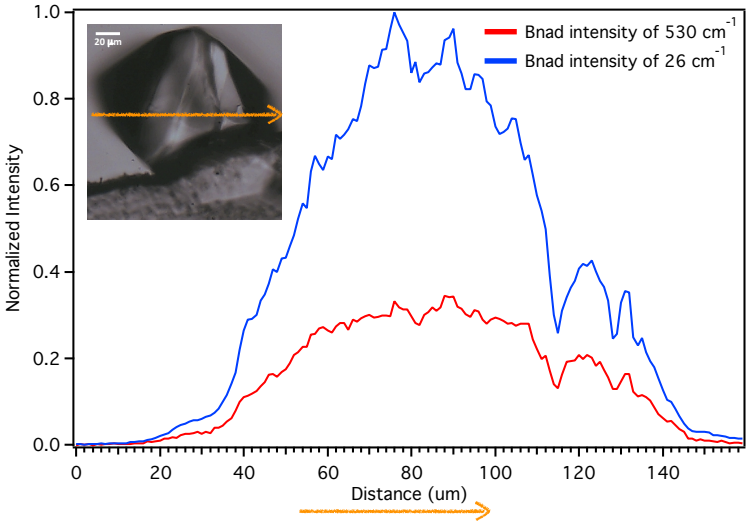

Figure IV-10. Comparison of the intensity variation of the 26 and 530 cm^{-1} bands along the direction indicated by an orange arrow.

IV-4-1. Domain Structures in the Transoid Crystal

As mentioned in Chapter III-3-1, the intensity ratio of low-frequency bands can be utilized to monitor the homogeneity of crystals. Here, we calculated the intensity ratio of 26/20 cm^{-1} and constructed the Raman image, as displayed in Figure IV-11 (a). In the Raman image, we can find many micro-domains (white and red-colored regions) with different crystal orientations. A red-colored domain indicates that the 26 cm^{-1} band is stronger than the 20 cm^{-1} band, whereas a blue-colored domain indicates that the 26 cm^{-1} band is weaker. From Figure IV-11 (b), the relative intensity difference at 26 and 20 cm^{-1} within different micro-domains is clearly seen. This kind of micro-domains with different crystal orientations is hardly possible to be solved in X-ray diffraction analysis, but is evident from low-frequency Raman imaging.

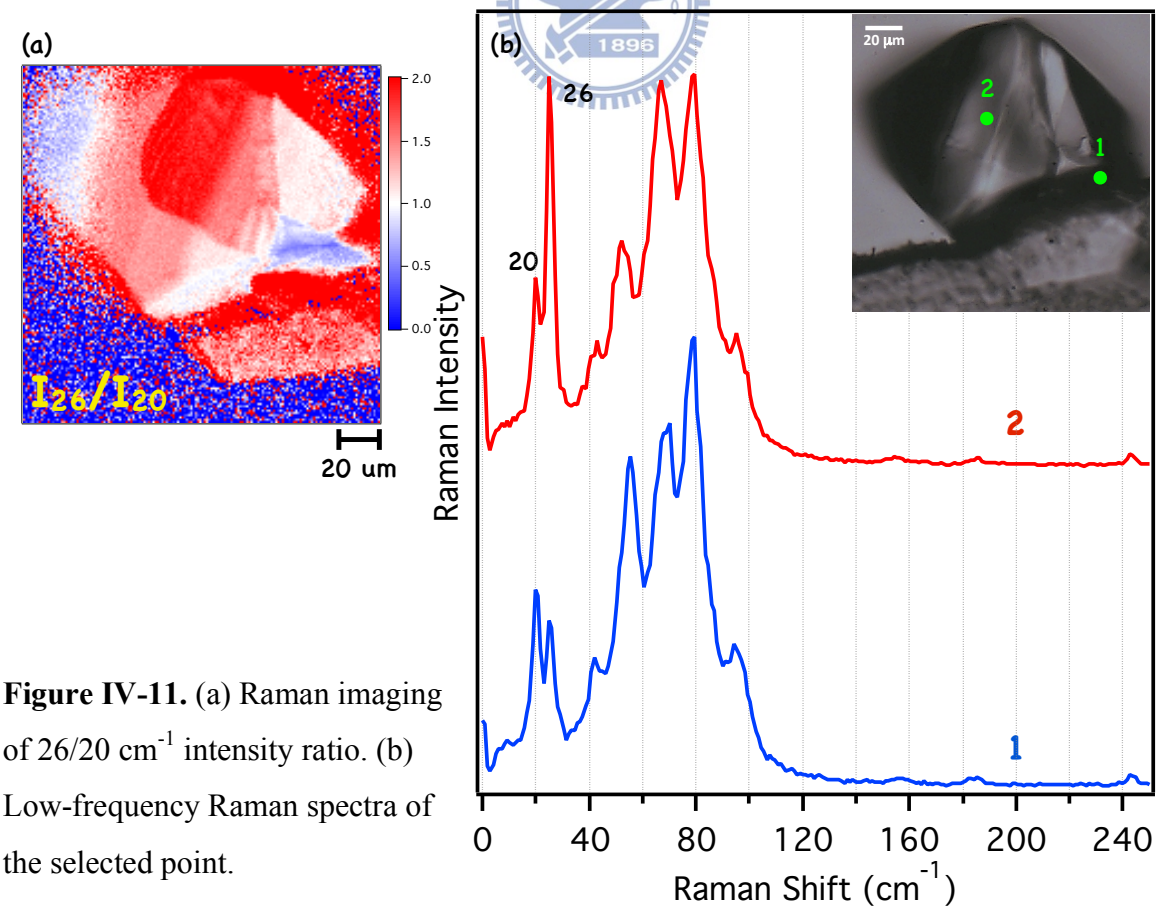

Figure IV-11. (a) Raman imaging of 26/20 cm^{-1} intensity ratio. (b) Low-frequency Raman spectra of the selected point.

IV-5. Polarized Low-Frequency Raman Imaging of the Transoid Form Crystal Adjacent to Cisoid Form Crystal

Because the low-frequency Raman spectrum (<150 cm^{-1}) of crystalline 1,1′-binaphthyl has yet to be reported, the assignment of the low-frequency Raman bands is crucial to understand the profound physical meaning of intermolecular interactions. Therefore, we have performed polarized low-frequency Raman imaging measurements with a view to understand the symmetry of molecular polarizabilities responsible for those low-frequency Raman bands. Here, the same cisoid/transoid crystal mixture as discussed in the last section was studied. Space-resolved Raman spectra were recorded by moving with a 1 μm step the sample mounted on the motarized stage. Each Raman spectrum was taken with 0.5 second exposure under the conditions of 532 nm excitation, 1 mW laser power and 2.7 cm^{-1} spectral resolution. Finally, an area of 160 × 160 μm^2 was scanned to cover the whole transoid crystal and part of the cisoid crystal. These experimental conditions were fixed throughout the measurements of four polarization configurations.

IV-5-1. Definition of Four Polarization Configurations

In this section, Raman imaging was performed with four different polarization configurations: namely, Z(XX)Z′, Z(XY)Z′, Z(YX)Z′ and Z(YY)Z′, where the four characters are defined as “direction of the incident laser, (incident laser polarization, analyzer/signal polarization), direction of the Raman signal” in the laboratory-fixed coordinates system. A

schematic layout of the X, Y, and Z axes is displayed in Figure IV-12. All Raman spectra were normalized by the white light spectra taken with X or Y analyzer polarization.

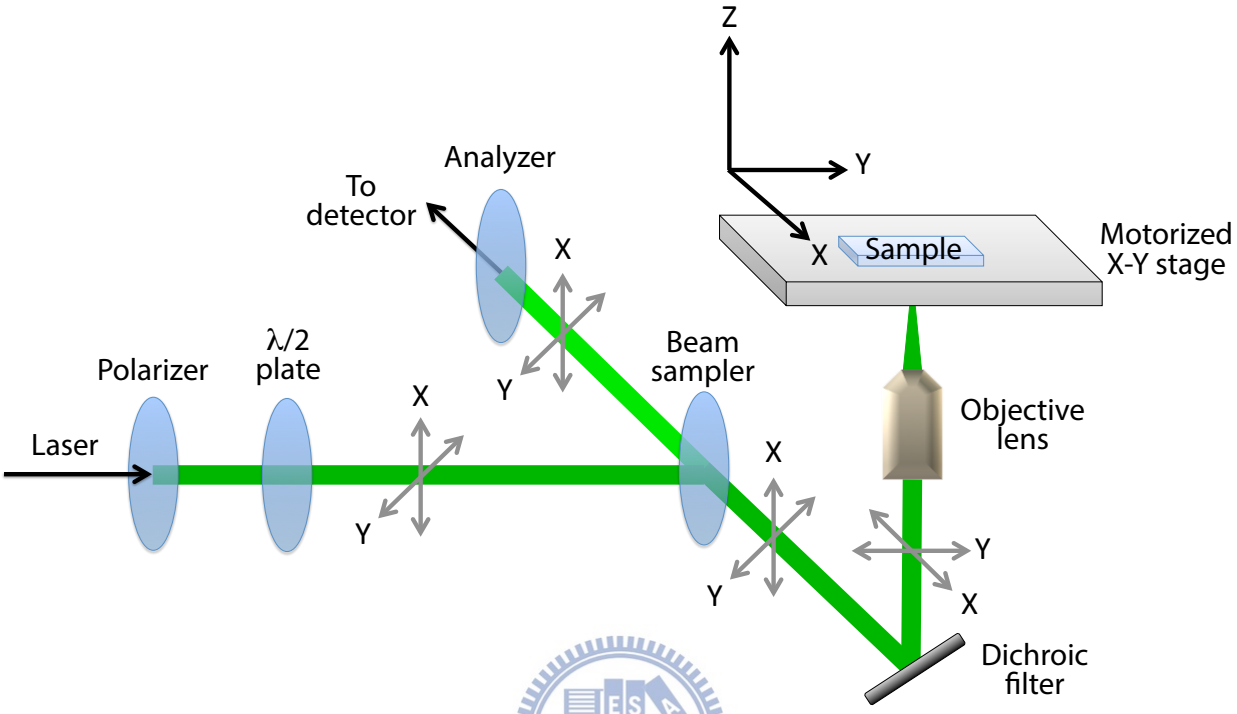

Figure IV-12. Schematic layout of the polarization configurations employed in the low-frequency confocal Raman microspectrometer.

IV-5-2. Singular Value Decomposition and Band Fitting

Due to the weak laser power (1 mW) and low transmittance of the thin-film analyzer (< 40%), the signal-to-noise ratio (S/N) of the Raman spectra was much lower compared with the former measurements. Thus, singular value decomposition (SVD) has been performed to improve the S/N, which has been successfully applied to many other studies [8-13]. SVD is a mathematical procedure that decomposes an arbitrary $m \times n$ matrix $\boldsymbol{A}$ into the product of three matrices as $\boldsymbol{A} = \boldsymbol{UWV^T}$ [14], where $\boldsymbol{U}$ is a $m \times n$ column-orthonormal matrix, $\boldsymbol{W}$ is a

$n \times n$ diagonal matrix of non-negative singular values, and $\boldsymbol{V^T}$ is a $n \times n$ orthonormal matrix. In our experiments, matrix $\boldsymbol{A}$ contains m spectra with n pixels (corresponding to wavenumbers) in each spectrum. Matrix $\boldsymbol{U}$ contains the information on spectral components. The diagonal elements of matrix $\boldsymbol{W}$, i.e., singular values, represent the contributions of the spectral components. Matrix $\boldsymbol{V^T}$ contains the spatial information in the present case. Figure IV-13 shows the singular values of the first 100 components for four different polarization configurations. The components in the shaded region have significantly large singular values, so they were retained to reproduce matrix $\boldsymbol{A}$. Representative spectra after SVD denoising are compared with the original spectra before SVD in Figure IV-14, which clearly illustrates that the S/N of the spectra has been substantially improved without distorting the spectral shape.

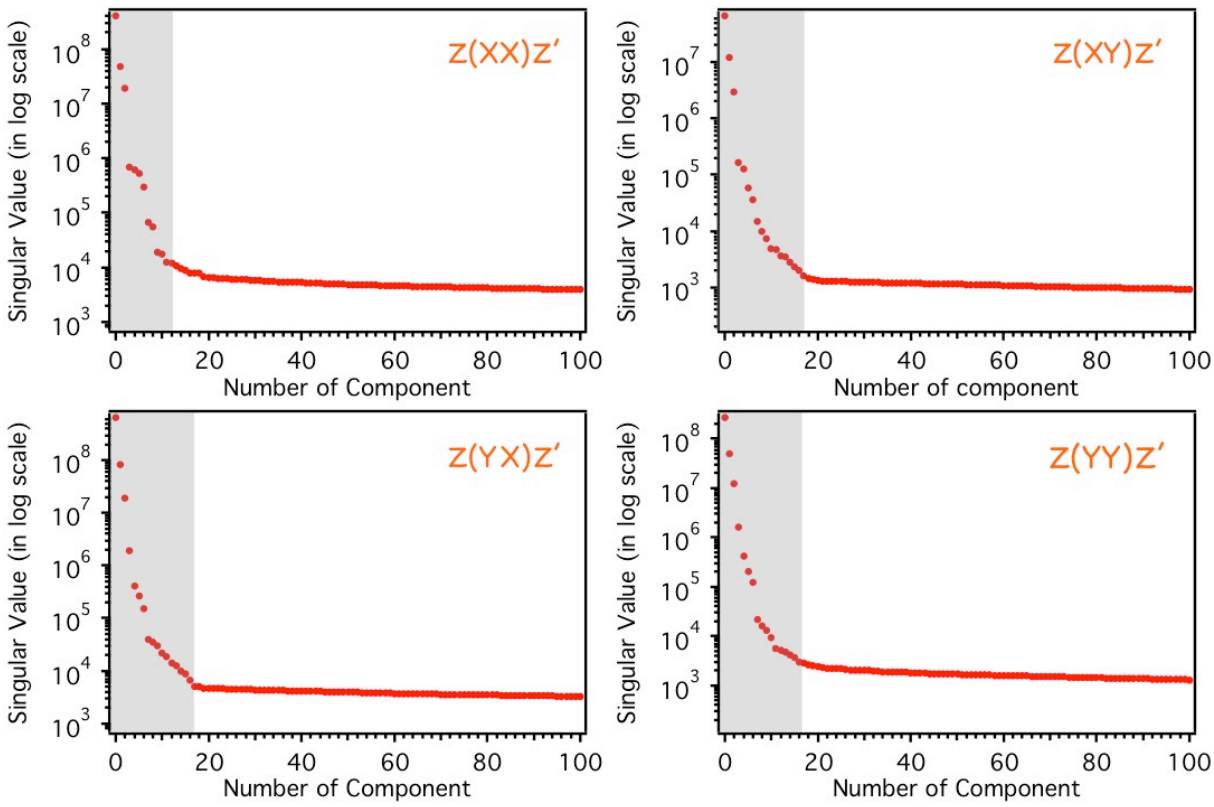

Figure IV-13. Singular value of the first 100 spectral components (red dots). The dots in the shaded region were retained to reproduce the matrix.

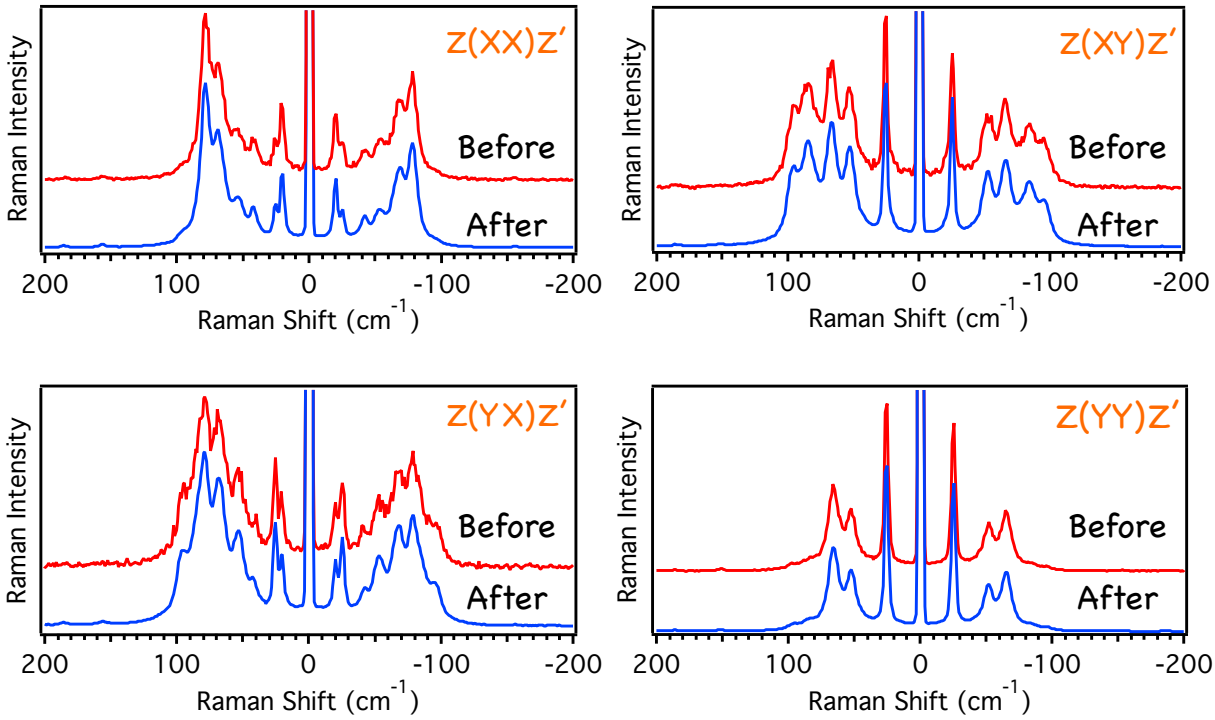

Figure IV-14. Low-frequency Raman spectra of the transoid crystal before (red curves) and after SVD (blue curves).

The SVD-denoised Raman spectra were subsequently analyzed with band fitting. The band fitting was performed on the low-frequency region (−200 to +200 cm^{-1}), following the same procedure as mentioned in Chapter III-5. Representative fitting results are shown in Figure IV-15. The 20, 26, 100, and 110 cm^{-1} bands can be fitted well by the assumed function, while the Raman bands within 40–95 cm^{-1} cannot particularly for the Raman spectra of the cisoid/transoid interface.

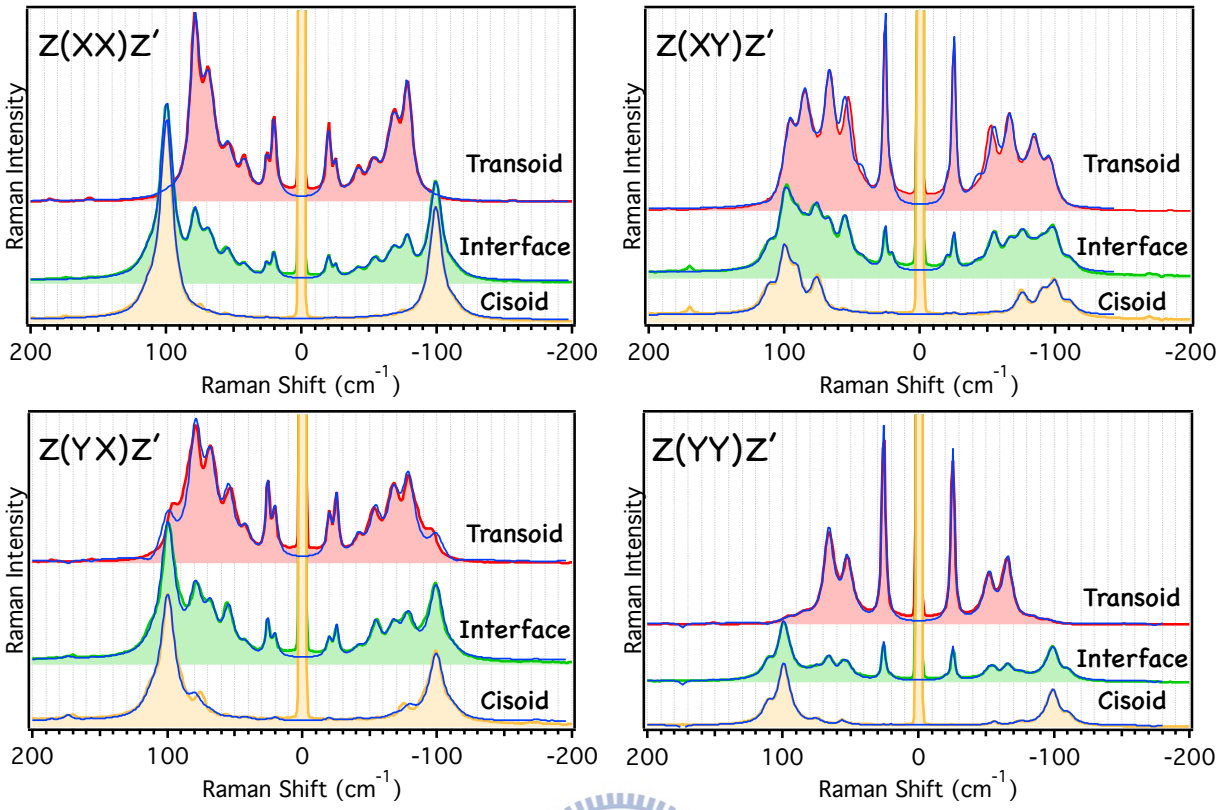

Figure IV-15. Representative fitting results (blue curves) of the cisoid (yellow curve), transoid (red curve) and cisoid/transoid interface (green curves) spectra.

IV-5-3. Polarized Raman Imaging of the Selected Low-Frequency Bands

The 20, 26, 100, and 110 cm^{-1} bands are the most important low-frequency bands that can discriminate the cisoid and transoid forms. Therefore, we focus on the polarization dependence of these four bands. Fortunately, they can be fitted well by the assumed fitting function (Equation III-5). The Raman images of the 20, 26, 100, and 110 cm^{-1} bands for the four polarization configurations were constructed from the band amplitude and are shown in Figure IV-16. The same color scale is used for each vibrational mode. We can clearly see the molecular

polarizability components that dominate the 20 and 26 cm^{-1} bands are perpendicular to other; the 20 cm^{-1} band would seem to be associated with the X direction, whereas the 26 cm^{-1} band the Y direction. In contrast, the 100 and 110 cm^{-1} bands would have a very similar polarizability component. As briefly demonstrated here, polarized Raman imaging helps us understand the symmetry of the molecular polarizability of the low-frequency modes. If we are able to define the crystal axis accurately, then this technique can be applied to obtain the absolute orientation of micro-domains in the transoid crystal.

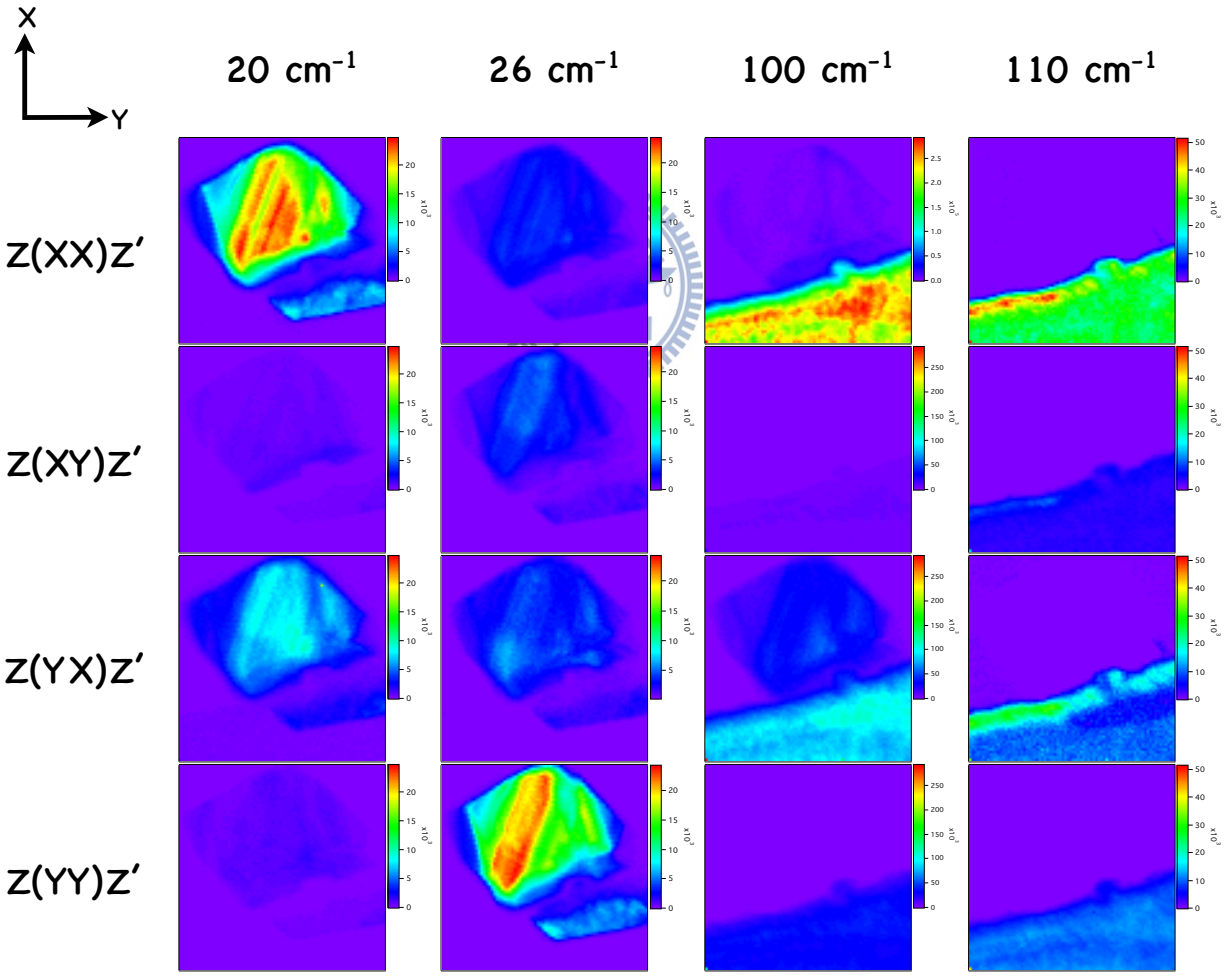

Figure IV-16. Low-frequency Raman imaging of the cisoid/transoid crystal mixture performed with four polarization configurations.

IV-6. Summary

In this chapter, we have demonstrated that low-frequency Raman imaging can effectively distinguish different crystal structures even if they have the same chemical formula. In addition, the intensity ratios of the low-frequency bands provide otherwise inaccessible information on microscopic heterogeneity (e.g., domain structure and crystal twinning) of apparent single crystals. Our study is the first to show that low-frequency Raman imaging can be a powerful addition to the crystallography toolbox.

The Raman imaging of the cisoid form crystal has shown that the inner part of the crystal is homogeneous as expected. However, we have revealed that the edges of the crystal are polycrystalline and exhibit a quite similar spectral pattern to the cisoid powder sample. The polycrystalline edge region has been estimated to be about 9 μm.

Using a composite of the cisoid and transoid microcrystals, we have demonstrated the ability of low-frequency Raman imaging to selectively visualize the cisoid and transoid crystals with markedly high contrast. Although the intensity ratio of some high-frequency bands (e.g., 510/532 cm^{-1}) can also discriminate the cisoid and transoid forms, the relatively low intensity levels increase errors in analysis and hence decrease the detection limit. Moreover, the precious information on crystal heterogeneity is lost. From the Raman imaging of the 26/20 cm^{-1} intensity ratio in the transoid crystal, we observed many micro-domains with different crystal orientations. The boundary of each micro-domain can be clearly seen by our method, but this kind of boundary is extremely hard to be solved by X-ray diffraction analysis. The polarized low-frequency Raman imaging further confirms the presence of micro-domains in the transoid

crystal.

In conclusion, we think low-frequency Raman imaging technique will be a novel tool for advanced crystallography.

References for Chapter VI.

[1]. Chuan-Keng Huang, H. Hamaguchi, and S. Shigeto, "*In vivo* multimode Raman imaging reveals concerted molecular composition and distribution changes during yeast cell cycle," *Chemical Communications*, vol. 47, 9423-9425, 2011.

[2]. Chuan-Keng Huang, M. Ando, H. Hamaguchi, and S. Shigeto, "Disentangling Dynamic Changes of Multiple Cellular Components during the Yeast Cell Cycle by *in Vivo* Multivariate Raman Imaging," *Analytical Chemistry*, vol. 84, pp. 5661-5668, 2012.

[3]. N. Noguchi, A. Abduriyim, I. Shimizu, N. Kamegata, S. Odake and H. Kagi, "Imaging of Internal Stress Around a Mineral Inclusion in a Sapphire Crystal: Application of Micro-Raman and Photoluminescence Spectroscopy," *Journal of Raman Spectroscopy*, vol. 44, pp. 147-154, 2013.

[4]. M. R. D. Bomio, L. S. Cavalcante, M. A. P. Almeida, R. L. Tranquilin, N. C. Batista, P. S. Pizani, "Structural refinement, growth mechanism, infrared/Raman spectroscopies and photoluminescence properties of PbMoO4 crystals," *Polyhedron*, vol. 50, pp. 532-545, 2013.

[5]. H. Pataki, I. Csontos, Z. K. Nagy, B. Vajna, M. Molnar, L. Katona and G. Marosi, "Implementation of Raman Signal Feedback to Perform Controlled Crystallization of Carvedilol," *Organic Process Research & Development*, vol. 17, pp. 493-499, 2013.

[6]. R. B. Kress, E. N. Duesler, M. C. Etter, I. C. Paul, and D. Y. Curtin, "Solid-state Resolution of Binaphthyl: Crystal and Molecular Structures of the Chiral $(A)^1$ Form and Racemic $(B)^1$ Form and the Study of the Rearrangement of Single Crystals. Requirements for Development of Hemihedral Faces for Enantiomer Identification," *Journal of the American Chemical Society,* vol. 102, pp. 7709-7714, 1980.

[7]. D. K. Kondepudi, J. Laudadio, and K. Asakura, "Chiral Symmetry Breaking in Stirred Crystallization of 1,1'-Binaphthyl Melt," *Journal of the American Chemical Society,* vol. 121, pp. 1448-1451, 1999.

[8]. M. Okuno, H. Kano, P. Leproux, V. Couderc, J. P. R. Day, M. Bonn, and H. Hamaguchi, "Quantitative CARS molecular fingerprinting of single living cells with the use of the maximum entropy method", *Angewandte Chemie International Edition*, vol. 49, pp. 6773-6777, 2010.

[9]. H. J. van Manen, N. Uzunbajakava, R. van Bruggen, D. Roos, and C. Otto, "Resonance Raman imaging of the NADPH oxidase subunit cytochrome b(558) in single neutrophilic granulocytes", *Journal of the American Chemical Society*, vol. 125, pp. 12112-12113, 2003.

[10]. H. J. van Manen, Y. M. Kraan, D. Roos, and C. Otto, "Intracellular chemical imaging of heme-containing enzymes involved in innate immunity using resonance Raman microscopy", *Journal of Physical Chemistry B*, vol. 108, pp. 18762-18771, 2004.

[11]. M. Ando, M. Sugiura, H. Hayashi, and H. Hamaguchi, "1064 nm deep near-infrared (NIR) excited Raman microspectroscopy for studying photolabile organisms", Applied Spectroscopy, vol. 65, pp. 488-492, 2011.

[12]. M. Okuno, and H. Hamaguchi, "Multifocus confocal Raman microspectroscopy for fast multimode vibrational imaging of living cells", *Optics Letters*, vol. 35, pp. 4096-4098, 2010.

[13]. H. N. N. Venkata, N. Nomurab, and S. Shigeto, "Leucine pools in *Escherichia coli* biofilm discovered by Raman imaging", *Journal of Raman Spectroscopy*, vol. 42, pp. 1913-1915, 2011.

[14]. G. H. Golub and C. Reinsch, "Singular Value Decomposition and Least Squares Solutions", *Numerische Mathematik*, vol. 14, pp. 403-420, 1970.

Chapter V.

Future Perspectives

Although the transformation from the ciosid to transoid form is commonly known via sublimaiton followed by recrystallization, we still do not understand how molecules manner in microscopic view. For example, the sublimation starts from a single molecule or cluster of molecules? And how does the transoid crystal grow? To solve these questions, syncronously heat up the cisoid form crystal under a microscope and acquire Raman images in a short time are required. An electron multiplying charge coupled device (EMCCD) can reach the detection time as short as 10 μs per spectrum, and if we scan an area of 100 × 100 μm^2 by 1 μm step, then each Raman image can be acquired within 5 minutes. Keep tracing the transformation by taking Raman images each 5 minutes help us understand how the cisoid form disappears and how the transoid crystal grows. In addition, three-dimensional Raman mapping with a piezo stage of the cisoid and transoid form crystals are essential to fully understand the distribution of domain structures and their orientations.